UC Santa Barbara
UC Santa Barbara Electronic Theses and Dissertations

Title
First Principles Modeling of the Thermodynamic and Kinetic Properties of Superalloys

Permalink
https://escholarship.org/uc/item/55d5w0cv

Author
Goiri, John

Publication Date
2018

Peer reviewed|Thesis/dissertation

eScholarship.org Powered by the California Digital Library
University of California

University of California
Santa Barbara

First Principles Modeling of the Thermodynamic and Kinetic Properties of Superalloys

A dissertation submitted in partial satisfaction
of the requirements for the degree

Doctor of Philosophy
in
Materials

by

Jon Gabriel Goiri

Committee in charge:

Professor Anton Van der Ven, Chair
Professor Tresa Pollock
Professor Carlos G. Levi
Professor M. Scott Shell

December 2018

The Dissertation of Jon Gabriel Goiri is approved.

Professor Tresa Pollock

Professor Carlos G. Levi

Professor M. Scott Shell

Professor Anton Van der Ven, Committee Chair

November 2018

First Principles Modeling of the Thermodynamic and Kinetic Properties of Superalloys

Copyright © 2018

by

Jon Gabriel Goiri

Curriculum Vitæ

Jon Gabriel Goiri

Education

2012-2018	Ph.D. in Materials (Expected), University of California, Santa Barbara.
2007-2011	B.S in Chemical Engineering, University of Michigan

Publications

2016	J. G. Goiri and A. Van der Ven, *Phase and structural stability in Ni-Al systems from first principles*, *Physical Review B* **94** (Sept., 2016)
2018	J. G. Goiri and A. Van der Ven, *Recursive alloy Hamiltonian construction and its application to the Ni-Al-Cr system*, *Acta Materialia* **159** (Oct., 2018) 257–265
2018	L. Feng, D. Lv, R. K. Rhein, J. G. Goiri, M. S. Titus, A. Van der Ven, T. M. Pollock, and Y. Wang, *Shearing of γ' particles in Co-base and Co-Ni-base superalloys*, *Acta Materialia* **161** (Dec., 2018) 99–109

Abstract

First Principles Modeling of the Thermodynamic and Kinetic Properties of Superalloys

by

Jon Gabriel Goiri

Ni-Al based alloys remain a material of technological importance for high strength and high temperature applications. A design that optimizes desirable properties, such as strength, or creep and oxidation resistance, requires a deep understanding of thermodynamics and kinetics. This thesis uses *ab initio* methods to model both phase stability and diffusion processes. Starting from Density Functional Theory (DFT), formation energies of different crystal orderings are used to parameterize cluster expansion models. Used in conjunction with Monte Carlo techniques, these models can be used to derive macro scale properties at finite temperature.

We use DFT calculations to explore orderings on FCC and BCC, first for the Ni-Al binary, and then the Ni-Al-Cr ternary. Our calculations not only predict the stability of known phases, but also reveal new families of previously unknown ordered phases. We introduce strain order parameters to systematically analyze orderings on both FCC and BCC lattices. Many of these orderings are predicted to be unstable around $x_{Ni} = 0.625$, where a martensitic phase transformation is known to occur.

DFT calculations serve as training data for cluster expansion effective Hamiltonians, which accurately predict formation energies of arbitrary orderings without costly computations. We use these effective Hamiltonians in Monte Carlo simulations to calculate free energies, with which we construct phase diagrams. The difficulty of parameterizing a cluster expansion grows exponentially with the number of possible components. We introduce a recursive approach to parameterize multi-component alloy Hamiltonians us-

ing interaction parameters from simpler subsystems as Bayesian informative priors. We applied this approach to expand the statistical mechanics study of Ni-Al to Ni-Al-Cr, and explore Cr behavior within the $L1_2$ ordering.

The same cluster expansion methods can be used to model hop barriers of kinetic processes as a function of the ordering on the crystal. Diffusion barriers for Al hops have a strong dependence on the immediate local composition, while Ni hops are largely independent of their local ordering. We have developed a rigorous Kinetic Monte Carlo model that incorporates these relationships of hop barriers with local ordering, and applied it to the Ni-Al binary. Ni and Al exhibit different diffusion properties in the γ and γ' phases, which we discuss using various metrics of diffusion.

Contents

Curriculum Vitae **iv**

Abstract **v**

1 Introduction **1**

2 Computational Methods **6**

2.1 Density functional theory 7
2.2 Cluster expansion formalism 11
2.3 Monte Carlo methods and statistical mechanics 21

3 **28**

3.1 Introduction 28
3.2 Methods 30
3.3 Results 38
3.4 Discussion 56
3.5 Conclusion 63
3.6 Acknowledgements 63

4 **65**

4.1 Introduction 65
4.2 Methods 67
4.3 Results 75
4.4 Discussion 85
4.5 Conclusion 89
4.6 Acknowledgements 89
4.7 Supplementary data 90

5 Diffusive hops and their local environments **95**

5.1 Introduction 95
5.2 Methods 96
5.3 Results 105

5.4 Discussion . . . 110
5.5 Conclusion . . . 114

6 Kinetic properties of Ni-Al 116
6.1 Introduction . . . 116
6.2 Theoretical formalism . . . 117
6.3 Computational details . . . 128
6.4 Results . . . 129
6.5 Discussion . . . 141
6.6 Conclusion . . . 142

7 Summary 143

Bibliography 145

Chapter 1

Introduction

Nickel alloys are used in a wide variety of industrial applications, such as heat exchangers, chemical reactors, nuclear plants and aircraft jet engines. Their high temperature creep resistance, oxidation resistance and mechanical strength make them an attractive choice for these applications[4, 5, 6, 7], where the operating conditions involve high stresses and elevated temperatures. The design of these alloys for turbine blades places emphasis on withstanding ever increasing operating temperatures, which confers a greater efficiency for the engine[8].

A typical turbine blade is composed of a Ni-Al based substrate and a ceramic thermal barrier coating (TBC). The TBC enables the substrate to maintain its mechanical properties by protecting it from the heat generated during combustion[9]. These two layers are held together by a bond coat, which can also be Ni-Al based[10], as shown in fig. 1.1. This bond coat acts as an aluminum reservoir, and promotes the formation of a desireable alumina scale, which hinders further diffusion of oxygen into the bulk, therefore increasing its oxidation resistance[11, 6, 12, 13].

At higher temperatures, the binary Ni-Al system can form three different phases[14], which can be seen in figs. 1.2a to 1.2c.

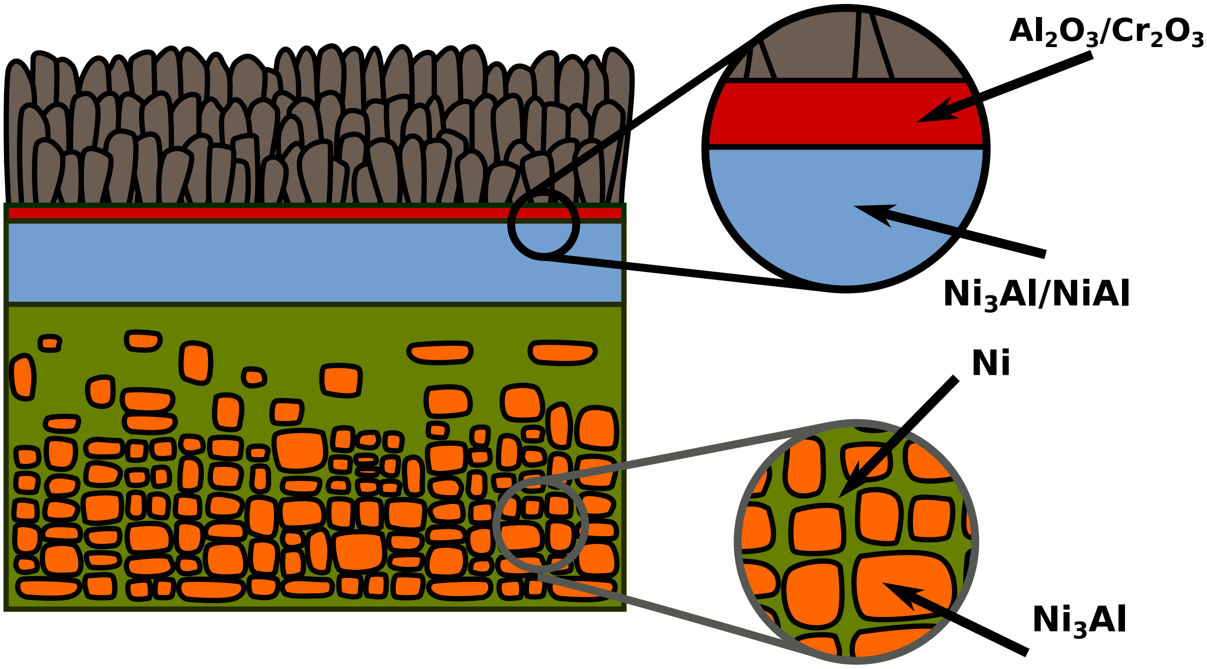

Figure 1.1: Schematic of a turbine blade cross section. The substrate, composed of γ' precipitates in a γ matrix, gives the turbine blade its mechanical strength. The thermal barrier coating acts as an insulator from external heat, while the bond coat promotes the formation of a thin oxide scale, which protects the blade from oxidation.

- γ phase, a FCC Ni solid solution with low amounts of Al (fig. 1.2a)
- $\gamma\prime$ phase, which forms around an Al fraction of 0.25. This is a FCC phase with $L1_2$ ordering (fig. 1.2b)
- β phase, which forms around an Al fraction of 0.5. This is a BCC phase with B2 ordering, and is known to accommodate a large number of vacancies at higher Al compositions[15]. (fig. 1.2c)

1.0.1 Design considerations

The high stresses experienced by the blades require the substrate to maintain it's mechanical properties. In order to accomplish this, the blades are cast as single crystals

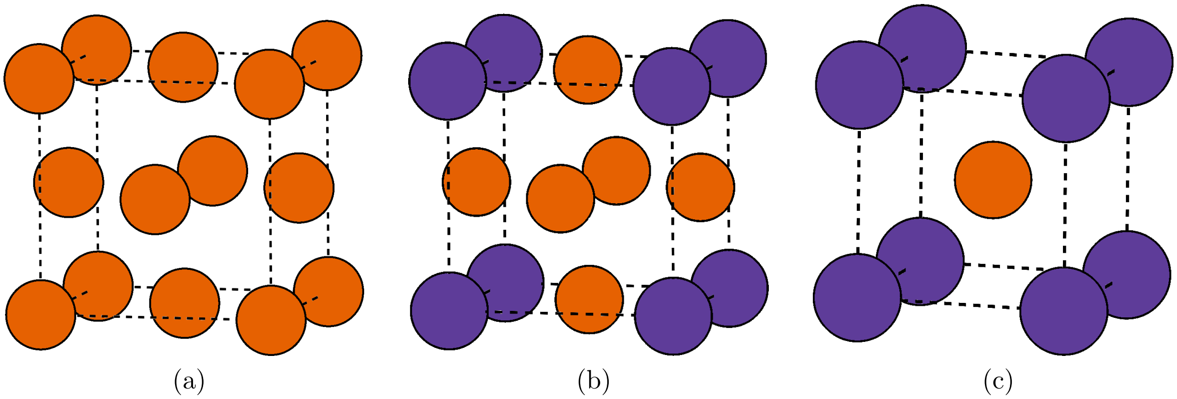
(a) (b) (c)

Figure 1.2: Unit cells for the three high temperature Ni rich orderings: the γ phase (FCC Ni solid solution, left), the γ' phase ($L1_2$ ordering, center), and the β phase (B2 ordering, right).

at a composition that promotes a two phase γ and $\gamma\prime$ mixture. The $\gamma\prime$ precipitates into the γ solid solution in cuboid shapes. The presence of these precipitates plays a crucial role in the mechanical properties of the alloy, as they inhibit the motion of dislocations.[16, 17] The composition of the alloy is carefully designed in order to create an optimal density of these precipitates. Additions of other elements (e.g. Ti, Ta, Mo, Hf, etc) influence the lattice parameters of the resulting phases[18]. This is an additional consideration in the design of the alloy, since the mismatch in lattice parameters of the two phases influences the shape of the precipitates. Additionally, the minor additions of different elements to the alloy also influences the travel of dislocations by solid solution hardening. The chemistry of these additions must be considered carefully, since an excess of these strengthening elements promotes the precipitation of undesired topologically closed packed phases[19].

During operation, the blades are exposed to heat in air. The exposure to oxygen introduces another design problem, namely the oxide films that can form on the surface of the blades, below the TBC[20]. The current solution is to allow the growth of a stable alumina (Al_2O_3) film between the TGO and bond coat, which has been show to effectively protect the blade from degradation. Even though this alumina phase is the most thermodynamically stable, other oxide phases can grow instead. NiO and $NiAl_2O_4$, which are observed to form more quickly than the alumina oxide, form non-protective coatings and are therefore undesirable[21]. The alumina phase is promoted by selecting an appropriate composition at the surface. Because the Al concentration at the surface is depleted as the alumina forms, the further growth of this oxide can be promoted by ensuring further Al is available to continue the reaction. A bond coat with a high Al content (such as the β phase) can therefore be used as an Al reservoir, such that Al is depleted from the bond coat to form alumina, rather than from the substrate[22]. Additions of different elements such as Pt can lower the activity of Ni, which suppresses the formation of undesired oxides, while Cr can foment the growth of alumina or chromia scales. The fast forming oxides are seen to appear first, but at higher Cr compositions, the flux towards the surface is great enough to completely form an alumina/chromia layer. After the fast forming oxides spall away, only alumina is left at the surface as a continuous scale[11]. The oxide formation is determined by how different elements can diffuse towards the surface as well as the thermodynamic stabilities of the oxides at different compositions.

1.0.2 Predictive limitations

The many component chemistries used in the new designs of alloys are largely a product of trial and error. Complex interactions between various elements make it difficult to know exactly how variations in the alloy chemistry will ultimately affect its properties. Understanding how compositions will affect phase fractions, phase compositions, lattice parameters and oxide stabilities requires a thorough thermodynamic basis, which currently does not exist for high component systems. Furthermore, diffusion in high component alloys, which affects creep and oxide formation, is difficult to quantify experimentally. Through first principles calculations, it is possible to predict the effects of different alloying elements on these properties without the need of expensive experiments. These types of calculations have so far been limited to 2-3 component systems[23], which is a very small composition space when we consider the number of components found in an industrial blade. Combining cluster expansion methods with Monte Carlo simulations, it is possible to calculate thermodynamic free energies and diffusion coefficients using DFT calculations an input[24]. Applying these methods to various Ni-Al-X systems, it is in principle possible to generate a database of thermodynamic and kinetic properties for a myriad of alloying elements X. Unfortunately, the currently available scientific tools to perform these calculations cannot be efficiently applied to systems of complex compositions. Simple binary systems, such as Ni-Al can readily be explored using the software package CASM, but extending the functionality to include several more alloying elements will require the development of new software libraries, capable of efficiently combining multiple binary systems into a single many component system. This thesis will explore the thermodynamic and kinetic nature of the Ni rich phases in the Ni-Al binary, as well as introduce new methods to incorporate more complex chemistries into first principles models.

Chapter 2

Computational Methods

A computational approach to understanding any crystal system requires ways to model both its thermodynamic and kinetic properties. Beginning from first principles allows us to incorporate interactions at the atomistic level into our model, which are ultimately governed by quantum mechanics. The task then, is to capture the natural atomistic behavior of the system, and incorporate it into simulations that will predict macro scale behavior. Of particular use are thermodynamic free energies, which determine the relative stability of different phases at equilibrium, and kinetic coefficients, which describe the movement of different species within a crystal.

The first step to building such a model requires an understanding of the quantum behavior of the system. Though straightforward for the most basic systems (such as a single hydrogen atom), properties of multi-body systems soon become impossible to calculate without making some approximations. A useful tool to make this calculations is Density Functional Theory (DFT), which can approximate the formation energy of atomic configurations within periodic boundary conditions at 0K. A major drawback of DFT is that the calculations are computationally expensive, especially as the number of atoms in the periodic unit cell increases. We capture the atomistic behavior predicted by DFT with the cluster expansion method. Under the cluster expansion formalism, the energy of any atomic arrangement on a particular crystal structure is a sum of interactions between clusters of atoms. Once a cluster expansion that accurately predicts the formation energies given by DFT, evaluating the energy of arbitrary configurations can be done much more rapidly.

All predictions up to this point remain limited to 0K. The final step to predicting thermodynamic and kinetic behavior is to incorporate temperature into the model. This can be done through a combination of statistical mechanics and Monte Carlo techniques. The cluster expansion effectively predicts the formation energy of a particular atomic configuration or microstate, from which macroscopic quantities can be derived by sampling a Boltzmann probability distribution.

2.1 Density functional theory

The energy of a quantum system is given by the Shrödinger equation:

$$H\psi = E\psi \tag{2.1}$$

Here H is a Hamiltonian that is related to the energy of the system E through the many-body wave function ψ. The Hamiltonian describes the interactions between all bodies of the system (atomic nuclei and electrons). If the positions of the ions are $\mathbf{R}_i$ and the positions of the electrons are $\mathbf{r}_i$, then $H = H\left(\mathbf{R}_1, \mathbf{R}_2, \cdots, \mathbf{R}_N, \mathbf{r}_1, \mathbf{r}_2, \cdots, \mathbf{r}_M\right)$ for a system with N nucelii and M electrons.

Equation (2.1) is an eigenvalue equation whose solution is given by the eigenstates ψ and eigenvalues E, and it is these eigenvalues E that we are ultimately interested in calculating.

Diagonalization of eq. (2.1) can in principle yield these solutions. However, obtaining these solutions is computationally unfeasible with current classical computers. Instead a more manageable approximation of the Hamiltonian is used:

$$H = T\left(\mathbf{r}_i\right) + V_{ee}\left(\mathbf{r}_i, \mathbf{r}_j\right) + V_{ii}\left(\mathbf{r}_i, \mathbf{r}_j\right) + V_{ei}\left(\mathbf{r}_i, \mathbf{R}_j\right) \tag{2.2}$$

The first term describes the kinetic energy of the electrons:

$$T = \sum_{i}^{M} \left(\frac{\hbar}{2m_i} \nabla_i^2 \right) \tag{2.3}$$

The second term represents the Coulombic interactions between each of the electrons:

$$V\left(\mathbf{r}_i, \mathbf{r}_j\right) = \sum_{i} \sum_{j<i} \frac{1}{\left|\mathbf{r}_i - \mathbf{r}_j\right|} \tag{2.4}$$

Conversely, the third term is the Coulombic interactions between the nuclei:

$$V\left(\mathbf{R}_i, \mathbf{R}_j\right) = \sum_{i} \sum_{j<i} \frac{Z_i Z_j}{\left|\mathbf{R}_i - \mathbf{R}_j\right|} \tag{2.5}$$

Lastly, the final term expresses the interactions between electrons and nuclei:

$$V\left(\mathbf{r}_i, \mathbf{R}_j\right) = -\sum_{i} \sum_{j} \frac{Z_j}{\left|\mathbf{r}_i - \mathbf{R}_j\right|} \tag{2.6}$$

In the terms above, m represents the mass of the negatively charged electrons, and Z is the charge of a particular nucleus. The presented approximation, known as the Born-Oppenheimer approximation, assumes that the nuclei are fixed in space, and only the electrons are moving within the system. For this reason, there is no counter part to the first term T, which would introduce a kinetic component for the nuclei in the system.

The approximation of eq. (2.2) brings us closer to a solvable problem, but still remains unreasonably difficult. One approach to tackling this multi-body problem is to approximate the many-body wave funcion ψ as a product of independent single-body electron wave functions, such that

$$\psi\left(\mathbf{r}_1, \mathbf{r}_2, \cdots, \mathbf{r}_M\right) = \prod_{i}^{M} \psi\left(\mathbf{r}_i\right) \tag{2.7}$$

This simplification, known as the Hartree product, assumes that the electrons do not interact with each other. In real systems, such interactions can have significant effects on the system energy, which has led to modifications of this method, such as subjecting each electron to a mean field created by the rest of the rest of the bodies in the system.

A key to solving for the many-body equation is to realize that instead of solving a problem of degree $3M$ (three spatial coordinates for each electron), the complexity can be reduced to a problem of degree 3. This realization was made by Hohenberg, Kohn, and Sham, who showed that the groundstate energy of the system is a functional of the electron density. There is a unique electron density that maps directly onto the groundstate wave function, thus if the electron density can be solved, the energy of the system is uniquely determined. By variationally minimizing the electron density functional, the resulting energy of the corresponding energy can be calculated. Recasting the many-body wave function to an electron density we get:

$$E\left[\rho\right] = T_s + \int V_{ext}\left(\mathbf{r}\right)\rho\left(\mathbf{r}\right)d\mathbf{r} + E_H\left[\rho\right] + E_{xc}\left[\rho\right] \tag{2.8}$$

In this equation, T_s is the kinetic energy of the electrons. $\int V_{ext}\left(\mathbf{r}\right)\rho\left(\mathbf{r}\right)d\mathbf{r}$ integrates over the interactions of the electrons over an external potential field generated by the nuclei of the system. E_H is the Hartree energy, which comes from the Coulombic interactions of the electron density. E_{xc} is the exchange-correlation energy, which captures additional non-classical interactions and must be approximated.

A method devised by Kohn and Sham allows the solving of the electron density to be simplified to solving a collection of equations, each for a single electron:

$$\left[-\frac{\hbar^2}{2m}\nabla^2 + V\left(\mathbf{r}\right) + V_H\left(\mathbf{r}\right) + V_{xc}\left(\mathbf{r}\right)\right]\psi_i\left(\mathbf{r}\right) = E_i\psi_i\left(\mathbf{r}\right) \tag{2.9}$$

The single-body electron wave function ψ depends only on the three spatial variables of $\mathbf{r}$. Notice that eq. (2.9) parallels eq. (2.2), with a term for the interactions of an electron with the positive nuclei (V), and another for the repulsion of the electron with the rest of the electron density (V_H). There is also a term for the exchange-correlation introduced in eq. (2.8), related by a derivative:

$$V_{xc} = \frac{\delta E_{xc}\left[\rho\right]}{\rho\left(\mathbf{r}\right)} \tag{2.10}$$

If the system has M electrons, then M total Kohn-Sham equations are derived, which are all dependent on each other. The solution to these equation must be solved iteratively to arrive at the groundstate electron density.

A computationally efficient method to numerically solving for the electron density is the pseudopotential method. With this approach, core electrons of atoms in the system are frozen and are effectively neglected. Instead, it is assumed that the important physics of the system is contributed by the valence electrons. Doing greatly reduces the number of Kohn-Sham equations that must be solved.

Various DFT software packages exist that can solve for the multi-body electron density and formation energy of a system. The work for this thesis has used the Vienna Ab Initio Simulation Package (VASP).

2.2 Cluster expansion formalism

DFT can be used to calculate the formation energy of a particular arrangement of atoms, but is computationally demanding. Section 2.3 will show that determination of macroscopic thermodynamic and kinetic properties requires determining an amount of formation energy that is unreasonable for DFT. The evaluation of orderings on a crystal structure can be drastically sped up with a cluster expansion model. In this technique, an effective Hamiltonian is constructed that depends on the degrees of freedom associated with each atom on a crystal lattice. There are several possible degrees of freedom that could be constructed into the cluster expansion model, including vibrational or electronic degrees of freedom. The cluster expansions used in this work will deal only with occupational degrees of freedom, such that the energy of a particular crystal structure depends solely on how different species are distributed on the crystal sites. Provided atomic relaxations are not extreme, there is always a well defined position on the lattice for each atom of a crystalline solid. We therefore define the allowed degrees of freedom from out cluster expansion relative to these ideal positions.

The first step to constructing the effective Hamiltonian is to assign occupational variables to each crystal site that defines its occupant. As an introduction to the cluster expansion method, this section will outline only how to deal with a binary system, chapter 4 will later derive a more general approach for multicomponent systems. We assign a variable p_i to each crystal site i that can take a value of either 0 or 1, depending on the occupant residing on that site (e.g. Ni vs Al). The entire atomic configuration of the crystal is therefore determined by the collection of all the occupation variables $\vec{p} = \{p_1, p_2, \cdots, p_N\}$.

Next we define clusters of sites, such are points, pairs, triplets, etc. A cluster is simply a particular collection of sites on the crystal, and we can define a cluster function by taking the product of the occupation variables from the sites that make up the cluster. Examples of clusters are shown in fig. 2.1, and their basis functions can by written as

$$\phi_\alpha(\vec{p}) = \prod_{i\in\alpha} p_i \tag{2.11}$$

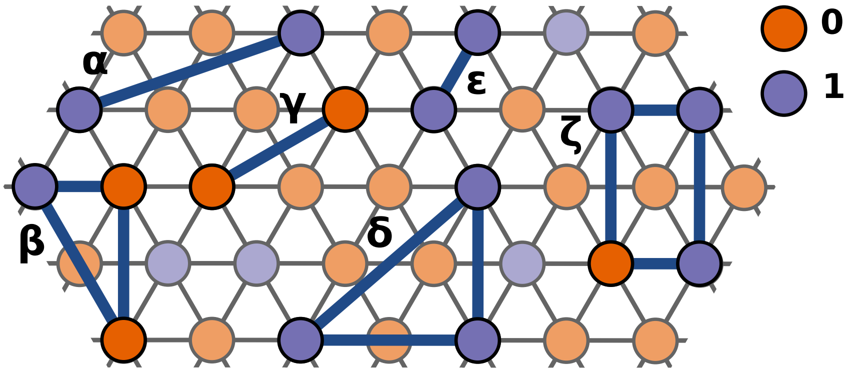

Figure 2.1: Example clusters on a triangular lattice, with two different species. Using the occupation basis, the site basis functions evaluate to 0 for orange atoms, and 1 for purple species. Cluster functions are computed by taking the product of the basis functions of their sites. For this example, clusters α, δ and ε would evaluate to 1, the rest end up as 0.

The cluster functions form a complete orthonormal basis, and a linear combination of them can be used to describe any property of the cystal that is dependent on composition. The energy of the crystal can therefore be expressed as

$$E(\vec{p}) = \sum_\alpha V_\alpha \phi_\alpha(\vec{p}) \tag{2.12}$$

The coefficients V_α are the effective cluster interactions (ECI), whose value is determined by the energy contribution to the system from its corresponding cluster of sites. For example, a large crystal of pure Ni that contains two Al atoms will have higher energy if the Al atoms are placed at nearest neighbor distances, instead of a large distance apart. If this is the case, then the ECI value for the nearest neighbor pair cluster will be higher than that of a pair with a large distance. Equation (2.12) sums over clusters of all sizes (points, pairs, triplets, etc.), but also includes a term for the "empty cluster", whose ECI is constant and independent of the atomic configuration of the crystal.

In theory, eq. (2.12) sums over all possible cluster sizes and cluster geometries. In order to determine the values of the ECI, a truncation must be made, such that only the most important cluster interactions are considered. Practically speaking, this means discarding clusters made up of many sites (usually more than 4) and long edge lengths. For typical systems, the assumption that ECI values converge rapidly is a good one, so the truncated expansion remains a good descriptor of the system energy, while retaining practicality.

2.2.1 Determination of ECI

Once the cluster expansion has been truncated, determining the value of the ECI is a simple regression problem. Solving for their values requires a set of training data. This is generated by enumerating symmetrically distinct atomic orderings on the parent crystal, and then determining their energies with DFT. The correlations for each of this configurations can also be readily determined, such that

$$\vec{y} = \boldsymbol{X}\vec{v} \tag{2.13}$$

where $\vec{y}$ is a vector containing the energies of each configuration in the training set, $\boldsymbol{X}$ is a matrix containing the correlations for each configuration (one row vector per configuration), and $\vec{v}$ is the vector of ECI values that we want to determine. The number of ECI to solve for matches the length of the correlation vectors, and is determined by how the cluster expansion is truncated. The solution for this ECI vector is expected to be sparse, so the regression problem is an underdetermined one. Indeed, when too many ECI make significant contributions to the system energy, complex unrealistic interactions appear. When this occurs, the system will predict unphysical results, which usually manifest themselves as undesired groundstates being predicted as stable orderings.

Many statistical methods exist to solve this type of regression problem. Common approaches include using Bayesian inference to shrink the ECI values (Ridge regression or L2), or induce sparsity in the solution (Lasso or L1), as well as the genetic algorithm. Injecting prior knowledge of the system into the regression can help guide the solution towards a more physical model.

2.2.2 Favoring important configurations

When parameterizing a cluster expansion, low energy configurations should inform the model more strongly than high energy ones. Of particular importance are the structures that make up the convex hull in energy-composition space, which correspond to stable orderings at 0K. The solutions for eq. (2.13) will change depending on the weighting of the training energies during the regression. A way to skew the weighting to favor low energy structures and groundstates will be presented here.

The projection of the energy of any configuration onto the convex hull can be expresses as a linear combination of the vertexes of the facet it is projected onto. If the distance from the convex hull is known, we can define

$$\vec{\Delta} = \vec{y} - \vec{y}^* \tag{2.14}$$

$\vec{\Delta}$ represents the distance from the convex hull, $\vec{y}$ represents the energy of the configuration, and $\vec{y}^*$ represents the projected energy of the configuration onto the convex hull. The vectors from 2.14 exist in a composition-energy space. $\vec{y}^*$ can now be written as a combination of the vertexes that make up the facet it lies on. Using a ternary system as an example, $\vec{y}_4$ will represent the configuration we're interested in, while $\vec{y}_1$, $\vec{y}_2$, and $\vec{y}_3$

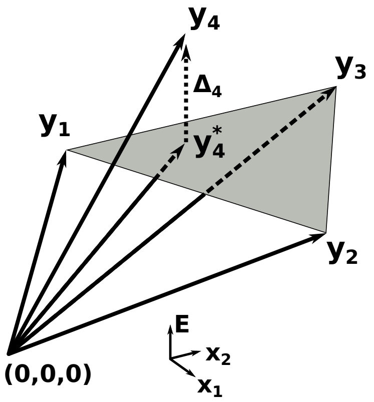

Figure 2.2: Example energies for a ternary system.

will represent the facet underneath $\vec{y}_4$. For this example,

$$\vec{y}_4^* = c_1\vec{y}_1 + c_2\vec{y}_2 + c_3\vec{y}_3 \tag{2.15}$$

The vector of weights $\vec{c}$ corresponds to the barycentric coordinates of $\vec{y}_4^*$, which falls within the simplex. We therefore have the additional constraint

$$c_1 + c_2 + c_3 = 1 \tag{2.16}$$

$$\begin{pmatrix} x_{1,4}^* \\ x_{2,4}^* \\ E_4^* \\ 1 \end{pmatrix} = \begin{pmatrix} x_{1,1} & x_{1,2} & x_{1,3} \\ x_{2,1} & x_{2,2} & x_{2,3} \\ E_1 & E_2 & E_3 \\ 1 & 1 & 1 \end{pmatrix} \begin{pmatrix} c_1 \\ c_2 \\ c_3 \end{pmatrix} \tag{2.17}$$

Though the system appears to be overdetermined, all four equations are consistent, since any point on the simplex is a weighted combination of the vertices. In order to solve for the values of $\vec{c}$, we drop the energy term, and solve:

$$\begin{pmatrix} x^*_{1,4} \\ x^*_{2,4} \\ 1 \end{pmatrix} = \begin{pmatrix} x_{1,1} & x_{1,2} & x_{1,3} \\ x_{2,1} & x_{2,2} & x_{2,3} \\ 1 & 1 & 1 \end{pmatrix} \begin{pmatrix} c_1 \\ c_2 \\ c_3 \end{pmatrix} \tag{2.18}$$

$$\begin{pmatrix} x_{1,1} & x_{1,2} & x_{1,3} \\ x_{2,1} & x_{2,2} & x_{2,3} \\ 1 & 1 & 1 \end{pmatrix}^{-1} \begin{pmatrix} x^*_{1,4} \\ x^*_{2,4} \\ 1 \end{pmatrix} = \begin{pmatrix} c_1 \\ c_2 \\ c_3 \end{pmatrix} \tag{2.19}$$

More compactly, and for an $n-1$ composition space, we can rewrite 2.19 as

$$\vec{c} = \boldsymbol{H}^{-1}\vec{x^*} \tag{2.20}$$

Here $\boldsymbol{H}$ is defined by the composition and energies of the appropriate convex hull facet, and $\vec{x^*}$ is defined by the composition of the projected configuration.

We're interested in a weight matrix $\boldsymbol{M_\Delta}$ that will skew the fit towards values of $\vec{\Delta}$ instead of values of $\vec{y}$. That is, there is some transformation $\boldsymbol{L}$ that will change the minimization problem as

$$(\vec{y} - \boldsymbol{X}\vec{v}) \xrightarrow{\boldsymbol{L}} \left(\vec{\Delta} - \boldsymbol{X}^*\vec{v}\right) \tag{2.21}$$

With $\boldsymbol{X}$ and $\vec{v}$ representing the correlation matrix and ECI respectively.

Continuing with the example of a ternary system, ignoring all configurations but one (and the additional three that make up the convex hull facet below it), we have

$$\begin{pmatrix} E_1 \\ E_2 \\ E_3 \\ E_4 \end{pmatrix} \xrightarrow{\boldsymbol{L}} \begin{pmatrix} 0 \\ 0 \\ 0 \\ \Delta_4 \end{pmatrix} \tag{2.22}$$

and since

$$\vec{\Delta}_4 = \vec{y}_4 - c_1\vec{y}_1 - c_2\vec{y}_2 - c_3\vec{y}_3 \tag{2.23}$$

we can define

$$\boldsymbol{L} = \begin{pmatrix} 0 & 0 & 0 & 0 \\ 0 & 0 & 0 & 0 \\ 0 & 0 & 0 & 0 \\ -c_1 & -c_2 & -c_3 & 1 \end{pmatrix} \tag{2.24}$$

such that

$$\boldsymbol{L}\vec{y} = \vec{\Delta} \tag{2.25}$$

$$\boldsymbol{L}\boldsymbol{X} = \boldsymbol{X}^* \tag{2.26}$$

In order to fit $\vec{v}$ exclusively by distance from the hull, we would solve for

$$\min \left(\vec{y} - \boldsymbol{X}\vec{v}\right)^{\intercal} \boldsymbol{L}^{\intercal}\boldsymbol{L} \left(\vec{y} - \boldsymbol{X}\vec{v}\right) \tag{2.27}$$

We can instead combine different weight matrices, to decide how much the distance from the hull should influence the fit. For $\boldsymbol{M}_\Delta = \boldsymbol{L}^{\intercal}\boldsymbol{L}$ and an arbitrary weight matrix $\boldsymbol{M}_x$, we can instead use scaling parameters α and β to minimize

$$\min\left(\vec{y}-\boldsymbol{X}\vec{v}\right)^{\intercal}\left(\alpha\boldsymbol{M}_{\Delta}+\beta\boldsymbol{M}_{x}\right)\left(\vec{y}-\boldsymbol{X}\vec{v}\right) \tag{2.28}$$

The same matrix $\boldsymbol{L}$ can be used to impose non-linear constraints. If we want to ensure that cluster expanded energies are predicted above the expanded energies of the convex hull, we'd like to impose

$$\boldsymbol{X}\vec{v} > 0 \tag{2.29}$$

which ensures that the expanded energies lie above the line connecting the energies of the cluster expanded energy of the groundstates.

2.2.3 Enforcing convexity of configuration sets

Using the weight matrix $\boldsymbol{L}$ to impose constraints is not enough to guarantee that the configurations that make up the convex hull of the training set will appear as predicted groundstates. Even if $\boldsymbol{X}\vec{v} > 0$, certain groundstates can be predicted to have an energy high enough that it disappears from the convex hull. The constraint only guarantees that energies will be predicted above the line connecting the predicted energies of the groundstates, but does enforce any condition on the groundstates themselves. This is evident from the fact that rows corresponding to groundstates in the weight matrix $\boldsymbol{L}$ are composed entirely of zeros.

In order to preserve the convexity of the groundstates, additional constraints need to be imposed. Specifically, for each groundstate, we want to impose that the predicted energy be below a pseudo convex hull made up of all the other groundstates. We can

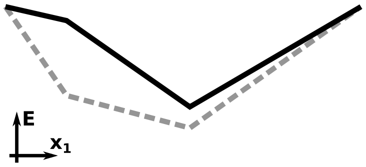

Figure 2.3: Comparison between the true convex hull (dashed) and the predicted energies of the real convex hull groundstates (connected by a solid line). Enforcing $\boldsymbol{X}\vec{v} > 0$ guarantees that all other energies will be predicted above the solid line, but does not enforce the convexity of the original groundstates.

define

$$\vec{\Delta}^{+} = \vec{y} - \vec{y}^{+} \tag{2.30}$$

$\vec{\Delta}^{+}$ represents the distance from the pseudo convex hull, $\vec{y}$ represents the energy of a groundstate, and $\vec{y}^{+}$ represents the projected energy of the groundstate onto the psuedo convex hull, constructed from all other groundstates that are not $\vec{y}$. In a similar manner to $\boldsymbol{L}$, we can write $\vec{y}^{+}$ as combination of the vertexes that make up the facet of the pseudo convex hull that lies above it. Using a binary system as an example, $\vec{y}_1$, $\vec{y}_2$. $\vec{y}_3$ and $\vec{y}_4$ will represent four configurations that fully define the convex hull of a system.

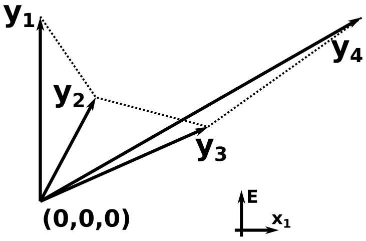

Figure 2.4: A convex hull in binary composition-energy space

For each of the groundstates that are not at the edge of the composition space, a new pseudo convex hull is constructed that can be used to calculate E^{+} in terms of a weighted average of neighboring groundstates.

$$\vec{y}_3^{+} = c_2\vec{E}_2 + c4\vec{E}_4 \tag{2.31}$$

The set of barycentric coordinates c_i is calculated in the same manner as shown in 2.17. For each groundstate, a new set of barycentric coordinates is calculated, each of which can be used to create a row in a matrix $\boldsymbol{Q}$, which converts the problem as

$$(\vec{y} - \boldsymbol{X}\vec{v}) \xrightarrow{\boldsymbol{Q}} \left(\vec{\Delta}^{+} - \boldsymbol{X}^{+}\vec{v}\right) \tag{2.32}$$

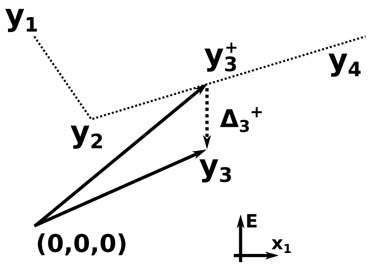

Figure 2.5: The pseudo hull constructed by excluding $\vec{y}_3$ from the set. The value of $\vec{y}_3^{+}$ is calculated as a weighted sum of $\vec{y}_2$ and $\vec{y}_4$, which make up the vertexes of the pseudo convex hull facet above.

The resulting matrix Q for the binary example is

$$\boldsymbol{Q} = \begin{pmatrix} 0 & 0 & 0 & 0 \\ -c_1 & 1 & -c_3 & 0 \\ 0 & -c_2 & 1 & -c_4 \\ 0 & 0 & 0 & 0 \end{pmatrix} \tag{2.33}$$

such that

$$\boldsymbol{Q}\vec{y} = \vec{\Delta}^{+} \tag{2.34}$$

$$\boldsymbol{Q}\boldsymbol{X} = \boldsymbol{X}^{+} \tag{2.35}$$

The matrix $\boldsymbol{Q}$ can be used both as a weight matrix and to enforce an additional set of non-linear constraints. When used as a weight matrix as shown in 2.28, $\boldsymbol{Q}$ will skew the fit to emphasize the relative predicted energy values of the true groundstates. $\boldsymbol{Q}$ can also be used to enforce the condition

$$\boldsymbol{X}^{+}\vec{v} < 0 \tag{2.36}$$

which will enforce that the set of configurations used to construct $\boldsymbol{Q}$ remains convex. In the simplest usage case, $\boldsymbol{Q}$ is constructed using the true convex hull as the set of configurations that should retain convexity. Combining 2.29 and 2.36 as constraints will guarantee that the convex hull of the predicted energies is made up of the same configurations as the original data set: while $\boldsymbol{Q}$ enforces the relative positions of the predicted energies of the groundstates, $\boldsymbol{L}$ ensures that all other configurations are predicted above the desired convex hull.

2.3 Monte Carlo methods and statistical mechanics

The macroscopic thermodynamic properties of a solid at equilibrium are an ensemble average of the microstates of the system. The term microstate here refers to a particular excitation that is accessible by the system, which might be configurational, vibrational, etc. At finite temperature, the system will find itself fluctuating between between these microstates, each with a particular energy $\Omega(\sigma)$, where σ refers to a particular microstate. The precise definition of Ω depends which thermodynamic variables of the system are being controlled, such as temperature, composition, or chemical potential. As an example, for the Canonical ensemble, where the composition, volume, and temperature are controlled, $\Omega\left(\sigma\right) = E\left(\sigma\right)$.

The probability that the solid is at a particular microstate σ is given by

$$P(\sigma) = \frac{1}{Z} e^{-\Omega(\sigma)/k_B T} \tag{2.37}$$

where k_B is the Boltzmann constant, and Z is the appropriate partition function for the controlled variables, defined as

$$Z = \sum_{\sigma} e^{-\Omega(\sigma)/k_B T} \tag{2.38}$$

This partition function is essentially a probability distribution for different microstates, from which we can determine how much each microstate contributes to the ensemble average of a macroscopic quantity. That is, for any thermodynamic quantity $X(\sigma)$, the value X of the system is given by

$$X = \sum_{\sigma} X(\sigma) P(\sigma) \tag{2.39}$$

Once a predictive model for the system has been constructed, formation energies for arbitrary configurations (i.e. microstates σ) can be rapidly calculated. However, a direct evaluation of the partition function of a system remains unfeasible, even for relatively small supercells, given the exponential growth of available microstates with number of atoms. Instead, Monte Carlo techniques can be employed to sample the ensemble with the Blotzmann probability that defines the system. Over a long enough period of time, the ensemble averages of the Monte Carlo sampling will converge to the ensemble averages of the full partition function.

2.3.1 Grand Canonical ensemble

In the Monte Carlo method, different microstates resulting from a Markov chain evolution of configurations are sampled. The Metropolis algorithm is used, where the transition from a starting configuration A to B is determined by the difference in relative energies $\Delta\Omega^{A\rightarrow B} = \Omega\left(\sigma^{B}\right) - \Omega\left(\sigma^{A}\right)$. If $\Delta\Omega^{A\rightarrow B} < 0$, then the system evolves into configuration B, and $P^{A\rightarrow B} = 1$. Otherwise, the new configuration B is accepted with a Boltzmann probability, such that

$$P^{A\rightarrow B} = e^{-\Delta\Omega^{A\rightarrow B}/k_B T} \tag{2.40}$$

In the Grand Canonical ensemble, the chemical potential μ of all species is controlled, and so

$$\Omega\left(\sigma\right) = E\left(\sigma\right) - \sum_{i} \mu_i N_i \tag{2.41}$$

where i is counting over each species in the system, and N represents the number of atoms present.

By consistently sampling thermodynamic variables as the system evolves, ensemble averages of almost all thermodynamic variables can be taken. As such, the values of Ω, E and N are readily determined. However, of most interest is the Gibbs free energy $G = E - TS$ (the PV term is absent due to they system being at zero pressure), which requires knowledge of the entropy S of the system. Though S cannot be measured directly, integration techniques can be used to extract the desired free energies.

If we define the Grand Canonical free energy as

$$\Phi = G - \sum_{i} \mu_i N_i \tag{2.42}$$

then

$$d\left(\Phi\beta\right) = Ed\beta - \beta\sum_i N_i d\mu_i - \sum_i \mu_i N_i d\beta \tag{2.43}$$

where $\beta = 1/k_B T$. The values for Φ can be found via different integration pathways. If the integration is done along constant temperature values and only one chemical potential is allowed to vary

$$\Phi^F = -\int_{\mu^I}^{\mu^F} N d\mu + \Phi^I \tag{2.44}$$

Conversely, if all chemical potential values are fixed, and the integration is done along temperature

$$\Phi^F = \frac{1}{\beta^F}\left[\int_{\beta^I}^{\beta^F} \Omega d\beta + \Phi^I\beta^I\right] \tag{2.45}$$

The superscripts of eq. (2.44) and eq. (2.45) denote the values at an initial reference state (I) and the final value at the end of the integration (F).

These integrations require a starting value Φ^I, which can be approximated by taking extreme values for μ, or starting the integration at very low temperatures. For both these cases $\Phi \approx \Omega$, and can be readily determined.

2.3.2 Kinetics

Kinetic coefficients relating do macroscopic diffusional processes can also be determined by Monte Carlo techniques. The process for this involves creating a simulation cell where at least one vacancy is present, and tracking the trajectories of each atom, as well as the amount of time elapsed. In this model, diffusion in a crystal is mediated through vacancy exchange events with neighboring atoms that occur at particular frequencies. The frequency with which a particular hop occurs is given by

$$\Gamma^{I\rightarrow F} = v^* e^{-\Delta E_b/k_B T} \tag{2.46}$$

Here $\Gamma^{I \to F}$ is the frequency associated with hopping from an initial state to a final one; v^* is a vibrational prefactor, determined through Vineyard's formula; and ΔE_b is the activation energy required for the hop to occur.

In the Ni-Al system, diffusional processes of the β phase are known to involve unusual vacancy exchange mechanisms, such as second nearest neighbor exchange, and the energy pathway of the diffusion paths may involve local minima. The diffusion calculations of this thesis focus on the γ and γ' phases, which are generally well behaved. An example of the energy pathway for a hop in these phases is shown in fig. 2.6.

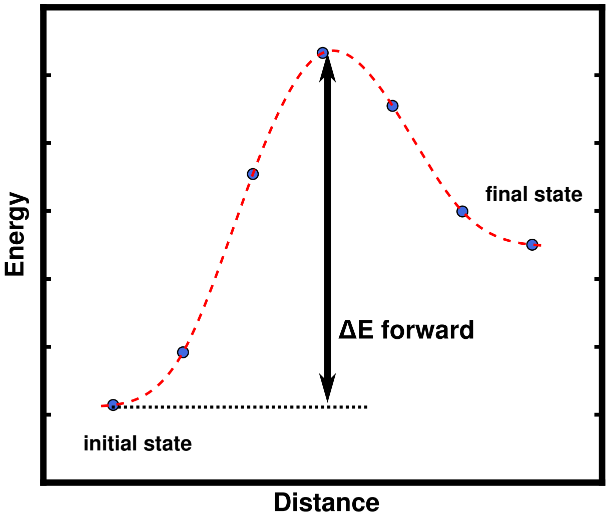

Figure 2.6: Example of energy pathway for a diffusion hop. In order to go from the initial state to the final one, the activation energy must be overcome.

The evolution of the diffusional processes therefore requires knowledge of what these activation barriers are, which depend both on which species is hoping, and the local environment around the hop pathway. More details on how to determine these values will be laid out in chapter 5, suffice it to say for this section that the hop frequencies of eq. (2.46) can be modelled with a cluster expansion in an analogous manner as the formation energies of atomic configurations.

Transitions from one configuration to another are determined by evaluating the frequencies Γ of every possible event that is possible for the current configuration. This means determining all the possible hops that can occur, and calculate each of their associated frequencies. In the case of a systems like the FCC phases of Ni-Al, the equilibrium vacancy concentration is on the order of 10^{-5}. A typical simulation cells contains on the order of 10^3 sites, so only a single vacancy is present during in the KMC cell. As a result, there is always a total of 12 possible events during the entirety of the simulation, one for each of the nearest neighbors of the vacancy in the FCC crystal.

The probability of a particular event being selected is proportional to its hop frequency, such that

$$P\left(\Gamma_i\right) = \frac{\Gamma_i}{\sum_j \Gamma_j} \tag{2.47}$$

where the sum counts over all possible events of the crystal for the current atomic configuration. Using a uniform random number $u \in (0, 1]$, an event is chosen with the weighted probability of eq. (2.47). The atomic positions of the participating atoms are then updated, while recording their changes in trajectories, as well as the time step associated with the event. The expected amount of time that would need to elapse for the hop to take place is given by

$$\Delta t = \frac{\ln(1/u)}{\Gamma_i} \sum_j \Gamma_j \tag{2.48}$$

A visual representation of a KMC event is given in fig. 2.7. Each of the 6 possible events for in this example has a different hop frequency, which is lined up and normalized. Choosing a random value u is like choosing a random position on the line of frequencies, which determines which event is selected. After the site occupant are updated, frequencies for the newly available events are calculated, and the process is repeated.

With each successive event, trajectories of each of the atoms grows longer and longer, as does the accumulated elapsed time of the simulation. After enough vacancy hops, kinetic properties can start being measured, such as the kinetic Onsager coefficients,

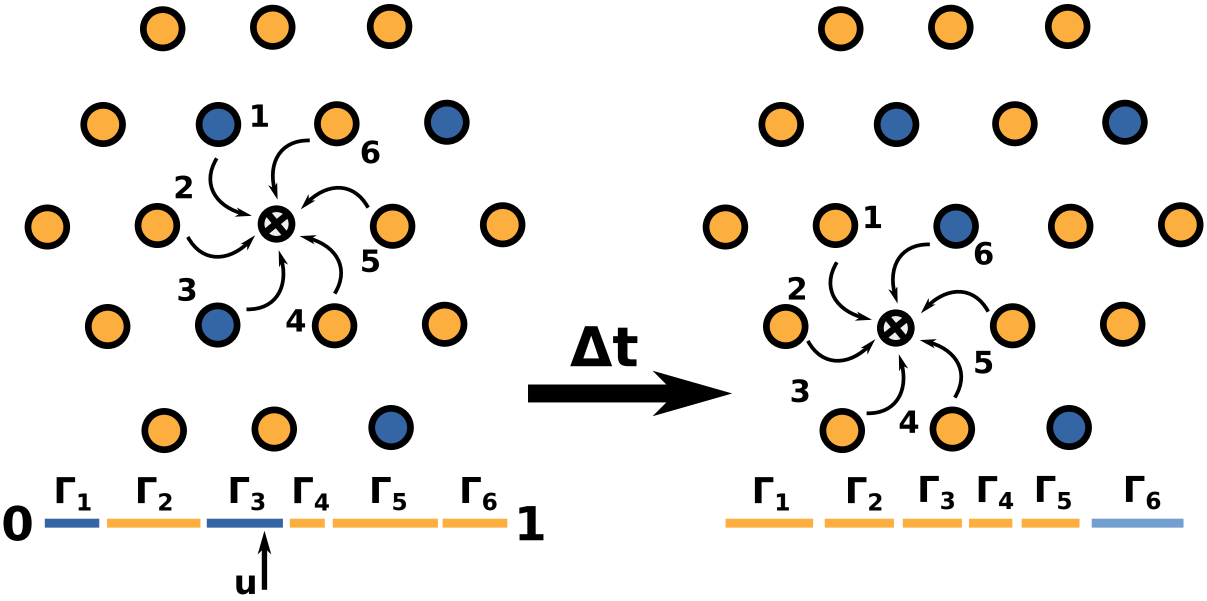

Figure 2.7: Schematic of how a KMC event is selected. A particular event is chosen with a weighted probability, with higher frequency events more likely to be chosen. Once the event is chosen, atomic positions and the clock are updated. The process is repeated with using the new hops that are possible.

correlation factors, or self diffusion coefficients. Once those properties are measured, the values of the trajectories and elapsed time are flushed out, and the process begins again. By sampling values periodically, the measured kinetic values will converge, and these values can be used to derive more useful diffusion metrics. The details and definitions of the values being measured explored in more detail in chapter 6, as well as how useful properties can be derived from them.

Chapter 3

The Ni-Al binary[1]

3.1 Introduction

Nickel based superalloys have found a wide range of industrial applications thanks to their high temperature mechanical properties and corrosion resistance [7]. The Ni-superalloys of turbine engines for propulsion and power generation usually contain many alloying additions, but primarily build on the Ni-Al binary. This binary has been studied extensively and contains a variety of intermetallic compounds with unique properties. The Ni rich phases of the Ni-Al binary are all orderings on an FCC parent crystal structure and include the Ni rich solid solution, γ, the γ'-Ni_3Al phase having $L1_2$ ordering and the Ni_5Al_3 phase. FCC ordering gives way to BCC orderings at equiatomic mixtures of Ni and Al where the β phase having B2 ordering on a BCC parent crystal structure is favored. Coherent two-phase mixtures consisting of γ and γ' are used to realize high strength and creep resistance at elevated temperatures [17], while the β phase, having favorable oxidation behavior, is used as a bond coat on turbine engine blades made of a superalloy core [25, 26].

---

[1] The contents of this chapter have been substantially reproduced from J. G. Goiri and A. Van der Ven, *Phase and structural stability in Ni-Al systems from first principles*, *Physical Review B* **94** (Sept., 2016)

In contrast to most intermetallic compounds, the β phase can tolerate a high degree of off-stoichiometry through the introduction of antisite defects and vacancies [27]. β-NiAl accommodates excess Ni by forming antisite Ni defects on its Al sublattice. Ni rich β phases are susceptible to a martensitic transformation upon quenching [28], whereby the high temperature, Ni-rich B2 ordering on BCC transforms to an FCC variant through a diffusionless process [29, 30, 31]. Many fundamental questions remain about the thermodynamics and kinetics of these martensitic transformations. Excess Al in β-NiAl, in contrast, is realized with Ni vacancies on the Ni sublattice of the B2 ordering and can reach unusually high vacancy concentrations for an intermetallic compound. In fact the high vacancy concentrations can lead to vacancy ordering within the B2 crystal structure, however, the phase relations among the various vacancy ordered derivatives have yet to be established.

Here we report on a combined first-principles density functional theory (DFT) and statistical mechanics study of phase stability in the Ni-Al binary. We focus in particular in elucidating the thermodynamic properties of the Ni-Al binary at concentrations where the alloy transitions from FCC to BCC. To this end, we introduce strain order parameters to determine the onset of instabilities between FCC and BCC based orderings along the Bain path. These instabilities are discussed in the context of the observed martensitic transformation, which has been the subject of both experimental [30, 29, 32] and computational [33] work. We also investigate the thermodynamic properties associated with vacancy ordering over the Ni-sublattice of Al-rich β-NiAl and discover the stability of a family of hybrid phases that combine features of $L1_0$ and $L1_2$ in the Ni rich half of the Ni-Al binary.

3.2 Methods

3.2.1 DFT calculations

First-principles density functional theory (DFT) calculations were performed to predict ordering preferences in the Ni-Al binary and to investigate instabilities with respect to the Bain path. All first-principles calculations were performed within the generalized gradient approximation (GGA-PBE) using the projector augmented wave (PAW) pseudopotential method [34] as implemented in the Vienna ab initio Simulation Package (VASP) [35, 36, 37]. The CASM [38, 39, 27, 40, 41] software package was used to enumerate symmetrically distinct orderings over FCC and BCC, allowing Ni and Al to occupy the FCC lattice, and Ni, Al and vacancies to occupy the sublattices of a BCC based B2 ordering. A k-point mesh of $23 \times 23 \times 23$ was found to converge the energy of a FCC primitive Ni cell to within 1meV per atom, while a density of $17 \times 17 \times 17$ was found to do the same for a NiAl B2 cell. The k-point meshes for the configurations enumerated in supercells of FCC Ni and of B2 NiAl were scaled appropriately to maintain the same k-point density. All DFT-PBE calculations were initialized with a spin polarized ferromagnetic ordering [42]. To ensure accuracy in our calculations, a plane wave energy cutoff of 560eV was used. Numerical k-space integration through the Brillouin zone was performed using a smearing parameter of 0.2eV with the Methfessel-Paxton method (first order). The DFT-PBE energies were calculated allowing atomic positions and lattice parameters to relax to minimize the total energy.

3.2.2 Metrics of relaxation and Bain instabilities

With the exception of Al_3Ni, every phase in the Ni-Al binary can be described as an ordering over either an FCC or BCC lattice. Most orderings over FCC or BCC break the original cubic symmetry of their parent crystal. These configurations therefore relax into structures that lack the initial connectivity between atoms of their ideal parent crystal structure. Every atom in FCC, for example, has exactly 12 nearest neighbors, while each atom in BCC has 8 nearest neighbors. Upon relaxation, the atomic connectivity of configurations with broken symmetry usually differ only slightly from that in the undistorted starting crystal, largely retaining the same number of nearest neighbors within a small tolerance. These configurations are dynamically stable and represent the lowest energy state for that ordering on the starting parent crystal structure. However, particular decorations on FCC and BCC may be dynamically unstable, undergoing significant deformation when relaxing atomic coordinates and lattice vectors during energy minimization. They change their connectivity to the point that the resulting structure more closely resembles a different parent crystal structure from the one they started on.

Strain can serve as an order parameter to track the extent of lattice relaxation. A reference lattice with vectors $\vec{a}$, $\vec{b}$ and $\vec{c}$

$$\mathbf{L} = \begin{bmatrix} a_x & b_x & c_x \\ a_y & b_y & c_y \\ a_z & b_z & c_z \end{bmatrix} \tag{3.1}$$

is related to a deformed lattice $\mathbf{L}'$ by a deformation gradient tensor $\mathbf{F}$ according to

$$\mathbf{L}' = \mathbf{F}\mathbf{L}. \tag{3.2}$$

This deformation tensor can be factored into a rotation $\mathbf{R}$ and a symmetric stretch tensor $\mathbf{U}$ using polar decomposition as

$$\mathbf{F} = \mathbf{R}\mathbf{U}. \tag{3.3}$$

Because $\mathbf{R}$ corresponds to a rigid body rotation, the energy of the crystal is unaffected by it, and any metric of strain should depend only on the stretch tensor $\mathbf{U}$. The rotation $\mathbf{R}$ can be eliminated by multiplying $\mathbf{F}$ by its transpose (since $\mathbf{R}^{-1} = \mathbf{R}^{\intercal}$), yielding the commonly used right Cauchy-Green stretch tensor[43]

$$\mathbf{U}^2 = \mathbf{F}^{\intercal}\mathbf{F} \tag{3.4}$$

There are several strain tensors that can be defined in terms of the stretch tensor $\mathbf{U}$. In this study, we use the Hencky strain defined as

$$\mathbf{E} = \ln \mathbf{U}. \tag{3.5}$$

Similar to $\mathbf{U}$, this strain metric is also symmetric, with only 6 independent strain components

$$\mathbf{E} = \begin{bmatrix} \varepsilon_{xx} & \varepsilon_{xy} & \varepsilon_{xz} \\ \varepsilon_{xy} & \varepsilon_{yy} & \varepsilon_{yz} \\ \varepsilon_{xz} & \varepsilon_{yz} & \varepsilon_{zz} \end{bmatrix} = \mathbf{E}^{\intercal} \tag{3.6}$$

However, instead of working directly with the six independent Hencky strain elements of eq. (3.6), it is more convenient to use an equivalent set of symmetry adapted strain metrics defined as linear combinations of the Hencky strains according to [44]:

$$e_1 = \frac{\varepsilon_{xx} + \varepsilon_{yy} + \varepsilon_{zz}}{\sqrt{3}} \tag{3.7}$$

$$e_2 = \frac{\varepsilon_{xx} - \varepsilon_{yy}}{\sqrt{2}} \tag{3.8}$$

$$e_3 = \frac{2\varepsilon_{zz} - \varepsilon_{yy} - \varepsilon_{xx}}{\sqrt{6}} \tag{3.9}$$

$$e_4 = \sqrt{2}\varepsilon_{yz} \tag{3.10}$$

$$e_5 = \sqrt{2}\varepsilon_{xz} \tag{3.11}$$

$$e_6 = \sqrt{2}\varepsilon_{xy} \tag{3.12}$$

e_1 is a measure of dilation, and is proportional to the volume change provided the Hencky strain metric is used. It is for this reason that we use the Hencky strains, as it uncouples any volume dependence from e_2-e_6. The e_2 and e_3 strains together describe tetragonal and orthorhombic distortions of the crystal, while the e_4,e_5 and e_6 strains represent shears.

A common instability for both FCC and BCC based orderings is the Bain path. The above symmetry adapted strain metrics enable a representation of all symmetrically equivalent Bain paths that connect FCC to BCC in the two dimensional space spanned by e_2 and e_3. A conventional FCC cell with its cubic axes oriented along the x-y-z Cartesian directions can be transformed to BCC by a contraction along the z direction and a simultaneous expansion along the x and y directions. The Bain path along the z axis is most easily visualized with a 2 atom tetragonal FCC unit cell as shown in fig. 3.1. There are three symmetrically equivalent Bain paths as a result of the cubic symmetry of an FCC crystal. Equivalent transformations can be realized by contracting along the y direction and expanding along the z and x directions, or by contracting along the x direction and expanding along the y and z directions. The Bain path involving a compression along the z-direction (fig. 3.1) follows the negative e_3 axis, holding e_2=0 when using FCC as a reference for strain. The two other symmetrically equivalent Bain paths follow the dashed lines of fig. 3.2, which are related to the e_3 axis by 120° rotations in e_2-e_3 space. The dashed lines in e_2-e_3 space in fig. 3.2 correspond to tetragonal distortions of the reference FCC lattice, while any other points that deviate from these lines correspond to orthorhombic distortions of FCC. When using Hencky strains, any distortion corresponding to a path in this space at fixed e_1 occurs at constant volume.

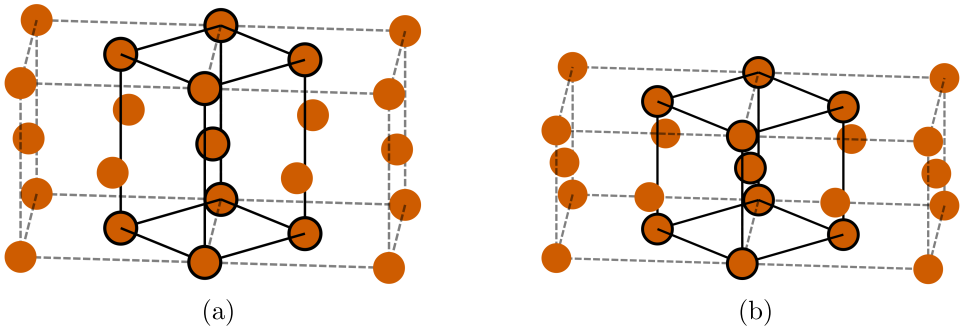
(a)

(b)

Figure 3.1: A Bain transformation from a FCC (fig. 3.1a) to a BCC (fig. 3.1b) crystal structure. The transformation of this FCC ordering corresponds to a path in the negative e_3 direction.

Strain transformations from BCC to FCC can also be mapped out in e_2-e_3 space using the BCC crystal as the reference to measure strain. The axes of the conventional cubic BCC unit cell must be aligned along the x-y-z directions. The BCC crystal then resides at the origin in e_2-e_3 space. The pathways are the same as the Bain paths described for FCC, but are taken in the opposite direction: a path in the positive e_3 direction with no e_2 contribution results in an expansion in the z direction and a contraction in the x and y directions. There are three equivalent paths in e_2-e_3 space that convert BCC into FCC. These paths are also related to each other by 120° rotations in e_2-e_3 space as illustrated in Figure 3(b).

While the Bain path can be fully described in terms of strains, many other paths connecting a pair of parent crystal structures combine a lattice strain with an internal shuffle of the basis atoms within the unit cell. An example is the Burgers path [45],

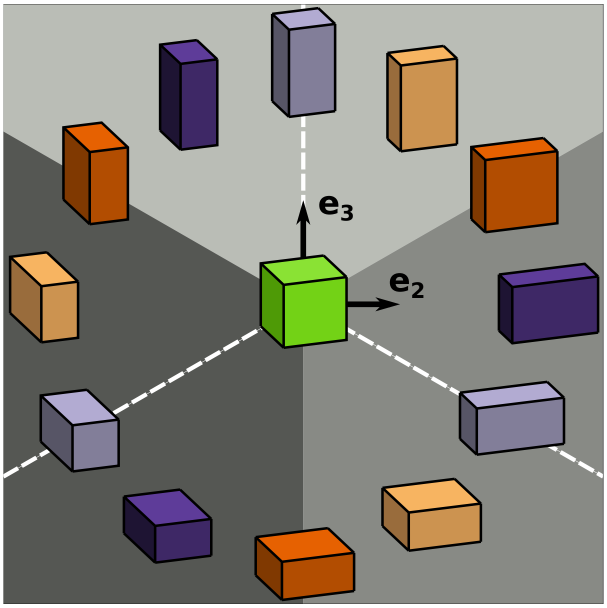

Figure 3.2: Schematic of the possible deformations in e_2-e_3 space relative to a cube. All deformations preserve the volume of the reference structure, with distortions along dashed lines being purely tetragonal. Shapes that share the same color have had a symmetrically equivalent deformation applied along different directions, resulting in identical structures that differ only by a spatial rotation.

which connects BCC to HCP. To map relaxed orderings onto their closest parent crystal structure, we therefore rely on a composite score that is a function of both the strain (deformation) of the unit cell vectors as well as the displacements of the basis atoms within the unit cell. A deformation score is defined as proportional to the sum of the squares of the Biot strain after removal of any volumetric expansion or contraction, i.e. $\mathbf{U}/\det(\mathbf{U}) - \mathbf{I}$ where $\mathbf{U}$ is the symmetric stretch tensor and $\det(\mathbf{U})$ relates the relaxed volume to the reference volume. A displacement score is defined as the sum of the squares of the displacements (normalized by the number of atoms in the unit cell) relative to the ideal positions of the prototype crystal having relaxed unit cell vectors. A weighted sum of the deformation and displacement score is then used to assign a relaxed configuration to the prototype it most closely maps onto. An in depth description can be found in the work of Thomas et al [46].

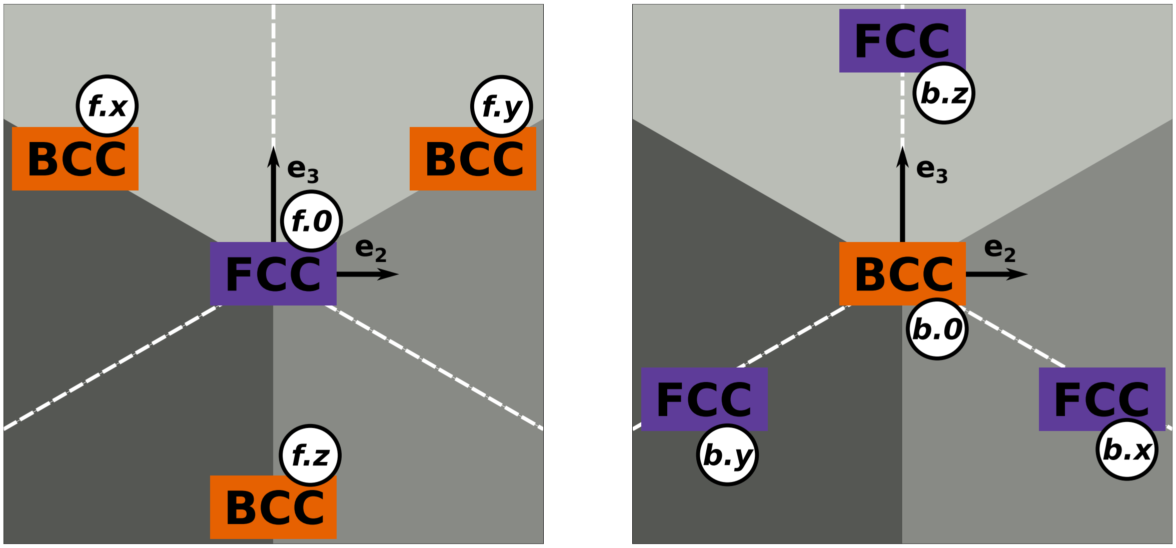

(a) (b)

Figure 3.3: Bain paths relative to FCC (fig. 3.3a) and BCC (fig. 3.3b) structures in e_2-e_3 space holding all other strain metrics constant. The origin represents the unstrained crystal and can take three symmetrically equivalent Bain paths to transform from FCC/BCC to BCC/FCC. The locations in e_2-e_3 space that correspond to FCC and BCC structures are labelled for reference throughout this work. The origin (reference structure) is indicated by a "*0*", while strain values at the end of equivalent Bain paths are indicated by "x", "y" or "z". Labels beginning with "f" correspond to strain values relative to a FCC structure, while labels beginning with "b" correspond to strains relative to BCC.

In this study, we compared all relaxed configurations to ideal FCC, BCC and HCP parent crystal structures. In the strictest sense, the great majority of orderings will not be perfect FCC, BCC or HCP, as they will lack cubic and hexagonal symmetry. Nevertheless, we will refer to relaxed orderings as FCC, BCC or HCP depending on which of these parent crystal structures they are most closely related to.

3.2.3 Cluster Expansion Method

Phase stability at finite temperature was studied using cluster expansions to extrapolate first-principles DFT energies within Monte Carlo simulations. A cluster expansion describes the energy of a multicomponent crystal as a function of its degree of order/disorder. For binary solids, occupation variable σ_i are assigned to each crystal site i that take on a value of 0 or 1 depending on the occupant of the site (e.g. Ni vs Al). A particular arrangement over the N-sites of a crystal is then specified by the collection of occupation variables $\vec{\sigma} = \{\sigma_1, \sigma_2, \cdots, \sigma_N\}$. The dependence of the energy of the crystal on arrangement, $\vec{\sigma}$, can be written as [47, 48, 49]

$$E_f\left(\vec{\sigma}\right) = \sum_{\alpha} V_\alpha \phi_\alpha\left(\vec{\sigma}\right) \tag{3.13}$$

where ϕ_α are cluster basis functions defined as

$$\phi_\alpha\left(\vec{\sigma}\right) = \prod_{i \in \alpha} \sigma_i \tag{3.14}$$

and correspond to products of occupation variables belonging to sites of clusters α, which include point, pair, triplet etc. clusters. The coefficients V_α are expansion coefficients called effective cluster interactions (ECI) and need to be determined from first principles.

While the sum in Eq. 3.13 extends over all clusters of sites α within the crystal, to be practical, it must be truncated at a particular cluster size and radius. The ECI of Eq. 3.13 can then be fit to the DFT energies of a set of symmetrically distinct configurations using one of several inversion methods [50, 51]. First-principles parameterized cluster expansions usually require only a relatively small number of nonzero ECI to accurately predict the formation energy of any configuration. With an accurate cluster expansion it is possible to rapidly evaluate the formation energy within Monte Carlo simulations to calculate thermodynamic averages. In this study of the Ni-Al binary, two cluster expansions were constructed, one for the FCC parent crystal and one for sublattice disorder in B2, which it self is an ordering over the BCC parent crystal structure. The construction and parameterization of the cluster expansion and the Monte Carlo simulations were performed with the CASM software package [38, 39, 27, 40, 41].

3.3 Results

3.3.1 Formation Energies

The first step to understanding the thermodynamics of the Ni-Al system from first principles is to establish the ground states at zero Kelvin. A large number of orderings on the FCC and BCC lattice were systematically enumerated within symmetrically distinct supercells. FCC configurations were enumerated from a one atom FCC primitive cell, allowing either Ni or Al to occupy each site. BCC configurations were enumerated relative to a B2 (2 atom) primitive cell. Previous studies[27, 52, 53, 54, 15] showed that off stoichiometry in B2 NiAl is accommodated by vacancies on the Ni sublattice and by Ni antisite defects on the Al sublattice. For this reason, the occupancy of the enumerated BCC configurations were limited to allow Ni-Va disorder on one sublattice and Al-Ni disorder on the other.

Figure 3.4 shows the calculated formation energies of all enumerated configurations over FCC and B2. Formation energies were calculated relative to pure FCC Ni and FCC Al, and were normalized per number of atoms according to

$$E_f = \frac{E^{DFT} - N_{Al}E^{DFT}_{Al} - N_{Ni}E^{DFT}_{Ni}}{N_{Al} + N_{Ni}} \tag{3.15}$$

Throughout we will use atomic fraction, defined as

$$x_{Ni} = \frac{N_{Ni}}{N_{Ni} + N_{Al}} \tag{3.16}$$

as our composition variable. The vertices of the convex hull (dashed line in fig. 3.4) of the formation energies correspond to the lowest energy groundstates, which are line compounds at 0 K.

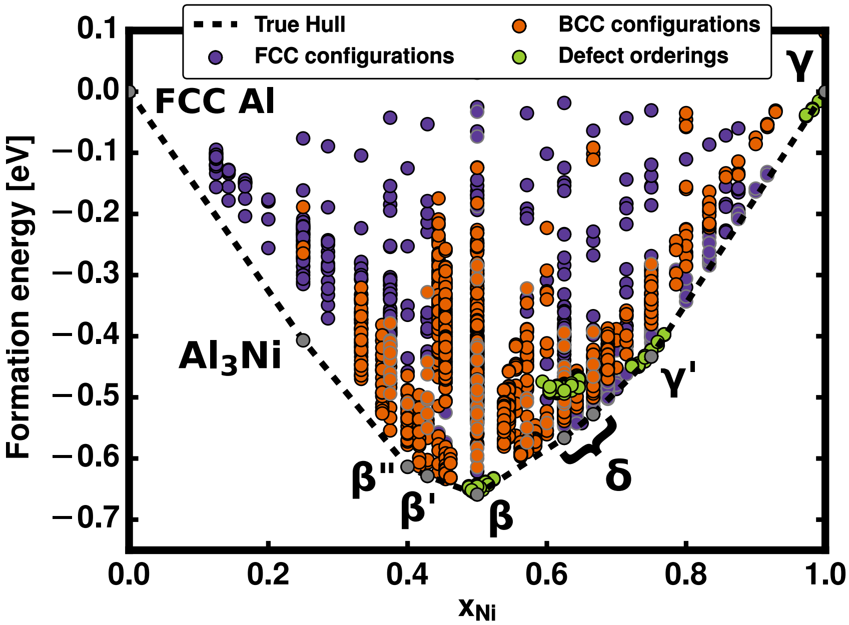

Figure 3.4: Calculated formation energies relative to FCC Ni and FCC Al. Configurations stable as a BCC structure are shown in orange, while configurations stable as a FCC structure are shown in purple. Groundstates have been colored gray and are connected by the convex hull of the energies.

Pure Ni ($x_{Ni} = 1$) is stable in the FCC crystal structure. At finite temperature it can dissolve Al, forming the Ni rich solid solution that is referred to as the γ phase. The next vertex of the convex hull at $x_{Ni} = 0.75$ in Figure 3.4 is the L1_2 ordering, commonly referred to as γ'. The unit cell for this ordered phase can be constructed by replacing the corners of a Ni FCC conventional cell with Al, which preserves cubic symmetry (fig. 3.5b). The ground state at x_{Ni}=0.625 has orthorhombic symmetry and corresponds to the experimentally characterized phase Ni_5Al_3 [27, 30], referred to in this work as δ. In addition to δ and γ', there is a large number of configurations between x_{Ni}=0.625 and 0.75 that also have low formation energies. One of these configurations, having a composition of $x_{Ni} = \frac{2}{3}$, is a groundstate, residing on the convex hull. Many others have energies that are only several meV above the convex hull. We elaborate on the orderings of these structures and their relation to the δ phase in section 3.3.2.

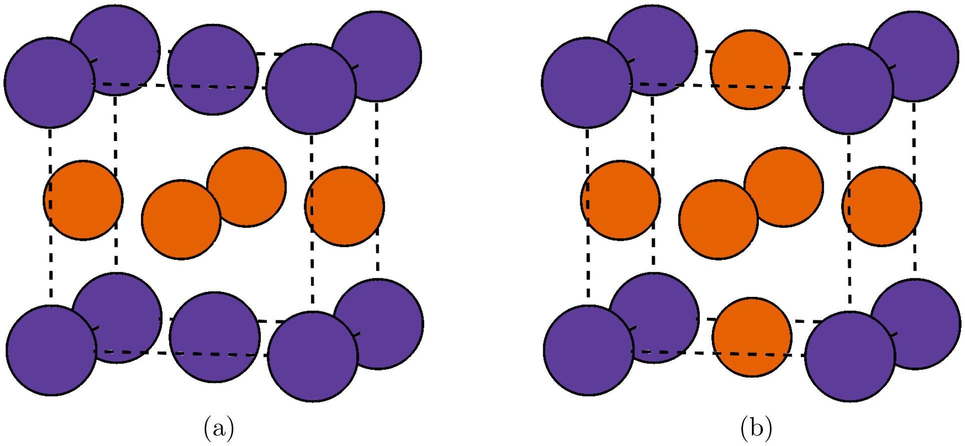
(a) (b)

Figure 3.5: Unit cells for the unstable $L1_0$ ordering (fig. 3.5a) and the $L1_2$ ordering of the γ' phase (fig. 3.5b). The ordering of $L1_0$ on the FCC crystal reduces the symmetry from cubic to tetragonal, while $L1_2$ preserves cubic symmetry. Ni atoms are shown in orange, while Al atoms are shown in purple.

The next set of ground states are all BCC based orderings. At $x_{Ni} = 0.5$, perfect B2 ordering is stable in which the corners of a conventional BCC unit cell are occupied by Ni and the body center is occupied by Al. Remarkably, two additional B2 derived ground states exist that are Al rich. Both can be viewed as B2 superstructures with vacancy ordering over the Ni sublattice. The first, having chemical formula Ni_3Al_4, has cubic symmetry, a full Al sublattice, and vacancy pairs ordered in a three dimensional pattern. This ordering requires a $4 \times 4 \times 4$ B2 supercell and was not enumerated directly, but was taken from the work of Ellner et al [55]. It is isostructural with the Ni_3Ga_4 compound. The vacancies are arranged in such a manner that any row of the Ni sublattice in B2 along any of the x, y or z directions has three filled sites followed by a single empty one, as shown in fig. 3.6c. The second B2 derived ground state, having chemical formula Ni_2Al_3, is even more Al rich as a result of a higher vacancy concentration on the Ni sublattice. The vacancy ordering in Ni_2Al_3 is achieved by removing every third Ni layer of B2 along the {111} direction. In the literature, stoichiometric B2-NiAl is referred to as the β phase. In view of their similarity to B2, we will refer to Ni_3Al_4 and Ni_2Al_3 as β' and β'' respectively in the remainder of the text.

The final intermetallic ground state, Al_3Ni, is distinctly different from all the other phases of the Ni-Al binary as it cannot be mapped to a particular ordering on FCC or BCC. Instead, it has the $D0_{20}$ structure, which is isomorphic with Fe_3C (cementite) and has orthorhombic symmetry.

As with pure Ni, pure Al is also stable in FCC. In contrast to pure Ni and the intermetallic compounds in the Ni-Al binary, though, FCC Al has a low melting temperature of around 660°C.[14]

In addition to enumerating different orderings in small supercells (containing up to 8 atoms for FCC and 16 atoms for BCC), we also systematically enumerated anti-site defects in large supercells of the ground state orderings. Supercells of $L1_2$, B2 and δ were perturbed with point, pair and triplet antisite defects. To minimize interactions between periodic images of the anti-site defects, supercells containing 108 atoms for $L1_2$, 96 atoms for δ, and 128 atoms for B2 were used. The formation energies for these orderings are depicted in green in fig. 3.4 and fig. 3.7. While the formation energies of supercells containing anti-site defects are normalized by the number of atoms in the supercell and their distance from the convex hull is not a direct measure of anti-site defect formation energies, fig. 3.4 and fig. 3.7 clearly show a large qualitative difference in anti-site defect formation energies between $L1_2$ and B2 on the one hand, and δ on the other. The formation energies for dilute antisite defects in $L1_2$ and B2 supercells all have values that are only slightly above the convex hull. The opposite is true for anti-site defects in δ, which have formation energies that are substantially above the convex hull. This suggests that while $L1_2$ and B2 may tolerate anti-site disorder at elevated temperature, δ will not and will behave as a line compound.

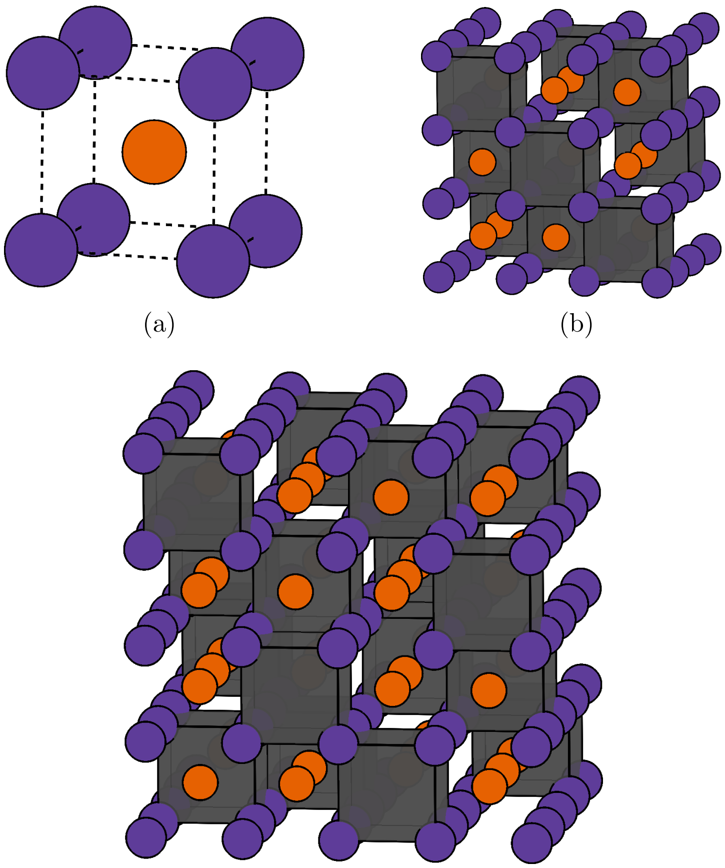

(a) (b)

(c)

Figure 3.6: Unit cells for the β (fig. 3.6a), β' (fig. 3.6c) and β'' (fig. 3.6b) phases. All three phases have an underlying B2 ordering, with Ni (orange) and Al (purple) atoms arranged on a BCC crystal. The β' and β'' phases have ordered vacancies on the Ni sublattice, shown with black boxes.

3.3.2 An infinity of groundstates

The calculated formation energies of Figure 3.4 and Figure 3.7 show that there are a large number of configurations between $0.625 < x_{Ni} < 0.75$ having formation energies that lie below the common tangent between δ at x_{Ni}=0.625 and γ' at x_{Ni}=0.75. The final relaxed crystal structures for each of these configurations were found to most closely map onto FCC. Examination of their atomic positions and arrangements revealed that they can be viewed as hybrids of L1_0 and L1_2 orderings. The crystal structures of L1_0

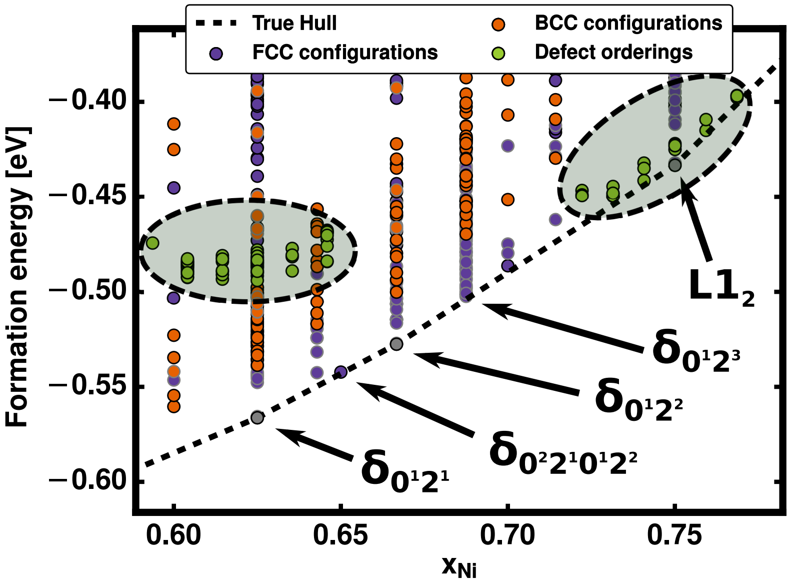

Figure 3.7: Close up of formation energies near δ and γ' compositions. Configurations that are combinations of L1_0 and L1_2 result in new groundstates that break the convex hull. Energies colored green correspond to orderings of $\delta_{0^1 2^1}$ and L1_2 with a dilute amount of antisite defects. Dilute defect energies in the $\delta_{0^1 2^1}$ and L1_2 orderings have been highlited.

and L1_2 are compared in fig. 3.5. L1_0 consists of alternating Ni and Al layers along the $\{001\}$ direction of FCC. L1_2 can be derived from L1_0 by replacing half the Al in the Al (001) layers of L1_0 by Ni in a checker board pattern.

The δ ordering at $x_{Ni} = 0.625$, which is the first ground state of the series of hybrid orderings (Figure 3.7), is made up of alternating layers of L1_2 and L1_0 along the $\{101\}$ direction as illustrated in fig. 3.8. Additional layered configurations were systematically enumerated by varying the number and order of L1_0 and L1_2 layers along the $\{101\}$ direction. Configurations with single L1_0 layers separated by one or more L1_2 layers were found to have formation energies that dip below the common tangent connecting δ at $x_{Ni} = 0.625$ and L1_2 at $x_{Ni} = 0.75$. Aluminum rich configurations having an excess of L1_0 layers in contrast were found to have high formation energies that are substantially above the common tangent between δ at $x_{Ni} = 0.625$ and B2 NiAl at x_{Ni}=0.5.

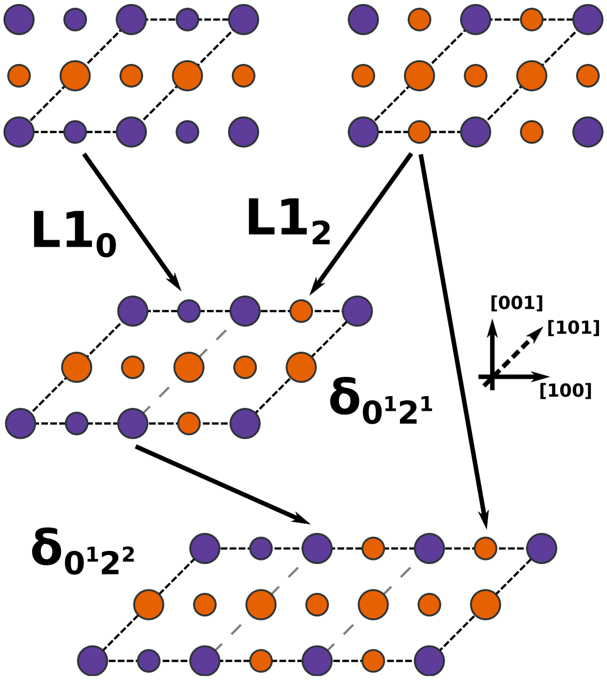

Figure 3.8: L1$_0$ (left) and L1$_2$ (right) orderings and their relation to the Ni$_5$Al$_3$ δ structure (bottom). Alternating layers of L1$_0$ and L1$_2$ unit cells along the [101] plane result in the $\delta_{0^12^1}$ and $\delta_{0^12^1}$ ordering.

Hybrid orderings are common in alloys and oxides [56, 23, 41, 57]. A naming convention has been established to label families of hybrid phases [56], which we adopt here. Since the first hybrid phase Ni$_5$Al$_3$ is referred to as δ, we use this label to refer to the whole family of hybrid orderings. Subscripts are then added to distinguish the various hybrid orderings based on their number of L1$_2$ and L1$_0$ subunits. A "0" indicates a L1$_0$ layer, while a "2" indicates a L1$_2$ ordering. Exponents on each subscript denote the number of each layer used to construct the full ordering. The unit cell of the groundstate at $x_{Ni} = \frac{2}{3}$, for example, is composed of a single L1$_0$ layer followed by two L1$_2$ layers (fig. 3.8). This groundstate is, therefore, labeled as $\delta_{0^12^2}$. The ground state at $x_{Ni} = 0.625$, Ni$_5$Al$_3$, consists of alternating layers of L1$_0$ and L1$_2$, such that its label would be $\delta_{0^12^1}$.

3.3.3 Navigating strain space

Many orderings on FCC and BCC in the Ni-Al binary are dynamically unstable and relax to a different parent crystal structure. [58] The strain order parameters described in section 3.2.2 can be used to quantify the distance of a relaxed structure to either FCC or BCC. We systematically analyze relaxation strains in this section. High symmetry points and lines in e_2-e_3 space will be referred to using the labelling outlined in fig. 3.3.

Pure Ni (γ) and L1$_2$ (γ') strain surface

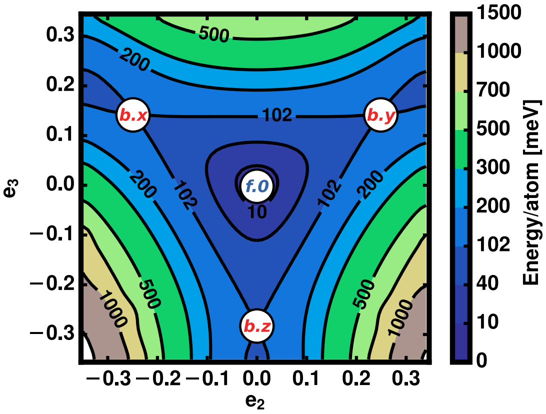

Figure 3.9: Strain energies relative to FCC Ni. Strain values corresponding to FCC are indicated with *f*, while values corresponding to BCC are shown with *b*. Any straight path connecting the origin to a marked location is a Bain path.

The simplest phase to explore in e_2-e_3 space is pure Ni (γ phase) as it lacks a symmetry breaking Ni-Al ordering. Wang et al [58] have already shown that if a pure element is stable as FCC at 0K, then the BCC form of that element must be unstable. The global energy minimum for Ni lies at the origin (fig. 3.9, located at *f.0*) when using FCC as a reference for strain. Three equivalent Bain paths connect FCC at the origin to three symmetrically equivalent BCC lattices (*b.z*, *b.y*, *b.x*). These equivalent BCC lattices appear as three saddle points (instabilities along the Bain path) on the energy surface.

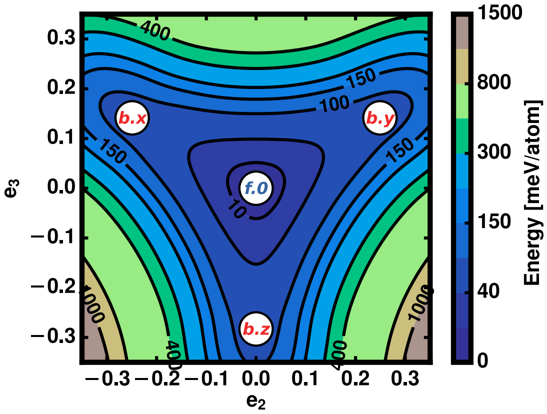

Figure 3.10: Strain energies relative to the $L1_2$ ordering.

Extending further along these Bain paths yields a local minimum, corresponding to a BCT structure, consistent with the findings of Wang et al [58].

The γ' phase, having $L1_2$ ordering, has FCC connectivity, and is the groundstate when $x_{Ni} = 0.75$. The global minimum for the strain energy plot of the γ' phase (fig. 3.10) using FCC as a reference again resides at the origin (*f.0*). The $L1_2$ ordering preserves the original FCC cubic point group symmetry, reflected in the threefold symmetry of the energy surface in e_2-e_3 space. The BCC variants (indicated by locations $b.z$, $b.y$, $b.x$) do not reside in a local minimum and are therefore unstable and will spontaneously relax back to FCC $L1_2$.

B2 (β) strain surface

The β phase has a B2 ordering on the BCC crystal structure. Figure 3.11a shows that its energy is at a global minimum at the origin in e_2-e_3 space ($b.0$) when B2 is used as the reference for strain. This structure also has cubic symmetry, which is once again reflected in the 3-fold symmetry in e_2-e_3 space. Straining B2 along any of the three Bain paths results in three equivalent FCC $L1_0$ orderings ($f.z$, $f.y$, $f.x$). The plot reveals that these three FCC variants do not coincide with any local minima and will spontaneously

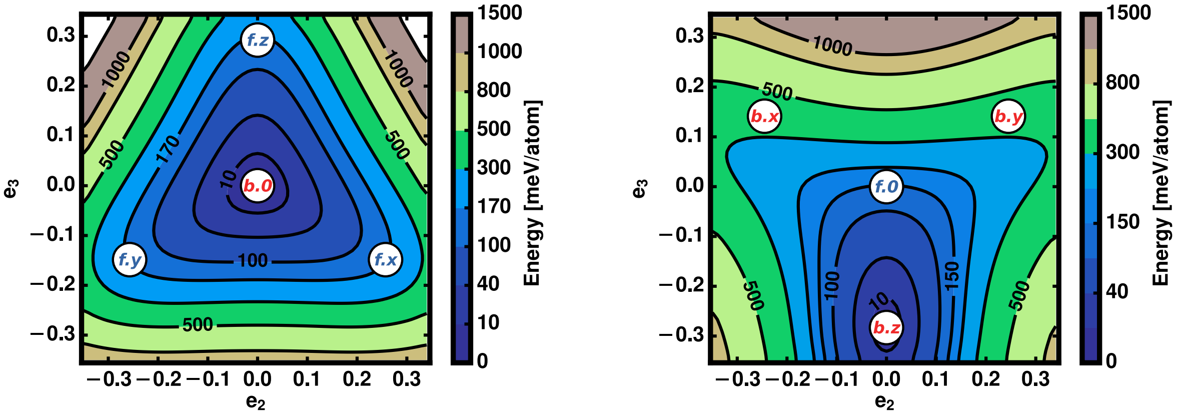

(a)

(b)

Figure 3.11: Strain energies relative to the B2 ordering (fig. 3.11a) and the $L1_0$ ordering (fig. 3.11a). Non B2 based BCC orderings are mechanically unstable.

collapse to the BCC B2 ordering. NiAl having $L1_0$ ordering is therefore mechanically unstable.

Interesting properties are revealed about Ni-Al orderings on BCC when using FCC $L1_0$ as a reference for strain. Since the Ni-Al ordering in $L1_0$ (fig. 3.5a) has tetragonal symmetry, the three-fold symmetry in e_2-e_3 space is broken (fig. 3.11b). One Bain path connects $L1_0$ (*f.0*) to the B2 ordering on BCC ($b.z$), and the two other Bain paths connect symmetrically equivalent orderings on BCC ($b.x$, $b.y$) consisting of alternating Ni and Al layers along the $\{110\}$ directions, as shown in fig. 3.12. As is clear in fig. 3.11b, not only is $L1_0$ at the origin unstable (*f.0*), the two non-B2 Ni-Al orderings (fig. 3.12, residing on $b.x$ and $b.y$) are also unstable. Figure 3.11b shows that alternating layers of Ni and Al along $\{110\}$ in BCC will spontaneously collapse to a B2 ordering, which is also BCC. This is an example where an instability of an ordering on BCC causes a structural relaxation to another ordering on BCC (fig. 3.12).

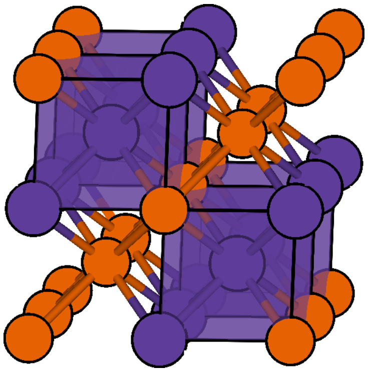

Figure 3.12: Unstable ordering on BCC. Alternating Ni and Al layers along {110} directions will spontaneously relax into the favorable B2 ordering. The ordering shown here corresponds to strain locations *f.y* and *f.x* in fig. 3.11b.

$\delta_{0^1 2^1}$ strain surface

Strain energy surfaces in e_2-e_3 space for δ Ni_5Al_3 (i.e. $\delta_{0^1 2^1}$) are shown in fig. 3.13. Figure 3.13a shows the strain energy surface when using FCC as a reference for strain. As is clear in fig. 3.13a, the minimum of the energy surface does not reside at the origin corresponding to perfect FCC (*f.0*), but is shifted due to the orthorhombic symmetry of the Ni-Al ordering of $\delta_{0^1 2^1}$. The three Bain distortions that originate from FCC are therefore also no longer symmetrically equivalent. While the three BCC orderings that can be generated by application of Bain distortions to $\delta_{0^1 2^1}$ are all dynamically unstable (fig. 3.13a), one of the BCC variants (*b.z*) clearly resides in a more shallow energy valley than the two others. Interestingly, the energies of the $\delta_{0^1 2^1}$-ordering of ideal FCC and of ideal BCC in the lowest energy valley are very close to each other, and have a low value of roughly 30meV/atom above the global minimum.

It is also revealing to consider the strain energy surface using the BCC variant in the lowest energy valley (*b.z* of fig. 3.13a) as a reference, shown as *b.0* in fig. 3.13b. While the minimum of the strain energy surface of fig. 3.13b resides close to the FCC variant corresponding to $\delta_{0^1 2^1}$ (*f.z*), the energy surface is nevertheless very shallow even for the other FCC variants (*f.x*, *f.y*) that can be reached by application of Bain distortions to

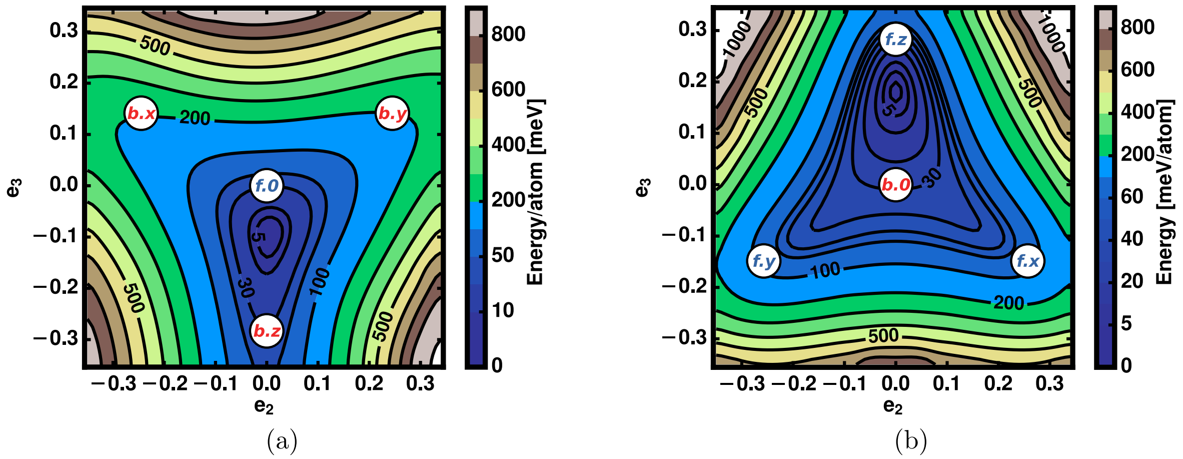

Figure 3.13: Strain energy values for the $\delta_{0^1 2^1}$ ordering on FCC (fig. 3.13b) and BCC (fig. 3.13b). Unlike other groundstates, the global minimum for this structure is neither FCC (*f.0*) or BCC (*b.0*).

the BCC variant at the origin of fig. 3.13b. Furthermore, it illustrates that there are two orderings on FCC at $x_{Ni} = 0.625$ (i.e. *f.x* and *f.y* in fig. 3.13b) that are dynamically unstable and that, instead of collapsing to a BCC structure along a Bain path, will relax to another ordering on FCC (i.e. $\delta_{0^1 2^1}$, located at *f.z*). The shallow strain energy surface and its strong deviation from parabolic behavior, along with dynamical instabilities not only of BCC, but also of FCC orderings, indicates a strong degree of anharmonicity at compositions around $x_{Ni} = 0.625$. The strain energy surfaces of fig. 3.13a suggest that the alloy exhibits ambiguity about its preference for either FCC or BCC. Since the minimum of the energy surface lies closer to FCC than to BCC, the $\delta_{0^1 2^1}$ phase will resemble FCC more than BCC at low temperatures. At elevated temperature, though, anharmonicity may shift the lattice dimensions more towards BCC. We revisit this point when discussing phase stability at finite temperature.

3.3.4 Relaxation of enumerated structures

The previous section showed examples where a particular ordering on FCC will spontaneously relax along a Bain path to BCC and vice versa. Quantifying the amount of strain experienced by a particular ordering during relaxation does not require a full mapping of the energy surface in e_2-e_3 space as was done in the previous section. Only the minimum energy strains relative to the ideal reference parent crystal are needed, which are obtained by comparing the enumerated configuration before and after relaxation. For example, a Ni-Al arrangement on FCC having $L1_0$ ordering will relax into the BCC B2 ordering. The resulting relaxation strain coincides with the global minimum of fig. 3.11b. Figure 3.14 shows the relaxation strains of orderings enumerated over FCC and over the sublattices of BCC based B2 relative to their ideal starting parent structure. Each relaxation has been color coded to indicate the prototype structure (FCC, BCC or HCP) it most closely maps onto as determined using the metrics outlined in section 3.2.2.

Figure 3.14 shows that structures with small relaxation strains mapped onto their original parent crystal structure, while those with very large relaxation strains mapped onto another parent crystal structure. Interestingly, without accounting for shear strains, a sharp transition between FCC and BCC is evident in fig. 3.14. Figure 3.14a shows that almost every FCC ordering with a relaxation strain beyond a e_2-e_3 radius of about 1.5 has transformed into a structure that resembles BCC more than FCC (see section 3.2.2). Similar behavior is evident in fig. 3.14b, which shows that BCC orderings with relaxation strains in e_2-e_3 space beyond a radius of about 1.2 more closely map onto FCC than BCC. The clustering of points in this space also reveals that many of the relaxations followed a Bain path. Especially the large relaxation strains tend to fall along the Bain path, resulting in clearly visible arms extending from the origin.

Whether or not a configuration on a particular crystal structure is mechanically un-

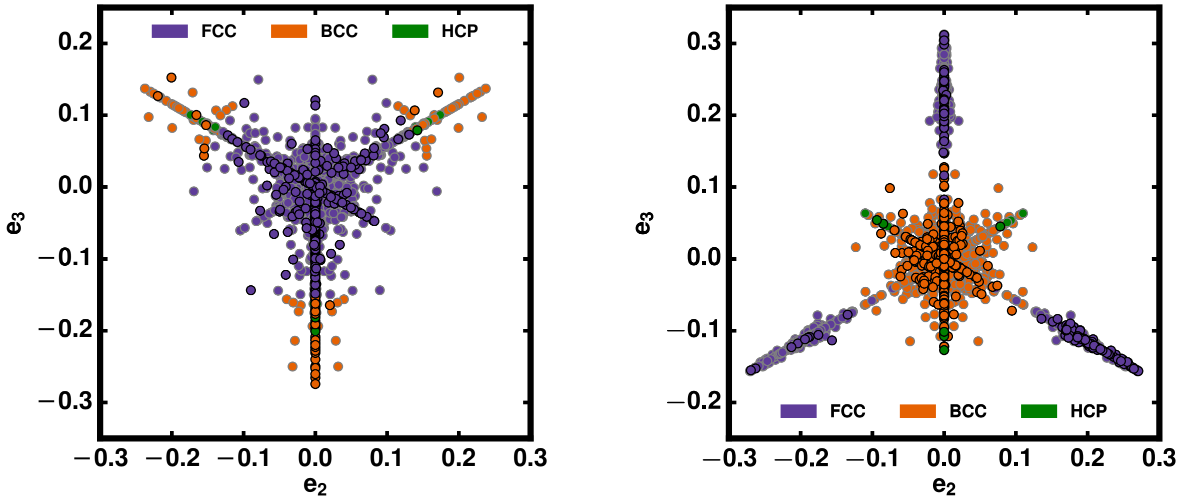

(a) (b)

Figure 3.14: For every enumerated configuration over FCC (fig. 3.14a) or B2 (fig. 3.14b) the strain of the relaxed structures is calculated relative to the structure used as input to DFT. This strain is then projected onto e_2-e_3 space. Orderings that undergo small e_2 and e_3 distortions appear closest to the origin. Combining the strain metrics with the Hungarian algorithm the relaxed structures are binned into FCC, BCC or HCP, indicated by the color of each point.

stable is strongly correlated with its concentration. The fraction of enumerated orderings that are unstable in different composition intervals is shown in the histograms and energy plots of fig. 3.15. Figures 3.15a and 3.15c plot relaxation histograms and formation energies for orderings that were enumerated over FCC, while figs. 3.15b and 3.15d only show results for orderings enumerated over B2.

The orderings enumerated on the FCC lattice are consistently stable at both high and low Ni compositions. At compositions close to x_{Ni}=0.5, however, many configurations relax from FCC into a B2 derived ordering. The most pronounced example already discussed is the relaxation of $L1_0$ ordering on FCC to B2 along a Bain path (fig. 3.11b). This configuration is the point with the lowest energy at a composition of 0.5 Ni. As the histogram of fig. 3.15a clearly shows, configurations on FCC with compositions close to that of β are increasingly likely to have an ordering that is unstable with respect to a

Bain strain to BCC.

The configurations enumerated from the B2 unit cell also show an increase of instabilities within a narrow composition range. At compositions close to x_{Ni}=0.5, almost all of the lower energy structures maintain the original BCC parent lattice, but as the composition passes x_{Ni}=0.625 (i.e. the composition of the $\delta_{0^1 2^1}$), the majority of the enumerated B2 orderings (with mostly Ni antisites) collapse into FCC. The three groundstates in this composition range are either the FCC based γ and γ' phases, or the family of δ phases, which are more closely related to FCC than BCC. It is likely that many of the B2 orderings above $x_{Ni} = 0.625$ that maintain BCC connectivity after relaxation actually reside at a saddle point due to a high symmetry Ni-Al ordering. These phases would also be dynamically unstable, however, establishing this would require a phonon analysis for each structure which is beyond the scope of this study.

3.3.5 Cluster Expansion and finite temperature

The fully relaxed formation energies of different orderings on FCC and over the sublattices of B2 were used to parameterize cluster expansions. A cluster expansion allows us to rapidly extrapolate the DFT energies calculated for a small set of orderings to an arbitrary configuration in substantially larger supercells used in Monte Carlo simulations to calculate finite temperature thermodynamic averages. Two separate cluster expansions were constructed to describe the NiAl binary for $0.2 < x_{Ni} \leq 1$: one for B2 based orderings on BCC around $x_{Ni} = 0.5$, and another for Ni rich orderings on FCC. The sets of training data used to construct a cluster expansion should consist exclusively of orderings that are stable on their respective parent crystal structure. In fitting the cluster expansions, we therefore eliminated all configurations that relaxed to a different parent crystal structure.

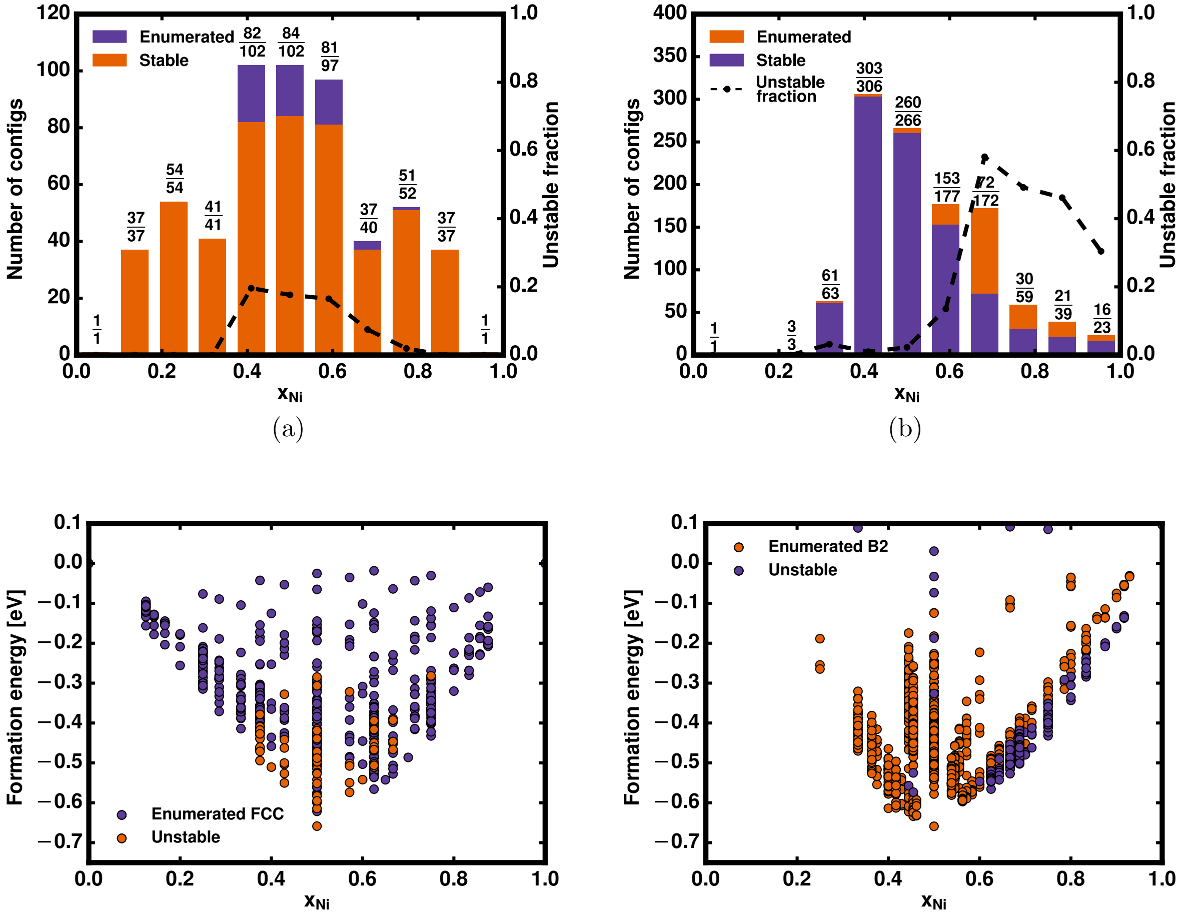

(a) (b)

(c) (d)

Figure 3.15: Enumerated configurations over FCC (figs. 3.15a and 3.15c) and B2 (figs. 3.15b and 3.15d) comparing the amount of orderings that are stable.

The expansion for FCC contains 26 cluster basis functions and was fit to the energies of 539 orderings that mapped to FCC after relaxations. The expansion has a root mean square (rms) error of 0.015 meV/atom relative to the formation energies used in the fit and a cross validation (cv) score of 0.016 meV/atom. The FCC cluster expansion was weighted to more accurately predict formation energies of configurations having Ni rich compositions. The rms relative to DFT formation energies of configurations with $0.73 < x_{Ni} \leq 1$ is therefore lower having a value of 0.010 meV/atom.

The cluster expansion for B2 consists of 68 clusters and was fit to the energies of 892 enumerated orderings. The rms error for this fit is 0.012 meV/atom with a cv score of 0.028 meV/atom. All of the configurations for this cluster expansion were enumerated from a B2 unit cell, with different occupants allowed on the two sublattices: one sublattice accommodates Ni and vacancies, while the other accommodates Al and Ni. The use of a coupled cluster expansion [59, 60] to describe disorder over two separate sublattices in β (B2-NiAl) was motivated by the early experimental observations of Bradley and Taylor [27] and more recent first-principles study [15, 61]. These studies showed that B2-NiAl accommodates an excess of Ni with Ni anti-site defects on the Al sublattice and an excess of Al with vacancies on the Ni sublattice. While other anti-site defects also form, they are entropically stabilized and have exceedingly low compositions such that they do not affect bulk thermodynamic properties [15, 61]. A cluster expansion that describes disorder relative to the B2 orderings on BCC as opposed to a general cluster expansion for the BCC lattice is also motivated by the strain energy surface of fig. 3.11b. As was pointed out in section 3.3.3, the B2 ordering of NiAl is especially stable with other simple orderings on BCC, such as the one depicted in fig. 3.12, being dynamically unstable and relaxing directly to B2.

The cluster expansions constructed to predict formation energies of orderings on FCC and B2 were subjected to grand canonical Monte Carlo simulations. In the grand canonical ensemble, the chemical potentials and temperature are controlled variables, while the conjugate variables, composition and grand canonical energy, are ensemble averages that can be approximated with Monte Carlo simulations. Free energies were obtained by integrating calculated relations between composition and chemical potential and between grand canonical energy and temperature [15, 62]. Figure 3.16 shows calculated free energies as a function of composition at 705°C. Included in fig. 3.16 are the DFT formation energies of Al_3Ni, $\delta_{0^1 2^1}$ and $\delta_{0^1 2^2}$, which are treated as line compounds. As was shown in section 3.3.1, antisite defect formation is substantially more costly in $\delta_{0^1 2^1}$

than in B2-NiAl and γ'. The family of δ phases are therefore more resistant to antisite defects to realize off-stoichiometric compositions even at elevated temperatures and are approximated as line compounds.

Figure 3.17 shows a first-principles phase diagram for the Ni-Al binary obtained by minimizing calculated free energies through a common tangent construction at various temperatures. The liquid phase was not explicitly considered in the construction of the phase diagram, which should form in the yellow region of fig. 3.17 according to experimental phase diagrams.[14] The orange regions in fig. 3.17 correspond to B2-derived single phase regions. The β phase, which has B2 ordering but no long-range vacancy ordering over the Ni-sublattice is stable around $x_{Ni} = 0.5$. The β' phase, having Ni_3Al_4 stoichiometry is stable at low temperature, but is predicted to decompose through a peritectoid reaction around 820°C. This phase, which as described in section 3.3.1 is derived from B2 and exhibits long-range vacancy ordering on the Ni sublattice, is only stable in a narrow composition range. The β'' phase, which is also a vacancy ordered derivative of B2, is stable up to high temperatures and in a wide composition range. The purple single phase regions in fig. 3.17 correspond to FCC derived phases. The calculated phase diagram shows that the γ solid solution can tolerate a high Al concentration. The γ' phase, which has $L1_2$ ordering, is also stable in a wide concentration range with off-stoichiometry achieved with antisite defects. The two δ phases that reside on the convex hull, $\delta_{0^1 2^1}$ and $\delta_{0^1 2^2}$, appear as line compounds and, surprisingly, are predicted to remain stable up to high temperatures. The Al_3Ni phase was similarly treated as a line compound and also appears strictly at its stoichiometric composition in the phase diagram.

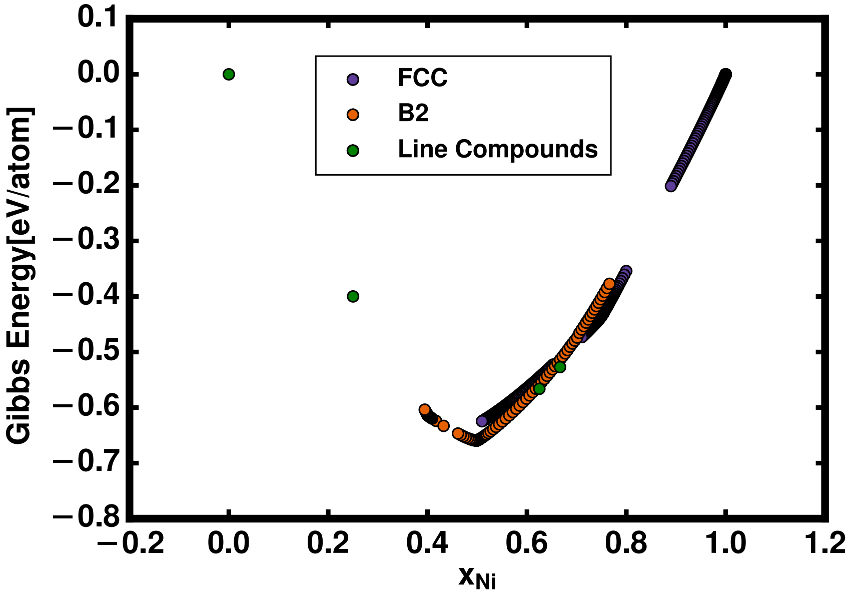

Figure 3.16: Calculated Gibbs free energies for both the FCC (purple) and B2 (orange) cluster expansions at 705°C. Phases that are being approximated as a line compound (such as δ orderings) appear as a single green point.

3.4 Discussion

Our first-principles study of phase stability in the Ni-Al binary, both at zero Kelvin and at finite temperature, not only confirms the stability of the well characterized β and γ' intermetallic compounds, but also predicts a variety of ground states derived either from β for Al rich compositions, or from γ' for Ni rich compositions. The β phase, having B2-NiAl ordering, is unique among intermetallic compounds in that it can accommodate very high concentrations of vacancies. While vacancy concentrations in intermetallic compounds typically do not exceed [63, 64] 10^{-6} they can reach a fraction as high as 0.3 on the Ni sublattice of the β phase. Interactions among vacancies become important at such high concentrations, which in the β phase lead to two vacancy ordered derivative phases of β. At Ni rich compositions, a hierarchy of hybrid phases, consisting of layers of $L1_0$ and $L1_2$ ordering having different ratios are predicted as ground states or near ground

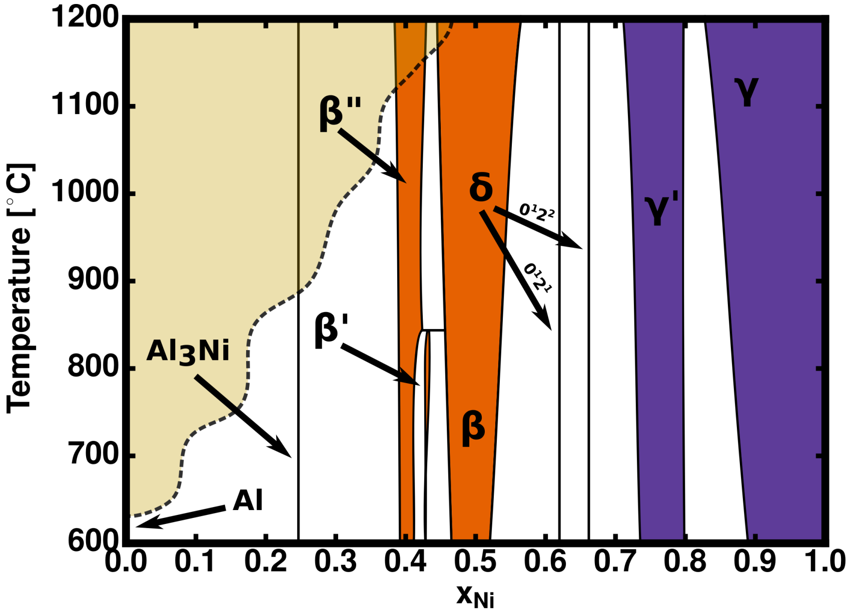

Figure 3.17: Gibbs energy minimization for the binary system.

states between $x_{Ni} = 0.625$ and 0.75. The energy of these phases as a function of strain order parameters that describe all symmetrically equivalent Bain paths are very shallow. These strain energy surfaces show that the hybrid phases are stable in a composition range where the Ni-Al chemistry exhibits ambivalence about its preference for either an FCC or a BCC parent crystal structure. It is in this composition range where many orderings are unstable as either FCC or BCC.

The calculated phase diagram of fig. 3.17 shows that a cluster expansion parameterized with several hundred DFT-PBE formation energies predicts a large Al solubility for γ and a wide concentration range around the stoichiometric L1$_2$ composition of $x_{Ni} = 0.75$ in which γ' is stable. The two-phase region separating γ and γ' is quite narrow, similar to what has been predicted with embedded atom force fields [65] and previous cluster expansions [66]. The phase diagram of fig. 3.17 also resolves the finite temperature phase boundaries between the family of vacancy rich B2 derived phases. The β phase, having B2-NiAl ordering, accommodates excess Ni as antisite defects on the Al sublattice, but relies on vacancies on the Ni sublattice to achieve Al rich compositions. In the β phase, the vacancies are disordered, however, above a threshold vacancy concentration, the vacancies prefer to order forming distinct phases having ideal stoichiometries of Ni_3Al_4 and Ni_2Al_3. Since these phases have a group/subgroup symmetry relationship with β as a result of vacancy ordering, we have labeled them as β' and β'' respectively. The β' phase, characterized by a three dimensional arrangement of vacancies (fig. 3.6c), is considered only in specialized phase diagrams that account for it specifically, such as the one by Ellener and Predel[55]. The β''-Ni_2Al_3 compound appears in most phase diagrams, but is generally not recognized as a derivative structure of B2 NiAl. The calculated phase diagram shows that the vacancy ordering of β''-Ni_2Al_3 is especially stable persisting to temperatures above 1200°C, in contrast to the vacancy ordering of β'-Ni_3Al_4, which disappears through a peritectoid reaction to β'' and β at 840°C. In both β' and β'', the vacancies favor positioning themselves diagonally from each other (fig. 3.6c and fig. 3.6b). The common underlying atomic ordering of β, β' and β'' allowed us to calculate their free energies with a single cluster expansion using Monte Carlo simulations.

Two of the δ phases are predicted to be stable in the calculated phase diagram, and because they were modeled as line compounds, they appear as stoichiometric phases. Though some experimentally based diagrams show significant solubility for a Ni_5Al_3 phase (with $\delta_{0^1 2^1}$ ordering), others appear to also indicate line compound behavior, or even omit the phase from consideration completely [67, 14]. The high formation energies of antisite defects in $\delta_{0^1 2^1}$ (Ni_5Al_3) suggest that this phase will only be able to accommodate small amounts of configurational entropy, even at high temperatures, providing the basis to model it as a line compound.

An interesting result from the enumerated configurations is the discovery of the many possible low energy δ orderings that appear between $x_{Ni} = 0.625$ and 0.75 (fig. 3.7). The construction of these orderings by combining $L1_0$ and $L1_2$ layers results in an arbitrary

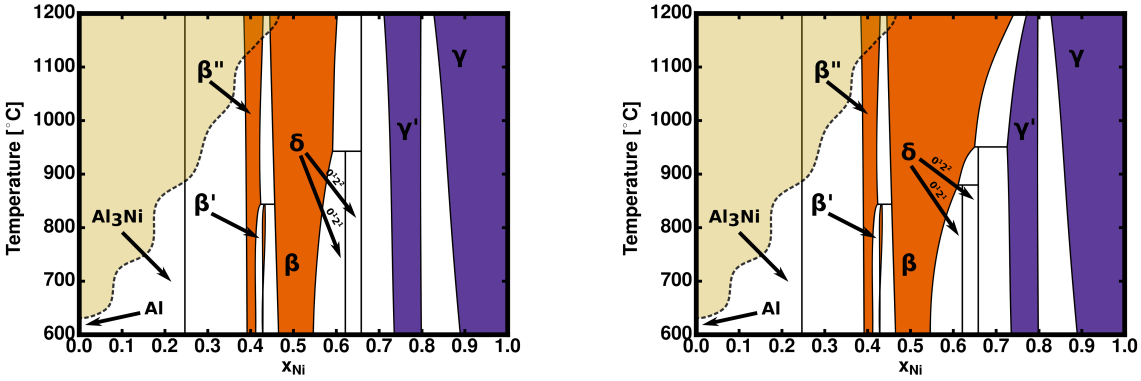

(a)

(b)

Figure 3.18: Phase diagrams such as fig. 3.17, with different amounts of artificial vibrational energy contribution added to the β free energies. The vibrational contributions increase with Ni composition and temperature, stabilizing the β (BCC) phase over δ (FCC) orderings.

number of configurations that are either groundstates or lie within a couple of meV from the global hull. The existence of these orderings as low energy configurations suggests an alternative mechanism with which a range of compositions around $x_{Ni} = 0.625$ are stabilized that does not require energetically costly antisite defects. Instead of creating antisite defects, an overarching δ phase can instead accommodate an excess of Ni by increasing the ratio of $L1_2$ to $L1_0$ layers, thereby locally preserving their ordering. The high degree of degeneracy among the many possible δ orderings indicate that a range of compositions are likely to be observed experimentally.

Experimental phase diagrams [14] show very high Ni solubility in β, with one assessment reporting a solubility as high as $x_{Ni} \approx 0.65$ at 1200° [14]. Yet, as discussed in 3.3.4, a majority of the B2 enumerated configurations (figure 15 b) around $x_{Ni} = 0.65$ are predicted to be dynamically unstable and collapse to an FCC ordering. These zero Kelvin predictions, however, are not necessarily inconsistent with the high temperature experimental observations of a Ni-rich B2 phase. Many high temperature phases, are in fact predicted to be dynamically unstable with DFT at zero Kelvin. Nevertheless, Monte Carlo simulations applied to anharmonic lattice dynamical Hamiltonians have shown that dynamically unstable phases can become stable at high temperature as a result of anharmonic vibrational excitations. TiH_2 and ZrH_2, for example, exhibit a cubic to tetragonal second order structural transition upon cooling [68, 69]. The high temperature cubic phases of these hydrides are predicted to be dynamically unstable at zero Kelvin with DFT but become stable at high temperature due to large anharmonic vibrational excitations [70, 39, 68]. Similar phenomena have been predicted for perovskites [71, 72, 73, 74].

A comparison of the strain-energy surfaces of the different groundstates in the Ni-Al binary reveals a strong degree of anharmonicity at compositions where Ni-rich β and the family of δ phases are stable. The strain-energy surfaces of pure Ni, $L1_2$ and stoichiometric B2-NiAl (figs. 3.9, 3.10 and 3.11a) increase rapidly as these crystals are strained. The quasi-harmonic approximation should therefore be sufficiently accurate to account for vibrational excitations in these elastically stiff phases, as was done in past studies [75, 76].The shape of the strain-energy surface of $\delta_{0^12^1}$, in contrast, is highly anisotropic and shallow (fig. 3.13b). While the energy minimum of $\delta_{0^12^1}$ in e_2-e_3 space is closer to FCC than to BCC, the constant energy contours at energies that are only slightly above the energy minimum in fig. 3.13b more symmetrically surround ideal BCC than FCC. In fact, the constant energy contours in fig. 3.13b exhibit shapes very similar to the energy surfaces of TiH_2 and ZrH_2 in e_2-e_3 space, compounds that are tetragonal at low temperature, but transform to cubic symmetry at elevated temperature through a second order structural transition [70, 39, 68]. This suggests that entropic forces arising from anharmonic vibrational excitations are likely to shift the equilibrium lattice vectors of $\delta_{0^12^1}$ away from the energy well close to FCC at low temperature more towards BCC symmetry at elevated temperature. At low temperatures, the system is limited to sampling states close to the global minimum, corresponding to the low symmetry martensite phase. As the temperature is raised, thermal excitations allow the system to sample higher energy states. The anharmonic potential results in an uneven sampling of these high energy states, which shifts the effective symmetry of the austenite phase towards BCC.

The above considerations about $\delta_{0^12^1}$ suggest that the BCC symmetry of the Ni-rich β phase is entropically stabilized at high temperature due to large anharmonic vibrational excitations and becomes dynamically unstable at low temperature. This conjecture is consistent with the martensitic transformations exhibited by Ni-rich β upon quenching [32, 30, 29, 77, 78, 79, 80, 81]. It also suggests that contributions to the free energy from vibrational excitations are especially important in the free energy description of Ni-rich β, more so than for stoichiometric β NiAl and the other compounds of the Ni-Al binary. Anharmonic vibrational excitations in Ni-rich β are also likely coupled to the local degree of ordering. Describing this coupling will require effective Hamiltonians that are simultaneous functions of displacement degrees of freedom [39, 68] and configurational degrees of freedom [47]. Monte Carlo simulations, similar to what was done with EAM potentials [33], will then capture the interplay between anharmonic vibrational excitations, dynamical instabilities and variations in ordering as a function of temperature and reveal the true nature of the martensitic phase transformations that occur upon quenching Ni-rich β. A coupled effective Hamiltonian that combines displacement and configurational degrees of freedom would allow Monte Carlo simulations to predict the onset of the martensitic transformation as a function of temperature and composition. Unfortunately, the construction of such a Hamiltonian currently presents a significant challenge, both for the amount of DFT calculations required as training data, as well as the vast number of resulting basis functions that must be considered in the fit.

While vibrational excitations have not been explicitly addressed in this study, we can speculate as to how their incorporation will qualitatively modify the predicted phase diagram. The importance of anharmonic vibrational excitations in Ni-rich β as compared to that in stoichiometric β (i.e. B2 NiAl), $L1_2$ and the family of δ phases, where vibrations are more harmonic in nature, suggests that Ni-rich β will have more vibrational entropy than the other compounds in the Ni-Al binary. The free energy of Ni-rich β should therefore decrease more than that of the other phases competing for stability upon inclusion of vibrational contributions. Such a lowering of the free energy of Ni-rich β improves the agreement of the calculated phase diagram with experiment. A significant discrepancy between the calculated phase diagram and those published in the literature is the width of the two-phase region separating β and γ'. Experiments show a large Ni solubility in the β phase and a relatively narrow γ' single phase region. The calculated phase diagram, in contrast, predicts a lower Ni solubility in β and a wide stability interval for γ', with the δ phases remaining stable above 1200°C. A lowering of the free energy of Ni-rich β at high temperature will widen the single phase region of the β phase by extending its Ni solubility to higher concentrations, while simultaneously narrowing the composition range of the γ' single phase region. Furthermore, an increased stability of Ni-rich β will decrease the maximum temperature at which the δ phases exist, which is significantly overpredicted in the calculated phase diagram.

We can explore how an increase in the stability of Ni-rich β affects the calculated phase diagram by parametrically modifying the free energy of the β phase. This is shown in fig. 3.18. The calculated free energy of the β phase above x_{Ni}=0.5 was lowered by subtracting off a term linear in composition and temperature (i.e. the correction term is zero at $x_{Ni} = 0.5$ but grows linearly with excess Ni concentration and temperature). Figure 3.18 shows that a further stabilization of Ni-rich β relative to the other competing phases increases the Ni-solubility of β, reduces the peritectoid transformation temperatures of the δ phases and decreases the width of the γ' phase. The effect of a doubling of the stabilization is evident upon comparison of fig. 3.18a and fig. 3.18b. The phase diagram of fig. 3.18b closely resembles the reported experimental phase diagrams. The parametric analysis of fig. 3.18 demonstrates that the additional lowering of the free energy of Ni-rich β relative to the other competing phases yields a phase diagram that is more consistent with experiment than that calculated by considering only configurational degrees of freedom. The strain energy surfaces of section 3.3.3 suggest that such a lowering of free energy in Ni-rich β should occur due to anharmonic vibrational excitations that are not as important in the other phases.

3.5 Conclusion

We have conducted a first principles study of phase stability in the Ni-Al binary, both at zero Kelvin and at finite temperature. Our results not only confirm the stability of the well charaterized β and γ' intermetallic compounds, but also predict a new family of groundstates derived from β and γ'. A comparison between the calculated phase diagram to experimental data [67, 14] shows good agreement with several important discrepancies. The discrepancies considered in conjunction with an analysis of the energy as a function of strain point to the likely importance of anharmonic vibrational excitations in stabilizing the Ni rich β phase at high temperature, which is susceptible to martensitic transformation upon quenching.

3.6 Acknowledgements

This research was supported by the National Science Foundation (DMR-1105672). Computational resource support was provided by the Center for Scientific Computing at the CNSI and MRL: an NSF MRSEC (DMR-1121053) and NSF CNS-0960316. Crystal structure images were generated using VESTA [82], and plots were generated using

matplotlib [83].

Chapter 4

Recursively extending to multicomponent systems[1]

4.1 Introduction

First-principles predictions of high temperature alloy properties will become more important as complex alloys are increasingly being considered for structural applications in extreme environments. Multi-principle element (MPE) alloys, also often referred to as high entropy alloys, promise to overcome many elevated temperature structural materials challenges[84, 85, 86, 87, 88, 89]. The extreme environments in which such alloys are to operate, however, make in depth experimental investigations difficult and costly. Complex MPE alloys also pose significant challenges to first-principles approaches as they reside in high dimensional composition spaces.

One way to model alloys from first-principles, especially at high temperature where disorder plays an important role, is with statistical mechanics approaches that rely on cluster expansions [47, 49]. A cluster expansion is an effective Hamiltonian that is capable of representing the dependence of the crystal energy on the degree of short and long-range order among alloying elements. The past years have seen the development of new approaches with which to parameterize the interaction coefficients of cluster expansions to first-principles energies[90, 91, 92, 93, 94, 95]. A cluster expansion that can accurately extrapolate expensive first-principles energies to any ordering on a given parent crystal structure can be used within Monte Carlo simulations to predict high temperature thermodynamic properties.

---

[1] The contents of this chapter have been substantially reproduced from J. G. Goiri and A. Van der Ven, *Recursive alloy Hamiltonian construction and its application to the Ni-Al-Cr system*, *Acta Materialia* **159** (Oct., 2018) 257–265

Parametrizing cluster expansions in high order alloy systems remains a challenge due to the large number of interactions that must be accounted for. This has limited the number of elements used in ab initio statistical mechanics studies of high temperature alloy properties. Here we introduce a recursive approach for constructing cluster expansions in high dimensional composition spaces, where the lower order interaction coefficients are used as informative priors for the estimation of higher order interaction coefficients. As an example, we study the Ni-Al-Cr system, and construct an effective Hamiltonian recursively by building on the interaction coefficients from the binary Ni-Al and Ni-Cr systems. The resulting cluster expansion is then used in grand canonical Monte Carlo to calculate high temperature phase diagrams and explore the sublattice preference of Cr as an alloying element.

The high temperature and mechanical properties of nickel based superalloys makes them ideal structural materials for turbine blades in aircrafts and power generation[7, 17]. Most superalloys are primarily Ni-Al based, but usually include additional elements such as Cr, Co, W, Ta or Re, which are added to improve mechanical properties and oxidation resistance[7]. The Ni-Al-Cr ternary is especially important, as the combination of Al and Cr within the Ni-rich γ and γ' phases can lead to favorable oxide scale formation [96, 97, 11]. While the Ni-Al and Ni-Cr binaries have received much attention theoretically

[98, 75, 53, 1, 99], far less has been explored about the ternary Ni-Al-Cr alloy with first-principles approaches. In this contribution, we focus in particular on the Ni-rich corner of the Ni-Al-Cr phase diagram in view of its importance for high temperature structural applications.

4.2 Methods

4.2.1 Cluster Expansion Method

A cluster expansion describes the energy of a multicomponent crystal as a function of the arrangement of the different atomic species on a parent crystal structure [49, 48, 47, 100]. This is achieved by assigning occupation variables to each crystal site. Here we use a lattice gas type cluster expansion [101, 64]. A ternary A-B-C alloy then requires two occupation variables, for example p_i^A and p_i^B, which are 0 or 1 depending on the occupant of site i. When the site is occupied by A, $p_i^A = 1$ and $p_i^B = 0$; when the occupant is B, $p_i^A = 0$ and $p_i^B = 1$; otherwise $p_i^A = p_i^B = 0$, indicating that C occupies the site. The two occupation variables for a particular site are combined into a site vector $\vec{p}_i = \{p_i^A, p_i^B\}$. The occupation of a crystal with N sites is now fully determined by $\vec{p} = \{\vec{p}_1, \vec{p}_2, \ldots, \vec{p}_N\}$.

The energy of the crystal depends on the occupation vector $\vec{p}$, and can be expressed as [47, 48, 49, 101]

$$E_f(\vec{p}) = \sum_{\alpha} \sum_{\pi} V_{\alpha}^{\pi} \phi_{\alpha}^{\pi}(\vec{p}) \tag{4.1}$$

where the cluster functions ϕ_{α}^{π} are defined as

$$\phi_{\alpha}^{\pi}(\vec{p}) = \prod_{i \in \alpha} p_i^{\pi(i)} \tag{4.2}$$

The variable α represents a collection of crystal sites, such as point, pair, triplet, etc.

clusters. The cluster function is simultaneously defined by π, which specifies unique combinations of the occupation variables p_i^A and p_i^B for each site i of the cluster α. For example, there are four distinct basis functions associated with a nearest neighbor pair cluster α in FCC: $p_i^A p_j^A$, $p_i^A p_j^B$, $p_i^B p_j^A$ and $p_i^B p_j^B$, where i and j are the two crystal sites of the pair cluster. Each of these cluster functions will evaluate differently, depending on the occupants of i and j. The coefficients V_α^π from eq. (4.1) are the effective cluster interactions (ECI), and are to be determined with regression techniques using first-principles density functional theory (DFT) calculations as training data.

The symmetry of the crystal relates many of the interaction coefficients V_α^π to each other: any basis function ϕ_α^π related to another basis function $\phi_{\alpha'}^{\pi'}$ by a symmetry operation of the crystal will have the same ECI, i.e. $V_\alpha^\pi = V_{\alpha'}^{\pi'}$. For example, a nearest neighbor cluster $\alpha = \{i, j\}$ in FCC has four basis functions, however, symmetry reduces the number of independent ECI for that cluster to three: one accompanying $p_i^A p_j^A$, another multiplying $p_i^B p_j^B$, and a third one multiplying both $p_i^A p_j^B$ and $p_i^B p_j^A$. Additional symmetry of the FCC crystal relates these three independent ECI to those of all other nearest neighbor pair clusters in the crystal. Equivalent cluster functions ϕ_α^π can be grouped into orbits Ω_α^π using the symmetry of the crystal. The energy of the crystal can then be rewritten according to

$$E_f(\vec{p}) = \sum_\alpha \sum_\pi V_\alpha^\pi \sum_{\alpha', \pi' \in \Omega_\alpha^\pi} \phi_{\alpha'}^{\pi'}(\vec{p}) \tag{4.3}$$

where the outer sums extend over symmetrically distinct cluster function prototypes, labeled by α and π, and the inner sums extend over all symmetrically equivalent cluster functions belonging to the same orbit Ω_α^π.

The energy of the crystal, $E_f(\vec{p})$, can be normalized by the number of primitive unit cells N to yield

$$e\left(\vec{p}\right)=\sum_{\alpha,\pi}V_{\alpha}^{\pi}m_{\alpha}^{\pi}\xi_{\alpha}^{\pi}(\vec{p}) \tag{4.4}$$

where

$$\xi_{\alpha}^{\pi}(\vec{p})=\frac{1}{m_{\alpha}^{\pi}N}\sum_{\alpha'\pi'\in\Omega_{\alpha}^{\pi}}\phi_{\alpha'}^{\pi}(\vec{p}) \tag{4.5}$$

are correlation functions and correspond to the average value of a cluster function in a particular configuration $\vec{p}$. The m_{α}^{π} are equal to the number of equivalent cluster basis functions per primitive unit cell.

The sum in eq. (4.1) extends over all clusters α within the crystal. In practice, the cluster expansion is truncated. One approach to determining values for the ECI of a truncated cluster expansion is with a regression method that relies on an inversion of eq. (4.4). This requires that a large number of energies for symmetrically distinct orderings, $\vec{p}$, are calculated from first-principles (e.g. with DFT or one of its extensions). Each $\vec{p}$ will have a distinct set of correlations, $\xi_{\alpha}^{\pi}\left(\vec{p}\right)$, one for each cluster basis function that remains in the truncated cluster expansion. The calculated energies, $e(\vec{p})$, can be collected in a column vector $\vec{y}$ while the set of correlations, $\xi_{\alpha}^{\pi}\left(\vec{p}\right)$, for each configuration $\vec{p}$ can be collected as rows in a matrix $\boldsymbol{X}$. Consistent with eq. (4.4), it is then possible to write

$$y=\boldsymbol{X}\vec{v} \tag{4.6}$$

where $\vec{v}$ is a column vector collecting the ECI for each cluster basis function multiplied by their multiplicity m_{α}^{π}, i.e. $\vec{v}^{\intercal}=\{m_{\alpha}^{\pi}V_{\alpha}^{\pi}\dots\}$. The problem of determining numerical values of the ECI has, therefore, been cast into a common regression problem.

In the next section, it will prove useful to categorize basis function combinations π into three groups: those that only contain p_i^A occupation variables, those that only contain p_i^B and those that contain a mix [102]. We will represent these three different types of interactions with π (pure A interactions), π' (pure B interactions), and π'' (cross interactions between A and B). This allows us to rewrite eq. (4.1) as

$$\begin{aligned}
E_f(\vec{p}) =& V_0 \\
&+ \sum_{\alpha,\pi} V_\alpha^{\pi} \phi_\alpha^{\pi}(\vec{p}) \\
&+ \sum_{\alpha,\pi'} V_\alpha^{\pi'} \phi_\alpha^{\pi'}(\vec{p}) \\
&+ \sum_{\alpha,\pi''} V_\alpha^{\pi''} \phi_\alpha^{\pi''}(\vec{p})
\end{aligned} \tag{4.7}$$

where V_0 is the ECI for the empty cluster and is equal to the formation energy of pure C [64]. Expressing the energy as in eq. (4.7) will prove advantageous for extracting ECI of a ternary alloy recursively, starting from simple binaries.

4.2.2 A recursive approach to constructing multicomponent cluster expansions

To construct a cluster expansion, we want to find the best set of ECI that reproduce the observed data, and can accurately predict DFT energies not used in the training process. Bayesian regression allows the introduction of prior probability distributions into the fit, which are used to inform the model of any knowledge we have about the system[92, 103]. A commonly used prior is the L2 regularization, which can be used to ensure a shrinkage of the fitting parameters, resulting in ECI having small magnitudes. Previous work[92] has shown how a Tikhonov regularization matrix can be used to enforce more shrinkage on particular clusters where we expect the smallest ECI values (e.g. clusters with longer lengths).

A common assumption is that the probability distribution of the ECI is centered around zero [92]. This is consistently the case whether a Gaussian distribution is used (L2 regularization) or a Laplace distribution is used (L1 regularization). One of the main challenges of fitting multicomponent cluster expansions is the steep increase in the number of interactions that need to be accounted for as the number of components increases. However, fitting a cluster expansion on any of the subsystems of a multicomponent system is relatively straightforward. We propose a method in which individual fits of the multicomponent subsystems can be used as an informative prior for the multicomponent system.

A generalized derivation of the L2 regularization will show how a set of previously established ECI from a binary fit can themselves be used as informative priors in a separate ternary cluster expansion. Though the derivation that follows assumes Gaussian distributed probabilities for all ECI, the same reasoning can be applied for L1 regularization, or other more advanced regression techniques such as automatic relevance determination[104].

We begin with Bayes theorem[105, 103], which states that for the given correlation matrix $\boldsymbol{X}$ and energy measurements $\vec{y}$ as defined in eq. (4.6), the probability of a set of ECI values $\vec{v}$ is

$$P(\vec{v}|\boldsymbol{X},\vec{y}) = \frac{P(\vec{y}|\vec{v},\boldsymbol{X})P(\vec{v}|\boldsymbol{X})}{P(\vec{y}|\boldsymbol{X})} \tag{4.8}$$

where $P(\vec{y}|\vec{v},\boldsymbol{X})$ is the likelihood and $P(\vec{v}|\boldsymbol{X})$ is the informative prior. Maximizing the likelihood results in a solution for $\vec{v}$ that minimizes the residuals (least squares), while the informative priors provide information about the expected values $\vec{v}$ should have. The priors are based on any information we have about our system, including any physical insights or previous models. The best set of ECI can be found by finding the maximum of the *a posteriori* probability estimate (MAP), which depends only on the likelihood and the prior.

$$\begin{aligned}\vec{v}_{MAP} &= \underset{v}{\operatorname{argmax}}\, P(\vec{v}|\boldsymbol{X},\vec{y}) \\ &= \underset{v}{\operatorname{argmax}}\, [\log P(\vec{y}|\vec{v},\boldsymbol{X}) + \log P(\vec{v}|\boldsymbol{X})]\end{aligned} \tag{4.9}$$

We assume normal distributions for both the observed energy values $\vec{y}$ and ECI values $\vec{v}$. The usual assumption for the distribution of the ECI values is that the probability is centered around zero. In our derivation we will not make that assumption for all the ECI values, and instead explicitly state that the distribution for v is centered around $\hat{v}$ with variance τ.

$$P(\vec{v}|\boldsymbol{X}) = \prod_i \frac{1}{\sqrt{2\pi\tau_i^2}} \exp\left(-\frac{(v_i - \hat{v}_i)^2}{2\tau_i^2}\right) \tag{4.10}$$

Similarly, we pick the mean for the distributions of the observed energies to be their expected values, with a variance $\sigma_{\vec{p}}^2$, which gives us an expression for the likelihood.

$$P(\vec{y}|\vec{v},\boldsymbol{X}) = \prod_{\vec{p}} \frac{1}{\sqrt{2\pi\sigma_{\vec{p}}^2}} \exp\left(-\frac{(y_{\vec{p}} - \vec{x}_{\vec{p}}\vec{v})^2}{2\sigma_{\vec{p}}^2}\right) \tag{4.11}$$

where $\vec{x}_{\vec{p}}$ is a row from the correlation matrix $\boldsymbol{X}$ and contains the correlations for configuration $\vec{p}$.

Inserting 4.10 and 4.11 into 4.9 we find that

$$\vec{v}_{MAP} = \underset{v}{\operatorname{argmin}} \left[\sum_{\vec{p}} \frac{(y_{\vec{p}} - \vec{x}_{\vec{p}}\vec{v})^2}{2\sigma_{\vec{p}}^2} + \sum_i \frac{(v_i - \hat{v}_i)^2}{2\tau_i^2}\right] \tag{4.12}$$

Note that some of the constant terms that are independent of $\vec{v}$ and do not affect the probability maximization have been omitted for clarity.

The value of $\sigma_{\vec{p}}$, which is usually unknown, complicates the solution of of eq. (4.12). In order to arrive at a closed form solution, we can perform a series of substitutions. Setting $\hat{v} = 0$ would yield the well established L2 regularization [92]. Instead, we define a new variable $v' = v - \hat{v}$.

$$\vec{v}_{MAP} = \underset{v}{\operatorname{argmin}} \left[\sum_{\vec{p}} \frac{\left(y_{\vec{p}} - \hat{\vec{v}}\vec{x}_{\vec{p}} - \vec{v}'\vec{x}_{\vec{p}} \right)^2}{2\sigma_{\vec{p}}^2} + \sum_i \frac{v_i'^2}{2\tau_i^2} \right] \tag{4.13}$$

By defining $y' = y - \hat{\vec{v}}\vec{x}$, and assuming σ takes a constant value, the expression takes the familiar L2 form, with $\lambda = \sigma^2/\tau^2$.

$$\vec{v}'_{MAP} = \underset{v'}{\operatorname{argmin}} \left[\sum_{\vec{p}} \left(y'_{\vec{p}} - \vec{v}'\vec{x}_{\vec{p}} \right)^2 + \sum_i \lambda_i v_i'^2 \right] \tag{4.14}$$

This shows that prior information about the expected value of certain ECI values can be inserted into the regression by recasting the training data, and constructing an appropriate Tikhonov regularization matrix. By subtracting out the energy contributions of the basis functions with known ECI values, and assigning them a high regularizing value λ, we can fit the remaining "uninformed" ECI and force the "informed" ECI to retain their original value. When picking large values of λ for "uninformed" ECI (as is the case in the usual L2 formulation), we are asserting that the probability distribution for v is sharply peaked around 0, resulting in small magnitudes. Conversely, when picking values of λ for "informed" ECI, we are effectively determining how close we expect the true value of v to be to $\hat{v}$, with large λ enforcing a small deviation from the expected value. A different value λ can be selected for each of the different ECI, allowing varying amount of confidence to be placed on the informed ECI. For our purposes, we have picked $\lambda = 0$ for all ECI involving ternary interactions, and a flat value λ for for the informed ECI, such that they reproduce the original binary groundstate formation energies within 5meV/atom.

4.2.3 Ab initio calculations

We employed density functional theory (DFT) calculations to predict the ordering preferences in the Ni-Al-Cr system. All calculations were performed with the generalized gradient approximation (GGA-PBE) using the projector augmented wave (PAW) method[34] with the Vienna ab initio Simulation Package (VASP)[37, 35, 36]. PAW potentials with 16, 3, and 12 valence electrons were used for Ni, Al, and Cr respectively (these are found in the *Ni_pv*, *Al*, and *Cr_pv* VASP potentials). Parametrizing a cluster expansion requires a large number of energies for different orderings as training data. These orderings were generated using the CASM[106, 40, 39, 41] software package by enumerating symmetrically distinct atomic combinations of Ni, Al and Cr on FCC and BCC lattices. DFT calculations were converged to within 1meV/atom by using a $23 \times 23 \times 23$ k-point mesh for a FCC primitive Ni cell, and a $17 \times 17 \times 17$ mesh for a NiAl B2 cell. The k-point meshes for enumerated supercells were scaled appropriately to maintain the same density. A relatively high energy cutoff of 560eV was employed for all calculations, and all calculations were initialized with a spin polarized ferromagnetic ordering[42]. The initial magnetic moment for Ni, Al, and Cr, was 2.5, 2.0, and 1.7 Bohr magnetons respectively. The Methfessel-Paxton method was used to first order for the numerical k-space integration through the Brillouin zone with a smearing parameter of 0.2eV. The DFT-PBE energies were calculated allowing lattice parameters and atomic positions to fully relax in order to minimize the total energy.

4.3 Results

4.3.1 Formation Energies and Groundstates

The first step towards understanding the thermodynamic behavior of an alloy such as the Ni-Al-Cr system is to determine the lowest energy phases at 0K. The Ni-Al-Cr ternary has a variety of phases that can be viewed as orderings over parent crystal structures such as FCC and BCC. Building on previous work focused on the Ni-Al binary[1], we enumerated ternary configurations within the FCC and BCC parent crystal structures and over the sublattice sites of the B2 NiAl compound. The B2 NiAl compound, having a CsCl crystal structure, accommodates off-stoichiometry in very different ways depending on whether it is Ni rich or Al rich[27]. Excess Ni in B2-NiAl is accommodated with Ni antisite defects on the Al sublattice, while an Al excess is realized by an uncommonly high concentration of vacancies on the Ni sublattice. Preliminary DFT calculations did not reveal a strong preference for either sublattice by Cr atoms. Ternary configurations in B2 NiAl were therefore enumerated by allowing Ni, vacancies, and Cr disorder on the Ni-sublattice and Al, Ni, and Cr disorder on the Al sublattice.

Figure 4.1 shows the convex hull of all calculated configurations, combined with formation energies of compounds that cannot be enumerated on an FCC or BCC lattice[107]. Formation energies for all structures were calculated relative to pure FCC Ni, FCC Al and BCC Cr, and normalized per number of atoms

$$E_f = \frac{E^{DFT} - N_{Ni}E^{DFT}_{Ni} - N_{Al}E^{DFT}_{Al} - N_{Cr}E^{DFT}_{Cr}}{N_{Ni} + N_{Al} + N_{Cr}} \tag{4.15}$$

As a measure of concentration, we use atomic fractions defined as

$$x_M = \frac{N_M}{N_{Ni} + N_{Al} + N_{Cr}} \tag{4.16}$$

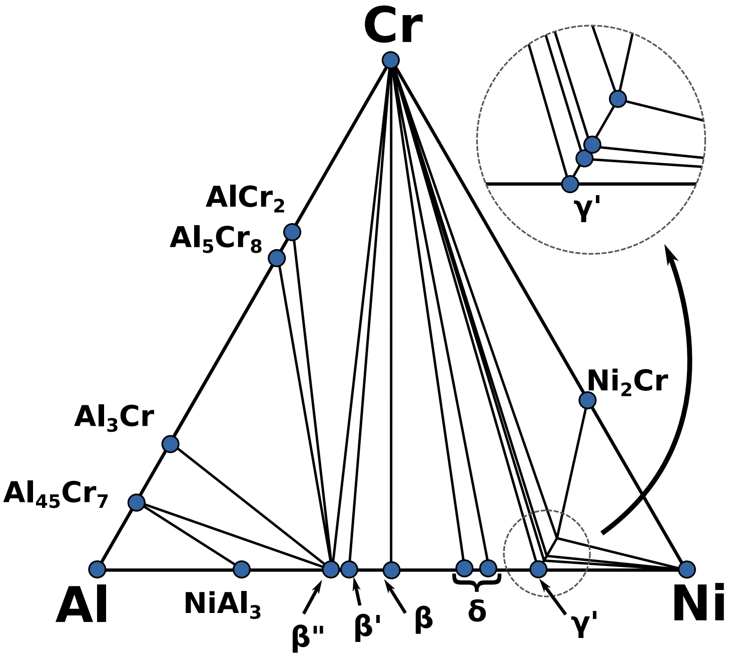

Figure 4.1: Projected convex hull of all calculated configurations, with blue circles highlighting the presence of groundstates. B2 based structures are labelled β (NiAl), β' (Ni_3Al_4) and β'' (Ni_2Al_3). The $L1_2$ based groundstates enclosed in a dashed circle (Ni_3Al, $Ni_{81}Al_{25}Cr_2$, $Ni_{27}Al_8Cr$ and $Ni_{12}Al_3Cr$) are collectively labelled γ'. An enlarged view of the $L1_2$ groundstates is shown on the upper right. The $\delta - Ni_5Al_3$ and $\delta - Ni_2Al$ groundstates are collectively labelled δ.

where M represents either Ni, Al or Cr. Table 4.1 in Supporting Information reports the formation energies of each ground state.

The binary Ni-Al alloy favors FCC derived phases at Ni rich compositions and B2-derived phases at equiatomic compositions (fig. 4.1). Pure Ni (γ) is stable in FCC, while Ni_3Al (γ') adopts the $L1_2$ ordering on FCC. A family of hierarchical orderings consisting of alternating units of $L1_0$ and $L1_2$ ordering are stable in the composition range of $0.625 \leq x_{Ni} \leq 0.667$ (x_{Cr}=0) [1]. We collectively refer to these orderings as δ, with two of them appearing on the global convex hull: $\delta - Ni_5Al_3$ and $\delta - Ni_2Al$. The β, β' and β'' phases, in contrast, are all derived from B2. The β phase corresponds to perfect B2 ordering, while β' and β'' are vacancy ordered variants of B2. The Al-rich Al_3Ni phase is unlike the other Ni-Al phases in that it is not an ordering on either FCC or BCC, but is instead isomorphic with cementite (Fe_3C).

While Al and Ni favor FCC, pure Cr prefers BCC. Figure 4.1 shows only one compound in the Ni-Cr binary. This compound, having an ideal Ni_2Cr stoichiometry, is an ordered FCC phase. It consists of (101) Cr layers alternated by pairs of (101) Ni layers as illustrated in fig. 4.2. This phase is experimentally observed to undergo an order-disorder transition around 825K[108].

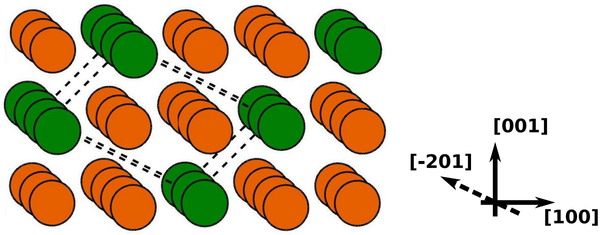

Figure 4.2: The Ni_2Cr ordering. Cr atoms (green) layers alternate with Ni (orange) as (101) planes. The structure can also be viewed as alternating layers of (102) planes. The primitive cell of this ordering is shown with dashed lines.

Though our focus lies primarily on the Ni rich side of the ternary phase diagram, we briefly describe the stable Al-Cr structures that appear as groundstates in fig. 4.1. Past experimental studies have indicated the existence of Al rich Ni-Al-Cr ternary phases, as well as Al-Cr binary phases that do not appear on our convex hull[109, 110]. Structures of reported phases in the Al and Cr rich corners that have proven difficult to characterize or that only exist at higher temperatures have been excluded from our calculations. The $Al_{45}Cr_7$ phase appearing as a groundstate on the convex hull in fig. 4.1 is an approximate structure to the experimentally observed quasicrystal, also referred to as Al_7Cr or $Al_{13}Cr_2$ [109, 111]. The Al_3Cr phase is $D0_{22}$, which is an ordering on FCC. On the Cr rich side of the Al-Cr binary, only $AlCr_2$ is reported in the literature. The ordering of this phase consists of a single Al (100) layer alternated by two Cr (100) layers within a conventional BCC cell.

Figure 4.1 shows that there are also several ternary groundstates in addition to the binary groundstates. These groundstates appear on the Ni rich portion of the convex hull, and were discovered by enumerating antisite defects in $L1_2$ superstructures. All of these ternary orderings maintain an $L1_2$ ordering, with Cr occupying exclusively the Al sublattice. The convex hull constructed from the set of calculated configurations shows 3 ordered ternary groundstates ($Ni_{81}Al_{25}Cr_2$, $Ni_{27}Al_8Cr$ and $Ni_{12}Al_3Cr$). However, we expect that further enumeration of orderings with varying distributions of Cr on the Al sublattice of the γ' phase is likely to result in the discovery of additional groundstates.

As shown in previous work[1], there is a series of configurations between $0.625 < x_{Ni} < 0.75$ ($x_{Cr} = 0$) that lie below the common tangent between δ-Ni_5Al_3 and γ'. These orderings can be constructed by combining layers of $L1_2$ and $L1_0$ along the [101] direction. The collection of these hierarchical groundstates is collectively labeled δ in fig. 4.1. Similar hierarchical orderings were found to be ground states in the Ni-Cr and Cr-Al binaries. An alternative way of visualizing the Ni_2Cr ordered phase is to view it as alternating layers along the $[\bar{2}01]$ direction, with single layers of Cr alternated by two layers of Ni (fig. 4.2). Configurations generated by increasing the number of Ni layers between those of Cr from 2 to 3 or 4 layers results in formation energies that are less than 5meV from the convex hull. Further combinations of these configurations into larger structures with a varying number of Ni layers (such as the example shown in fig. 4.3) also have very low energies. The lowest energy structure enumerated in this series is a 22 atom supercell with stoichiometry $Ni_{15}Cr_7$. In fact, DFT predicts this ordering as being a global groundstate, bringing Ni_2Cr about 3meV above the convex hull. In view of the complexity and size of the $Ni_{15}Cr_7$ superstructure ordering and its near degeneracy with the experimentally observed Ni_2Cr phase, we did not include it as part of the zero Kelvin convex hull in fig. 4.1, nor did we consider it in the construction of our cluster expansion Hamiltonian.

We found that the Cr-Al binary also exhibits hierarchical groundstate orderings. A

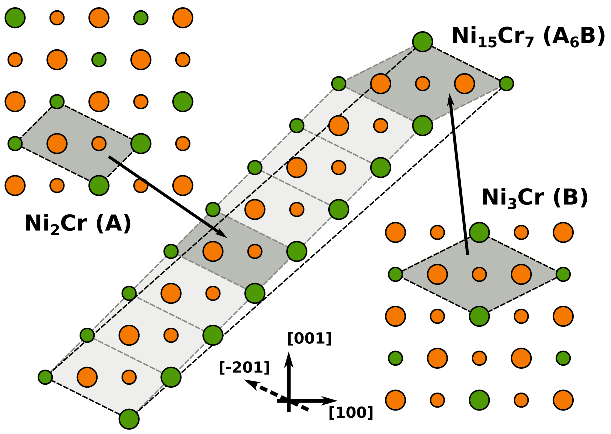

Figure 4.3: Example of a low energy stacking for Ni-Cr. The true DFT groundstate shown in the center is composed of 6 Ni_2Cr units and a single Ni_3Cr unit. Additional low energy structures can be found by combining different amounts of Ni_2Cr, Ni_3Cr, and Ni_4Cr units.

systematic enumeration led to the discovery of a previously unreported groundstate with stoichiometry Al_5Cr_8 on a BCC lattice. The Cr_2Al ordering, consisting of single Al (100) layers and double Cr (100) layers in BCC, can be combined with CrAl, which has alternating pairs of (100) Cr and Al layers in BCC. Stacking sequences such as the one shown in fig. 4.4 result in an array of low energy structures, including this new groundstate.

4.3.2 Finite temperature phase diagram

Three separate cluster expansions were constructed to model the Ni-Al-Cr ternary. Fully relaxed formation energies of different orderings on FCC, B2 and BCC were used as training data to parametrize the cluster expansions. Structures that relaxed from one parent crystal structure to another due to dynamical instabilities were identified using criteria described in [1] and were not included in the training sets. Figures 4.12 to 4.14 in Supporting Information show a comparison between the predicted and DFT formation energies for the three cluster expansions.

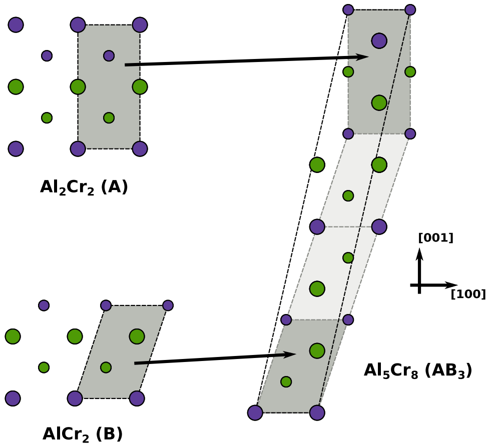

Figure 4.4: Example of a low energy stacking for Cr-Al. A new groundstate was found by combining one unit of Al_2Cr_2 with three units of the well established groundstate $AlCr_2$. Combining these units in different ratios results in additional low energy configurations.

A ternary cluster expansion was parameterized for BCC, weighting the Cr rich structures since BCC is only observed and predicted to be stable in the Cr rich corner of the ternary composition space. The coefficients of 70 basis functions were selected and parametrized using automatic relevance determination (ARD)[104] with a training set of 544 structures. The resulting cluster expansion has a root mean square error of 17meV/atom, but just 10meV/atom for configurations with $x_{Cr} > 0.8$, where the cluster expansion is required to accurately predict energies. In order to ensure that our models are predictive, we used k-fold cross validation, where k is the number of folds we split our training data into. By training on all but one of the folds k times (once for each excluded fold), we compute the cross validation (cv) score by averaging the error of all the folds that were excluded from the training set[103]. Using this method with $k = 10$, the cv score for the BCC Cr cluster expansion is 18meV/atom.

A second cluster expansion was parametrized to describe Ni-rich FCC, including γ (Ni solid solution), γ' ($L1_2$) and the ordered Ni_2Cr phase. To construct this ternary cluster expansion, we used the recursive approach described in section 4.2.2. We started with optimized binary cluster expansions for the Ni-Al and Ni-Cr binary subsystems. The ECI for FCC Ni-Al were taken from previous work[1], which was shown to accurately predict energies for the γ and γ' phases. A binary cluster expansion for the FCC Ni-Cr system with 38 binary interaction coefficients and an overall root mean square error (RMSE) of 7meV/atom was also constructed. It predicts Ni_2Cr as the only groundstate in the FCC Ni-Cr binary. A k-fold cross validation score with $k = 10$ closely tracks the RMSE value at 7meV/atom.

The two binary cluster expansions were used as informative priors to parameterize the terms of a ternary FCC cluster expansion. We picked relatively large values of λ for the binary interactions of the two subsystem cluster expansions to ensure that the ECI of the final fit accurately reproduce the predicted energies of the binaries. For the ternary interactions, no shrinkage was imposed ($\lambda = 0$), and the genetic algorithm was used to pick an additional 26 ternary basis functions, yielding a total of 110 non-zero ECI in the final ternary cluster expansion. The ternary cluster expansion also predicts $Ni_{12}Al_3Cr$ as being a groundstate, consistent with the DFT convex hull. A total of 2100 energies, of which 1290 corresponded to ternary configurations, were used to train the full ternary cluster expansion having an RMSE of 20meV/atom. At high Ni compositions ($x_{Ni} > 0.6$) where the cluster expansion is required to predict configurational energies accurately the RMSE is only 9meV per atom. Performing a k-fold ($k = 10$) cross validation on the entire data set gave a value of 23meV/atom. However, repeating the same cross validation using only high Ni compositions ($x_{Ni} > 0.6$), reduced the CV score to 12meV/atom.

A final cluster expansion was constructed to describe the configurational energy of B2 NiAl in the ternary Ni-Al-Cr composition space. As shown in our previous study [1], a binary cluster expansion that allows for vacancies on the Ni-sublattice and Ni on the Al sublattice is capable of describing the three B2-derived orderings, β, β' and β'', observed experimentally. We constructed a ternary cluster expansion for B2-NiAl that also accounts for Cr additions on both sublattices by applying the recursive approach described in section 4.2.2 to the binary cluster expansion for B2-NiAl [1]. We focused exclusively on the Ni rich side of the β phase, adding 22 additional ternary interactions to the original set of 68. The RMSE for this cluster expansion in the composition range of $0.5 \leq x_{Ni} < 0.65$ and $x_{Cr} < 0.2$ is 12meV per atom, with a k-fold ($k = 10$) cv score of 13meV/atom.

The three cluster expansions were next subjected to Monte Carlo simulations to calculate free energies of the three parent crystal structures. The simulations were performed within the semi grand canonical ensemble, where temperature, chemical potential and total number of crystal sites are the controlled variables. The composition and grand canonical energy were calculated as averages over sampled configurational microstates. Gibbs free energies were calculated with thermodynamic integration techniques [40, 112, 113].

Figure 4.5 shows a calculated phase diagram at 800K. The phase diagram was constructed by applying the common tangent construction to the calculated Gibbs free energies (δ-Ni_5Al_3 and δ-Ni_2Al phases shown as δ in fig. 4.1 were modelled as a line compounds). The binary Ni-Al and Ni-Cr phase diagrams as calculated with the same cluster expansions are shown in fig. 4.9 of Supporting Information. The calculated phase diagram predicts only a very small Ni and Al solubility in BCC Cr. A limited degree of off-stoichiometry and Cr solubility is predicted in B2 at 800K. The Ni_2Cr ordering, which is FCC based, also does not accommodate a significant degree of off-stoichiometry, exhibiting very low Al solubility. The FCC based Ni-rich solid solution (γ) and the γ'-Ni_3Al phase, in contrast, are able to dissolve a large concentration of Cr.

Figure 4.6 shows a phase diagram calculated at 1400K. This temperature is above the disorder temperature of Ni_2Cr[114, 110], which no longer appears in the phase diagram. At this temperature the β phase accommodates significantly more Al than at 800K, with only a very slight increase in Cr solubility. The free energy for β, even at these elevated

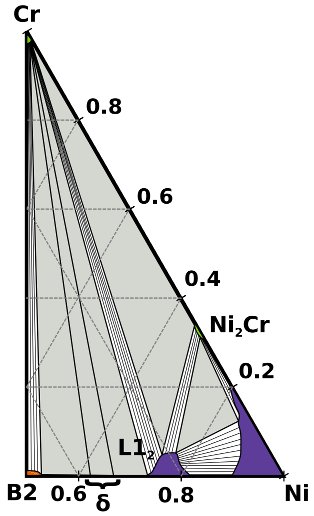

Figure 4.5: Calculated phase diagram at 800K. Single phase regions are colored, while two phase regions are white and show several tie lines. Three phase regions are shown with a gray background.

temperatures, does not decrease sufficiently at Ni-rich concentrations to destabilize the Ni_5Al_3 phase, even though this ordering is not seen experimentally at 1400K[114, 110]. As described in [1], this is likely due to the neglect of vibrational excitations, which are expected to be highly anharmonic in B2 at Ni-rich compositions. The γ and γ' phases show the most dramatic change with increasing temperature. The γ phase extends further along both the Ni-Al and Ni-Cr binaries, uniformly increasing the single phase region. The γ' phase also increases its Cr solubility. Similar to the phase diagram at 800K, the maximum Cr solubility occurs at Ni-rich compositions, reaching as high as $x_{Cr} = 0.04$ when $x_{Ni} = 0.78$.

4.3.3 Preferential occupation of Cr on $L1_2$ sublattices

The calculated phase diagrams at both 800K (fig. 4.5) and 1400K (fig. 4.6) show a high Cr solubility in the γ'-Ni_3Al phase. This phase has an $L1_2$ ordering on FCC, in which Al occupies the corner sites of the conventional FCC cubic unit cell, while Ni occupies the remaining sites. Along the Ni-Al binary, γ' accommodates Ni excess with

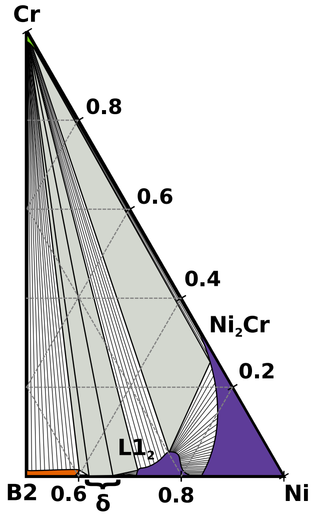

Figure 4.6: Calculated phase diagram at 1400K. The solubility of γ' has extended and Ni_2Cr has undergone a disorder transformation.

Ni anti-site defects on the Al sublattice and Al excess with Al antisite defects on the Ni sublattice. The DFT calculations at zero Kelvin predict that Cr prefers to reside on the Al sublattice of the $L1_2$ ordering. This behavior persists at elevated temperature. The Cr distribution over the two distinct $L1_2$ sites at elevated temperature can be tracked within Monte Carlo simulations with the aid of sublattice concentrations. Figure 4.7 shows the Cr concentration on the the Al sublattice of $L1_2$, while Figure 4.8 shows the Cr concentration on the Ni sublattice of $L1_2$. As is clear from both figures, Cr almost exclusively resides on the Al sublattice with negligible occupancy of the Ni sublattice.

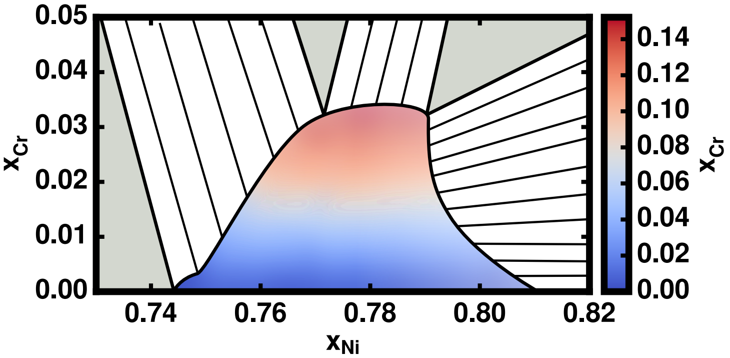

Figure 4.7: Cr composition of the Al sublattice of $L1_2$. The composition on this single sublattice very closely tracks the global Cr concentration.

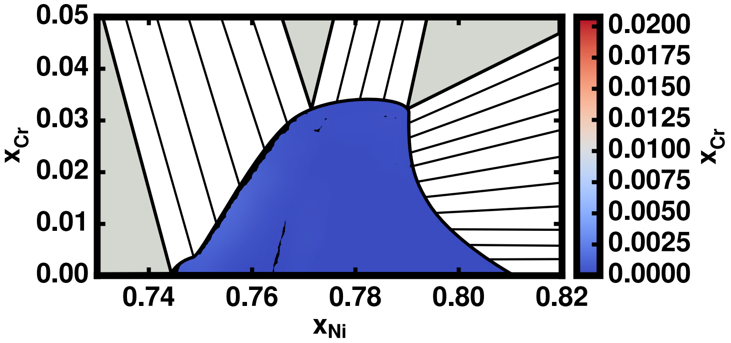

Figure 4.8: Average Cr composition for all three Ni sublattices of $L1_2$. The Cr concentration of these sublattices remains close to zero despite an increase in the global Cr concentration.

4.4 Discussion

Many methods have been developed to parameterize alloy cluster expansion Hamiltonians. The reliance on a cross validation score opened the door to more automated approaches of selecting the basis functions that are to be included in a truncated cluster expansion [95]. Other innovations have included the use of genetic algorithms [115] and compressive sensing approaches [91, 90] to select a sparse cluster expansion Hamiltonian. Bayesian approaches have been introduced to exploit prior knowledge [92] and have been particularly effective in the construction of cluster expansion Hamiltonians for nano-particles [116]. Recent advances exploit non-linear programming techniques to impose constraints that ensure that the cluster expansion predicts the correct ground states [93]. Approaches developed so far, however, parameterize all terms of the final cluster expansion simultaneously.

Here we have introduced a recursive approach to build multi-component cluster expansion Hamiltonians starting with well-optimized Hamiltonians for its subsystems. This means that the first-principles parameterization of a ternary cluster expansion Hamiltonian, for example, can be informed by optimized fits of binary subsystems. The approach uses information about the interaction coefficients of the lower-dimensional subsystems as Bayesian priors when fitting higher order systems. A major advantage of this approach is that it guarantees that the cluster expansion Hamiltonian for a ternary alloy, for example, faithfully replicates the predictions of well-optimized binary Hamiltonians. This is evident in figs. 4.10 and 4.11 of Supporting Information, which compare the binary Ni-Al and Ni-Cr phase diagrams as calculated with optimized binary cluster expansions to those calculated with the ternary cluster expansions constructed by using the binary expansions as informative priors. The approach complements the multitude of other methods that have been introduced to parameterize cluster expansions and can be used in combination with them. Here, for example, we used the recursive approach together with a genetic algorithm to select an optimal basis set.

The recursive approach opens the door to systematic Hamiltonian parameterizations of multi-principle element (MPE) alloys (also referred to as high entropy alloys), which are currently receiving much attention due to their multitude of promising properties [84, 85, 86, 87, 88, 89]. The recursive approach will enable a higher degree of self-consistency between cluster expansions in high dimensional composition spaces and those that have been parameterized in all the lower-dimensional subsystems.

In the approach introduced here, we have only used the values of the interaction coefficients of lower dimensional Hamiltonians as prior knowledge, neglecting other information that may be available from a cluster expansion parameterization, such as an estimate of the spread on each interaction coefficient. A sensitivity analysis, as developed by Zabaras and co-workers [117], for example, will also provide information about the spread on each interaction coefficient of the lower dimensional subsystem that can be utilized in the formulation of the recursive approach of section 4.2.2.

As Sanchez [48, 100] and Asta et al[118] have shown, there is some flexibility in the mathematical form of the cluster basis functions. To preserve orthonormality between cluster basis functions with respect to a particular scalar product [47, 48, 118], it is common to rely on Chebyshev polynomials for the site basis functions. While appealing due to their orthogonality properties, these basis functions are less suited for a recursive approach as developed here since it is difficult to express an n-component cluster expansion as a sum of $n-1$ component cluster expansions plus cross terms. Here we have relied on a 'lattice gas' formulation of a cluster expansion, which, for an n component system, is explicitly expressed in terms of $n-1$ site occupation variables, p_i^E, that are each either 1 or 0 depending on whether or not site i is occupied by element E. Cluster expansions expressed in terms of these occupation variables can be written as a sum of subsystem cluster expansions plus higher order interactions.

The recursive parameterization of cluster expansions has enabled us to construct ternary Hamiltonians for the FCC and B2 phases in the Ni-Al-Cr system by building on well optimized binary cluster expansions for these phases. In the Ni-rich portion of the ternary phase diagram, there are two intermetallic compounds that can be viewed as orderings over FCC: the well-known $L1_2$ Ni_3Al phase (γ') and Ni_2Cr. There are no qualitatively distinct ternary ordered compounds in the Ni rich corner. Rather the ternary groundstate orderings are derivatives of γ'-Ni_3Al, with Cr simply replacing a fraction of Al on the Al sublattice of the $L1_2$ ordering. These zero Kelvin groundstates have already disappeared at 800K, but the solubility of Cr in γ' Ni_3Al remains high. The Ni_2Cr compound, in contrast only tolerates a small concentration of Al. This is likely due to the strong stability of γ' Ni_3Al, which forms tie lines with Ni_2Cr. The predicted Cr solubility in B2-NiAl is surprisingly low. Experimentally assessed phase diagrams of the Ni-Al-Cr ternary report higher Cr solubility limits in B2[114, 110]. As pointed out in a detailed study of the Ni-Al binary [1], it is likely that anharmonic vibrational excitations are important in determining thermodynamic properties of Ni-rich B2. The neglect of these excitations in this study may be at the origin of the underpredicted Cr solubility in B2.

All DFT calculations used to parameterize the cluster expansions were initialized in the ferromagnetic state. Ni-rich FCC is ferromagnetic while $L1_2$ Ni_3Al relaxes to a non magnetic state. We found that the energy of Ni_2Cr is insensitive to whether it is initialized ferromagnetically or anti-ferromagnetically. It is well known, however, that BCC Cr prefers antiferromagnetic ordering [119, 120]. Our treatment neglects the enthalpic and entropic contributions to the free energy from the long and short-range antiferromagnetic ordering that exists in the Cr rich BCC phase. The simultaneous treatment of both chemical and magnetic configurational degrees of freedom is possible with a magnetic cluster expansion [120, 121]. The inclusion of the additional magnetic degrees of freedom will lower the free energy compared to that calculated here and thereby increase the predicted Ni solubility in the Cr-rich bcc phase. However, since the focus has been on the Ni-rich portion of the ternary phase diagram, an explicit treatment of magnetic configurational degrees of freedom in the Cr-rich BCC phase is beyond the scope of this study.

Our systematic enumeration of low energy orderings over FCC and BCC in the Ni-Al-Cr system led to the discovery of several families of hierarchical orderings. In addition to the family found to be stable in the Ni-Al binary between $0.625 < x_{\mathrm{Ni}} < 0.75$ [1], such orderings were also found to be ground states in the Ni-Cr and Cr-Al binaries. Hierarchical orderings are long-period superstructures built by periodically tiling blocks of simpler orderings. Different combinations of simpler orderings result in more complex orderings that can span a range of compositions. In the case of the Ni-Cr system, the existence of these low energy structures could help explain the short range ordering observed in Ni_2Cr alloys during ageing[122, 99, 123, 124, 108, 125]. The short range order may be a product of the atomic arrangement within the tiling blocks, while the arrangement of the blocks themselves remain disordered. Similar hierarchical orderings were recently also discovered to be stable in HCP based Mg-rare earth alloys [57, 126, 112] and are likely common in many other alloy systems.

4.5 Conclusion

We have developed a method for parametrizing multicomponent cluster expansions recursively, using cluster expansions of lower order subsystems as informative priors. We applied this approach to study phase stability in the Ni-Al-Cr ternary, building on detailed studies of the Ni-Al and Ni-Cr binaries. The resulting cluster expansions predict a significant Cr solubility in both the γ and γ' phases at high temperatures. In the $L1_2$-ordered γ' phase, Cr almost exclusively occupies the Al sublattice. Our systematic study of low energy orderings over FCC, BCC and B2 in the Ni-Al-Cr ternary led to the identification of previously unreported long-period hierarchical ordered groundstates in the Al-Cr and Ni-Cr binaries.

4.6 Acknowledgements

This research was supported by the National Science Foundation (DMR-1105672). Computational resource support was provided by the Center for Scientific Computing at the CNSI and MRL: an NSF MRSEC (DMR-1121053) and NSF CNS-0960316. Crystal structure images were generated using VESTA [82], and plots were generated using matplotlib [83]. We thank Ben Bales for helpful discussions.

4.7 Supplementary data

4.7.1 Groundstate energies

The convex hull of a ternary system can be difficult to interpret, due to being 3 dimensional. The general location of the existing groundstates of the Ni-Al-Cr system is most readily seen in fig. 4.1, but does not reveal any information about their relative energies. Here we provide the formation energies of each of the highlighted groundstates, relative to FCC Al, FCC Ni, and BCC Cr.

Groundstate	x_{Ni}	x_{Al}	E_f [eV/atom]
Al (FCC)	0.0000	1.0000	0.000
$NiAl_3$	0.2500	0.7500	−0.399
β''	0.4000	0.6000	−0.613
β'	0.4286	0.5714	−0.628
β	0.5000	0.5000	−0.659
δ-Ni_5Al_3	0.6250	0.3750	−0.565
δ-Ni_2Al	0.6667	0.3333	−0.527
γ'	0.7500	0.2500	−0.432
$Ni_{81}Al_{25}Cr_2$	0.7500	0.2314	−0.408
$Ni_{27}Al_8Cr$	0.7500	0.2222	−0.396
$Ni_{12}Al_3Cr$	0.7500	0.1875	−0.345
Ni (γ)	1.0000	0.0000	0.000
Ni_2Cr	0.6667	0.0000	−0.026
Cr (BCC)	0.0000	0.0000	0.000
$AlCr_2$	0.0000	0.3333	−0.131
Al_5Cr_8	0.0000	0.3846	−0.144
Al_3Cr	0.0000	0.7500	−0.142
$Al_{45}Cr_7$	0.0000	0.8654	−0.117

Table 4.1: Summary of the formation energies of the groundstates show in fig. 4.1. Formation energies are calculated relative to the sable endstates: FCC Ni, FCC Al, and BCC Cr.

4.7.2 Binary phase diagrams

The ternary phase diagrams presented in figs. 4.5 and 4.6 were constructed by recursively creating a ternary cluster expansion starting from independent binary cluster expansions. One of the benefits of this method is being able to retain the nature of the starting binary cluster expansions in the final ternary cluster expansions. Figure 4.9 shows binary phase diagrams constructed from the Ni-Al-Cr ternary cluster expansions. A comparison between the predicted phase diagrams from the original binary cluster expansion and the ternary cluster expansions is shown in fig. 4.10 and fig. 4.11. In both the Ni-Al and Ni-Cr systems, the phase diagrams from the binary and ternary cluster expansions match up very closely. The degree to which the ternary cluster expansion replicates the binary one can be adjusted by tuning the λ parameter described in section 4.2.2.

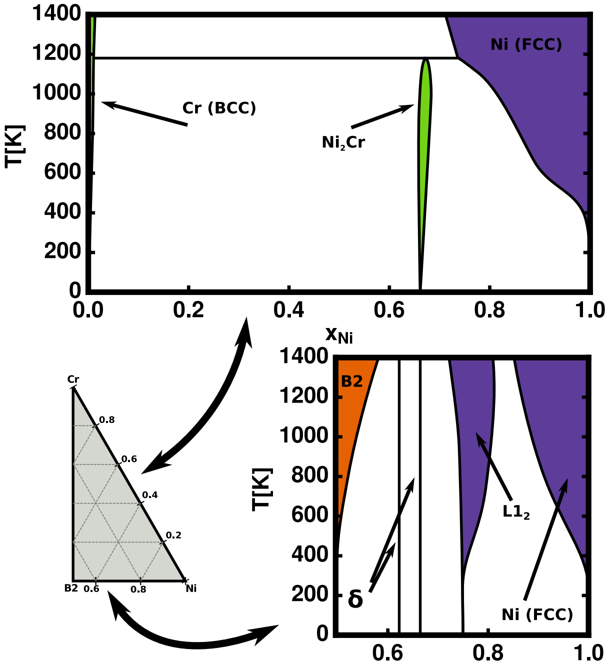

Figure 4.9: Predicted binary phase diagrams for the Ni-Al (below) and Ni-Cr (above) subspaces of Ni-Al-Cr cluster expansions. Each of the two binary phase diagrams corresponds to one side of the ternary phase diagrams shown in figs. 4.5 and 4.6.

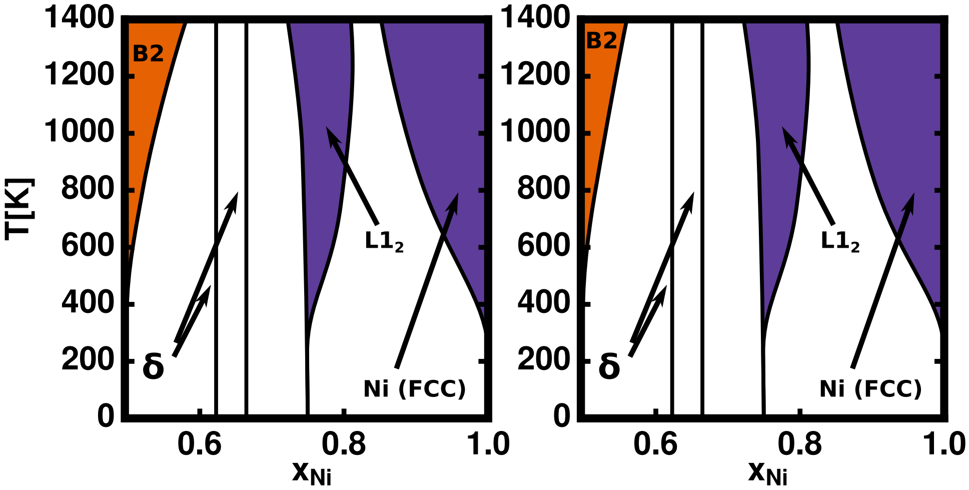

Figure 4.10: Predicted phase diagrams for the Ni-Al system: using the ternary cluster expansions (left), and the original binary cluster expansions that were used to recursively construct the ternary cluster expansion (right).

4.7.3 DFT vs cluster expanded energies

A useful cluster expansion must be able to accurately predict the formation energy of arbitrary atomic configurations. Figures 4.12 to 4.14 compare the values of the DFT energies used as training data against the predicted energy from the resulting final cluster expansions.

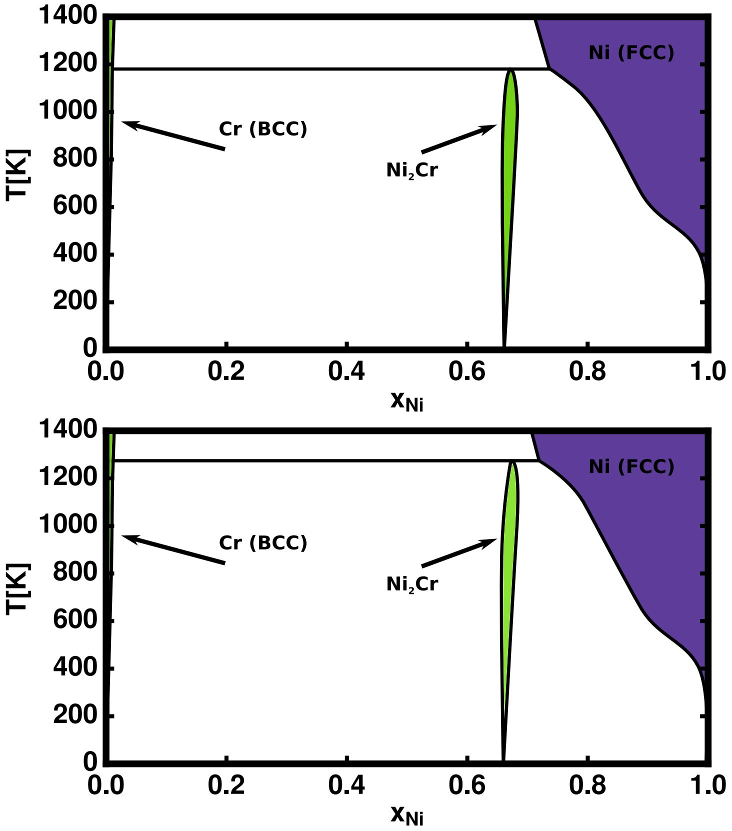

Figure 4.11: Predicted phase diagrams for the Ni-Cr system: using the ternary cluster expansion (above), and the original binary cluster expansion (below).

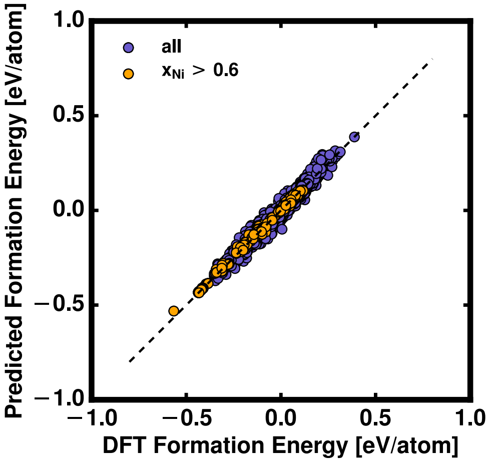

Figure 4.12: Comparison between the cluster expansion predicted energies and the DFT energies for the FCC Ni-Al-Cr system. Points highlighted in orange correspond to configurations with a composition where the cluster expansion was used to generate free energies during Monte Carlo simulations.

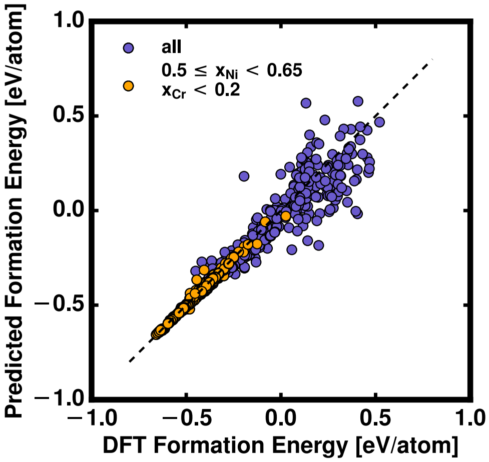

Figure 4.13: Comparison between the cluster expansion predicted energies and the DFT energies of ternary Ni-Al-Cr configurations enumerated from B2. Points highlighted in orange correspond to configurations with a composition where the cluster expansion was used to generate free energies during Monte Carlo simulations.

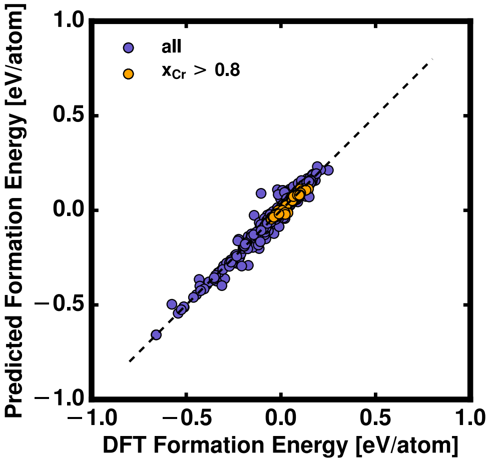

Figure 4.14: Comparison between the cluster expansion predicted energies and the DFT energies of ternary BCC Ni-Al-Cr system. Points highlighted in orange correspond to configurations with a composition where the cluster expansion was used to generate free energies during Monte Carlo simulations.

Chapter 5

Diffusive hops and their local environments

5.1 Introduction

Atomic diffusion within a crystal is a property of interest for many different applications. The rate at which thermodynamically stable solid phases will form is often determined by the atomic transport within the material. In battery technology for example, fast diffusion through a solid electrolytes is desirable. On the other hand, diffusion controlled depletion of Al from bond coats used in Ni-Al superalloy turbine blades lead to degradation.

In alloys, diffusion typically occurs by exchange of vacancy defects in the crystal with neighboring sites. As such, an activation energy ΔE must be overcome in order for the atomic exchange to take place. This activation barrier is the difference in energy at the activated state and the energy of of the initial state of the hop. In the dilute limit, the value for ΔE can be considered constant, since the environment of every hop event is identical. However, as concentrations become non-dilute, or if hops are occurring within an ordered phase, the value of ΔE becomes more difficult to model, as it depends on the local degree of order surrounding the vacancies.

Previous work has already shown how a local cluster expansion can be used to parameterize the dependence on local environments of the activation barrier. In order to train the local cluster expansion model, activation barriers within different environments must be calculated. The FCC phases of the Ni-Al binary exhibit a wide variety of long and short range order. FCC phases of the Ni-Al binary include the Ni rich solid solution, and the $\mathrm{Ni_3Al}$ $\mathrm{L1_2}$ ordering. These correspond to the γ and γ' phases respectively, and make up the bulk of superalloy turbine blades. In this work we systematically explore the diffusion pathways within these ordered structures, and compare the energetic cost of atomic migrations under different local environments.

5.2 Methods

Substitutional diffusion in a crystal is mediated by vacancy exchange. The first step towards a complete enumeration of diffusion environments is understanding the possible exchange mechanisms that can occur in the crystal. In most substitutional alloys, such as FCC Ni-Al, vacancies are dilute, and migration occurs by an exchange with a nearest neighbor atom. In FCC, the vacancy is surrounded by 12 nearest neighbors, all of which are candidates for a diffusion hop. Other systems may involve more complex exchange mechanism. Such is the case for the B2 ordering of Ni-Al, in which vacancies are known to exchange not only with their nearest neighbors, but their second nearest neighbors. Other possible mechanisms may involve more than just a single vacancy and single atom. For example, more than two sites may participate in a ring mechanism, where each atom exchanges places with a neighbor in a cyclical manner. Schematic representations of these mechanism are shown in fig. 5.1.

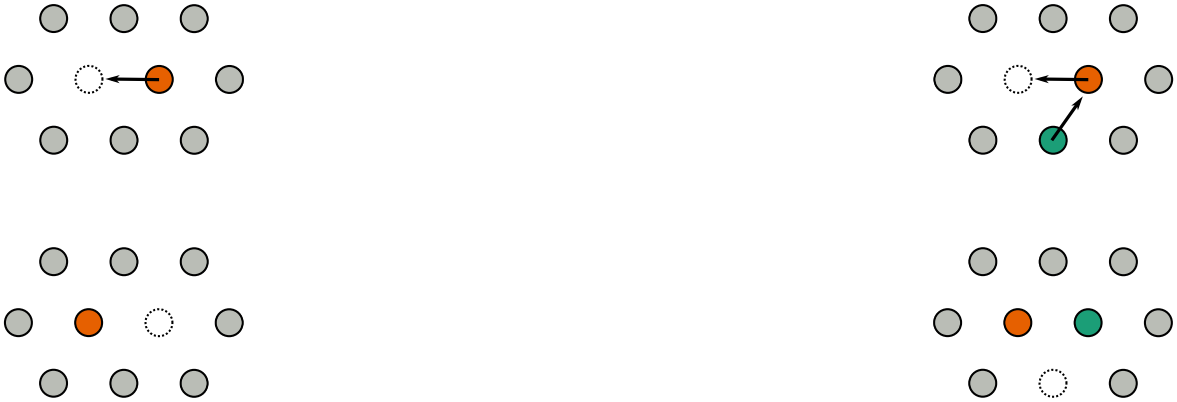

(a) (b)

Figure 5.1: Schematic illustration of a nearest neighbor vacancy exchange (fig. 5.1a), and a cyclic hop (fig. 5.1b). Participating atoms are colored, while vacant sites are shown with a dashed circle.

The activation barrier of any particular kind of hop depends on the identities of the hopping atoms, as well as their relative positions. In FCC Ni for example, we expect a different activation energy for a Ni atom exchanging with a vacancy as we do for an Al atom undergoing the same exchange. Additionally, the local environment surrounding the migration path will influence the activation energy. In FCC, an atom moving into a nearest neighbor vacancy must pass through a rectangle of 4 atoms, as shown in fig. 5.2. We will refer to these 4 atoms as the Activated Coordination Environment (ACE). Examples of local perturbations on the ACE are shown in fig. 5.2.

Due to the proximity of the ACE atoms to the migration path, we can expect their ordering to have the most significant impact on the activation energy. However, atomic shells at further distances will also influence the energetics of the hop. The $L1_2$ ordering for example, results in environments beyond the ACE that are very different than those encountered in the disordered dilute γ phase. These differences in further shells will also have an influence on the migrating atom. In the case of $L1_2$, this manifests itself as two distinct migration environments: one for an exchange occurring between two Ni sublattice sites, and another for an exchange between an Al and a Ni sublattice. These

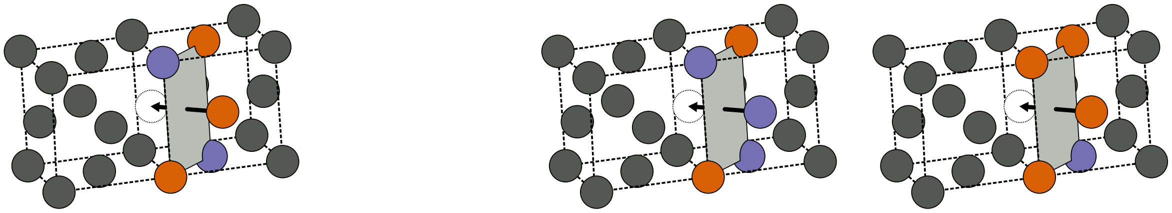

Figure 5.2: Examples of possible ACE environments. Ni atoms are shown in orange, while Al is colored purple. Vacant sites are represented with white. Atoms at greater distances from the migration path are shown in gray. Figure 5.2a and fig. 5.2b have identical ACE environments, but the type of atom migrating is different. In both fig. 5.2a and fig. 5.2c Ni is the diffusing atom, but the local environments differ. The result is a different activation energy for all three cases.

hops are illustrated in fig. 5.3, which show the single migration environment of pure Ni, and the two possible ones of the L1$_2$ ordering.

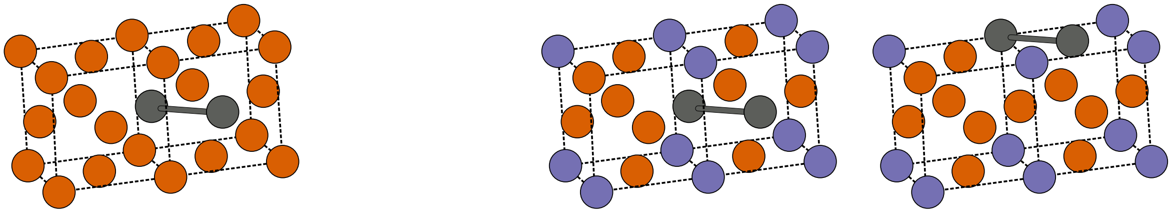

Figure 5.3: The absence of ordering of pure Ni results in the single hop environment shown in fig. 5.3a. In the L1$_2$ ordering, hops can occur between two Ni sublattices (fig. 5.3b), or between an Al and a Ni sublattice (fig. 5.3c). Sites in the hop cluster are shown in gray.

Local perturbations in the local environment will affect the value of the migration barrier. Such perturbations will arise naturally for off-stoichiometric compositions, or due to disorder that emerges at higher temperatures. We can enumerate configurations for these types of perturbations by applying antisite defects in the local environment of the hop. Some of these local perturbations will be equivalent due to they symmetry of the crystal. Figure 5.3c for example, shows a local perturbation where a single Al atom is in the ACE. The symmetry of the FCC crystal is such that placing an Al atom on any of the four ACE sites is symmetrically equivalent.

Diffusion hops in the bulk are rare events and can be approximated to occur in an infinite crystal far away from symmetry breaking defects. For a particular type of hop, equivalence of the local ordering is determined by a subgroup of the crystal space group. This subgroup, which we refer to as $\mathcal{L}$, is an intersection of a hop symmetry group $\mathcal{H}$ and the space group $\mathcal{S}$. In the case of a pair hop cluster (such as the nearest neighbor exchange in FCC Ni-Al), $\mathcal{H}$ is simply the point group of the hop cluster. However, for hop clusters involving more than two sites, the occupants participating in the hop mechanism must be accounted for. For any hop cluster, we can define a start and an end state, which defines what the occupants on the hop cluster are before and after the hop has taken place. Which state of the states is considered initial or final is arbitrary. Examples of two different possible hops for a cyclic 3-point hop cluster are shown in fig. 5.4. When determining the operations belonging to $\mathcal{H}$, the relevant symmetry to consider is that of the superposition of the initial and final states. Any operation that maps the sites of the hop cluster onto themselves, while accounting for the superposition of the occupants is a member of $\mathcal{H}$. Any locally perturbed ordering that can be mapped onto itself using $\mathcal{L} = \mathcal{H} \cap \mathcal{S}$ is then equivalent by symmetry.

There are different possible algorithms to generate local environments around a particular hop. Here we use a two step approach. First we identify important low energy, long range ordered structures, such as FCC Ni and the $L1_2$ groundstates. Within each of these groundstates, we identify different environments the hop can be placed in. Figure 5.3 shows the environments that exist for a nearest neighbor exchange in pure Ni and in the $L1_2$ ordering. Lastly we generate additional local orderings by applying perturbations to each of these environments. Examples of possible local perturbations are shown in fig. 5.2. A representative set of hops can therefore be enumerated with the following steps:

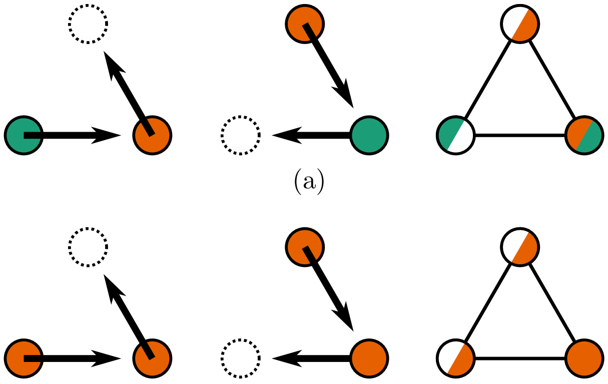

(a)

(b)

Figure 5.4: Different types of possible hops for the same three point hop cluster. The occupants of the hop cluster determine the operations of $\mathcal{H}$, which in turn determines which local orderings are symmetrically equivalent. Rather than considering the occupation of the hop cluster in its initial or final state, operations of $\mathcal{H}$ map the superposition of the initial and final occupants onto themselves. Figures 5.4a and 5.4b show examples of different occupants on the same hop cluster during the initial and final states, as well as their superposition.

1. Identify the exchange mechanism, and the cluster of sites associated with the hop. This is usually a nearest neighbor hop, but could be next nearest neighbor, or a triplet cluster for a cyclic mechanism. Hops with different types of atoms participating in the migration are considered distinct (for FCC Ni-Al, the two possible hops are a Ni-vacancy and an Al-vacancy nearest neighbor exchange).
2. For each hop cluster, find the environments that exist within each long range ordering (one in pure Ni, two in $L1_2$).
3. For each hop environment, apply symmetrically distinct local perturbations to the crystal within a certain radius of the migration path (antisite defects in the ACE).

5.2.1 Local cluster expansion formalism

There are three critical energy values associated with any diffusion hop within a crystal: the energy of the starting configuration E_i, the energy of the activated state E^*, and the energy of the end configuration E_f. In alloys, diffusion can be approximated by a series of stochastic hop events, where vacancies exchange with neighboring atoms of the crystal and then thermalize . For each of these hop events, the value of the activation energy ΔE depends not just on the local environment, but on the direction of the hop, i.e. which of the two possible endstates is considered to be "initial" and which is considered to be "final". This dependence on directionality complicates the relationship of a ΔE with its local environment, but can be simplified by instead relying on the Kinetically Resolved Activation (KRA), defined as

$$\Delta E^{KRA} = E^{*} - \frac{E_i + E_f}{2} \tag{5.1}$$

Figure 5.5 illustrates how the hop direction changes the value of ΔE, and how both the forward and backward energies can be collapsed into a single KRA value. If the KRA and endstate energies are known, the activation energy can be recovered:

$$\Delta E = E^{*} - E_i = \Delta E^{KRA} + \frac{E_f - E_i}{2} \tag{5.2}$$

In essence, the KRA separates the kinetic component of the hop from the thermodynamic endstates. While the KRA is independent of the hop direction, it will still depend on the degree of local ordering surrounding the hop.

A cluster expansion can describe the value of the KRA as a function of order/disorder around the hop cluster. In a binary alloy, we can assign occupational variables p to each site on the crystal that either take a value of 0 or 1, the entire local configuration can be described as an occupational vector $\vec{p}$. The energy of a KRA for a particular

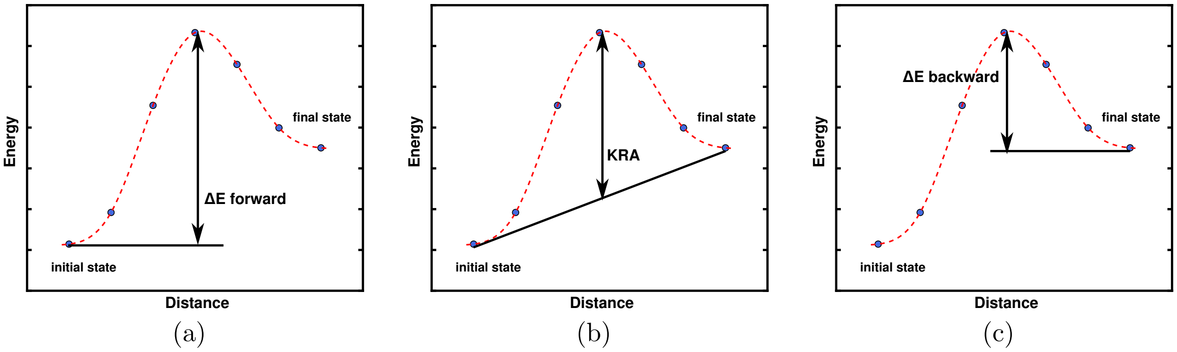

(a) (b) (c)

Figure 5.5: Example of how the activation energy changes based on the direction of the hop. The KRA captures the initial, end, and activated energies in a single value.

configurational ordering can then be expressed as

$$\Delta E^{KRA} = \sum_{\alpha} V_{\alpha}^{KRA} \phi_{\alpha} \tag{5.3}$$

where the cluster functions ϕ are defined as

$$\phi_{\alpha} = \prod_{i \in \alpha} p_i \tag{5.4}$$

The cluster functions ϕ are products of symmetrically unique combinations of the site occupational variables p that define the occupation of each site in α. Here α is a clusters of sites, such as points, pairs, triplets, etc of variable lengths and geometries. The coefficients V^{KRA} are the local Effective Cluster Interactions (ECI), and are determined from first principles calculations.

This is an identical formalism to that of the global cluster expansion, the only difference being the symmetry operations used to determine which clusters (and therefore cluster functions ϕ) are equivalent. Symmetry imposes constraints on the number if independent interaction coefficients needed to be parameterized. In the case of a global cluster expansion, the space group of the crystal $\mathcal{S}$, which contains translations, determines the equivalence between clusters. When constructing a local cluster expansion, the symmetry equivalence is checked using $\mathcal{L} = \mathcal{H} \cap \mathcal{S}$, where $\mathcal{H}$ is the point group of the hop cluster, and lacks translational symmetry. A local cluster expansion therefore not only a truncation in terms of the size of the clusters and the cluster lengths, but also a truncation in terms of distance from the hop cluster of sites that participate in the exchange mechanism.

In the case of an FCC crystal such as the Ni-Al γ and γ' phases for example, only a single point cluster exists, because all sites of an FCC structure can be mapped to each other with the symmetry operations of the crystal. However, if we generate point clusters around a local environment, there are an infinite number of distinct point clusters, each at different distances from the diffusion path.

Note that a different cluster expansion is required for each distinct hop mechanism. Even though a Ni-vacancy exchange and an Al-vacancy exchange share the same sites in their hop cluster, they are considered different mechanisms, and their interaction with the local environment will differ.

5.2.2 DFT calculations

A practical way to calculate barriers is to use Density Functional Theory (DFT), placing a particular hop within a supercell. The nudged elastic band method (NEB) available in the Vienna Ab Initio Simulation Package (VASP) is an effective way of calculating formation energies at different stages of the atomic migration. In this method, a number of images are interpolated between the start and end configurations, and energies are calculated for each one. Before these images can be interpolated, the endstate configurations must be relaxed. We fixed the lattice parameter for all of our calculations, allowing only the positions of ions to relax. For transitions within pure Ni, we chose the

DFT relaxed lattice parameter of Ni, and for transitions within $L1_2$, we chose the relaxed lattice parameter of the $L1_2$ groundstate. The assumption under these conditions then is that the perturbations within our supercell are dilute enough to not interact with their periodic image. Once the endstates were converged, we interpolated a total of 7 images for the NEB calculations, including the endstate configurations. An example of how the energy changes throughout the diffusion pathway can be seen in fig. 5.6. Each energy corresponds to one of the interpolated images, with a cubic spline fit between them.

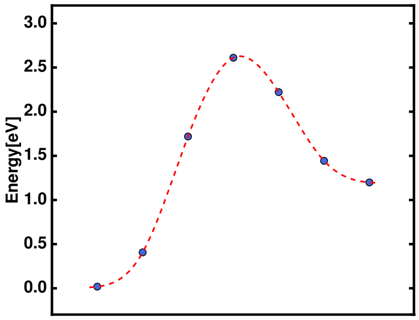

Figure 5.6: Example calculation for an Al transition between two symmetrically distinct endstates. The energies of the start and end configurations differ, resulting in an asymmetry of the path direction.

All calculations were performed with the generalized gradient approximation (GGA-PBE), using the projector augmented wave (PAW) pseudopotential method. Calculations were performed with the generalized gradient approximation (GGA-PBE), using the projector augmented wave (PAW) pseudopotential method. Calculations for all KRA values were done inside a 108 $3 \times 3 \times 3$ conventional FCC supercell, for which we chose a k-point mesh of $4 \times 4 \times 4$, with a smearing parameter of 0.2eV. We applied spin polarized ferromagnetic ordering to all supercells, and employed a plane wave cutoff energy of 560eV to ensure accuracy in our calculations.

The NEB method will work for any of the enumerated hops, but it is computationally expensive. For systems where the diffusion pathway is expected to have only a single maximum, as is the case in the FCC Ni-Al system, the symmetry of some hops can be exploited to reduce computational time. If a mirror plane exists perpendicular to the diffusion pathway, the KRA value can be determined by calculating only one intermediate image in addition to the endstate configurations. If all atoms in the supercell are placed in their ideal FCC coordinates, then putting the migrating atom exactly on the mirror plane will result in a relaxation where the symmetry of the supercell keeps the migrating atom from falling into either of the endstate positions. Such a calculation does not require the NEB method, and drastically reduces computation time. If the assumption of a single maximum through the diffusion path is correct, then its value corresponds to this balanced configuration. This type of mirror plane exists for all the ACE decorations in pure Ni, as well as a subset of the $L1_2$ local orderings, namely for the decorations around hops occurring between two Ni sublattices. An example of this sort of calculation can be seen in fig. 5.14, which shows only a single intermediate image, corresponding exactly to the maximum energy of the diffusion path.

5.3 Results

We calculated KRA values for both Ni and Al nearest neighbor vacancy exchange hops, in different local environments within pure Ni and the $L1_2$ Ni_3Al ordering. In order to get a good understanding of non-dilute behavior, local environments for these hops were enumerated in both pure Ni and the $L1_2$ ordering. The vacancy composition in these two orderings is known to be low, so the local perturbations did not include vacancy defects, only antisite defects, which were limited to the 4 atoms in the ACE. By calculating barriers in both FCC Ni and $L1_2$, we also sample variations in concentration and ordering in shells beyond the ACE. In addition, we also calculated barriers at different volumes to separate the effect of volume from local variations in concentration and ordering.

5.3.1 ACE environment

For pure Ni, there is only one distinct environment for an atom-vacancy exchange, namely an exchange between two nearest neighbor sites. The $L1_2$ ordering on the other hand, breaks translational symmetry that produces two distinct possible hops: one between two different Ni sublattice sites, and another between an Al sublattice site and any of its nearest neighbor Ni sublattice sites. The local environments of these hops in the absence of local antisite perturbations are shown in fig. 5.3. The mirror plane bisecting the diffusion path in pure Ni is preserved for $L1_2$ when the hop occurs between two Ni sublattice sites, but is no longer present in $L1_2$ when the hop is between an Al and Ni sublattice site. Starting from these hop environments, we created additional local perturbations by putting antisite defects on the ACE.

Using DFT, we calculated KRA values in these different local environments for both a Ni-vacancy hop and an Al-vacancy exchange. The KRA values are plotted as a function of the global and local ACE composition in figs. 5.10 and 5.11. There is a striking difference in the dependence on the ACE concentration for Ni and Al migrations.. Regardless of local and long range ordering, Ni KRA values remain constant to within 250meV. On the other hand, Al KRA values show a clear linear dependence on the ACE composition. Furthermore, long range ordering in the crystal seems to impact Al KRAs as well, as evidenced by a systematic shift of KRA values down when in $L1_2$ vs KRA values in pure Ni for the same ACE ordering.

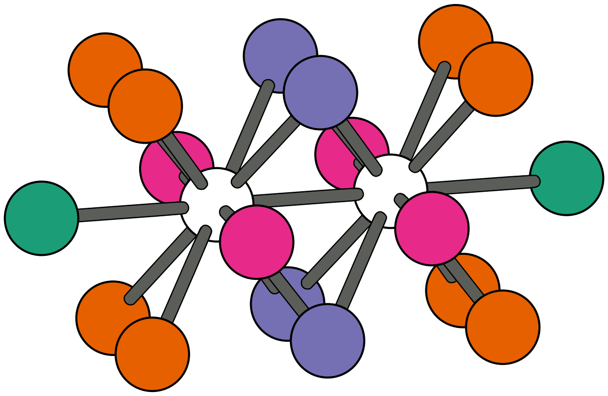

Figure 5.7: Local environment of a diffusion path in FCC. Sites participating in the vacancy exchange are white, the rest of the colors represent groups of symmetrically equivalent sites under local symmetry. The purple sites are of special interest, since they are closest to the diffusion path. We refer to these 4 atoms as the Activated Coordination Environment. Though only the purple sites in ACE were perturbed to generate environments for KRA calculations, all atoms were accounted for during the cluster basis set generation.

5.3.2 Local cluster expansion

Two local cluster expansions, one for Ni, and another for Al KRA values, were constructed, using a genetic algorithm approach as to select basis functions having non-zero expansion coefficients. Figure 5.7 shows 4 different shells of atoms around the hop, each with a different color, where each shell is a collection of symmetrically equivalent atoms under local symmetry. The pool of available cluster interactions contained up to 3-body terms for any combination of atoms of the 4 shells, any atoms further out were assumed to have a negligible effect. A total of 22 Ni KRAs and 21 Al KRAs were used as training sets. The cluster expansion for Ni was constructed using 4 local basis functions, and has a leave-one-out cross validation (LOOCV) score of 62meV. For the Al KRA expansion, the LOOCV score is 69meV, using a total of 5 basis functions to predict KRA values. The magnitudes and selected clusters can be seen in figs. 5.8 and 5.9. The predicted KRA values of both fits are contrasted with the DFT values in fig. 5.12, which shows that our models are in very good agreement with the training data.

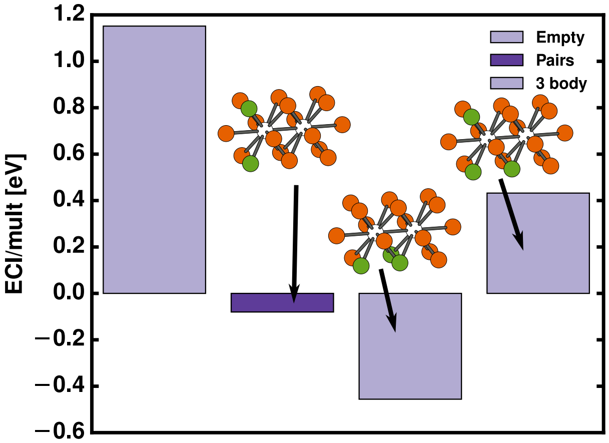

Figure 5.8: ECI values with their associated atom clusters for the Ni KRA local cluster expansion. The cluster of each ECI is highlighted in green.

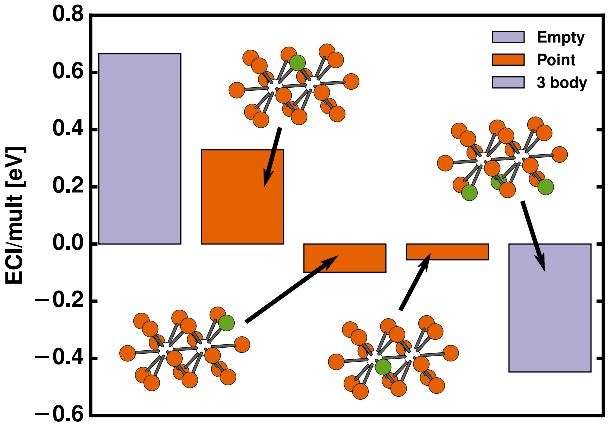

Figure 5.9: ECI values with their associated atom clusters for the Al KRA local cluster expansion The cluster of each ECI is highlighted in green.

An interesting result is that the KRA values of Al hops exhibit a linear dependence on the ACE composition in both Ni rich environments and in the $L1_2$ ordering. Figure 5.11 shows that Al KRA values have the same linear dependence on the local composition, but are uniformly lower in $L1_2$. The two linear trends for the KRA values of Al hops are captured by the local cluster expansion with one point and one triplet cluster. The linearity rises from the first point cluster shown in fig. 5.9, whose cluster function effectively describes the local composition in the ACE. To a lesser extent, there is a contribution from other point clusters, which describe the composition of shells at greater distances

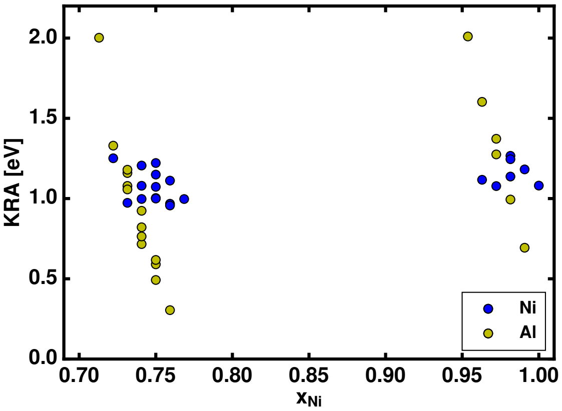

Figure 5.10: KRA values as a function of local Ni composition in the ACE for both Ni (left) and Al (right) vacancy exchanges. The values for both types of hops are colored to distinguish between hops that occur in pure Ni, and hops that occur in the $L1_2$ ordering.

from the hop cluster. These weaker point interactions capture the spread of the KRA so that they are not exactly linear with the ACE composition. Lastly, the triplet cluster captures the long range ordering of $L1_2$. Notice that the cluster highlighted in fig. 5.9 is clearly present in the local environment of a hop between local Ni sublattices in $L1_2$, as shown in fig. 5.14.

5.3.3 Effect of strain

An ordered intermetallic phase my experience strain when its embedded within matrix due to a lattice mismatch. Such might be the case for particles grown during a precipitation hardening process. We can gain some insight into the effect of strain of diffusional processes by calculating KRA values within a strained crystal. The lattice parameter used in our FCC Ni calculations is 3.52 Å, while that of $L1_2$ is 3.57 Å. For a selection of configurations calculated in the $L1_2$ ordering, we repeated the KRA calculation after straining the crystal such that its lattice parameter matched that of FCC Ni (1.4% strain). The results are shown in fig. 5.13, which reveals that the KRA values in

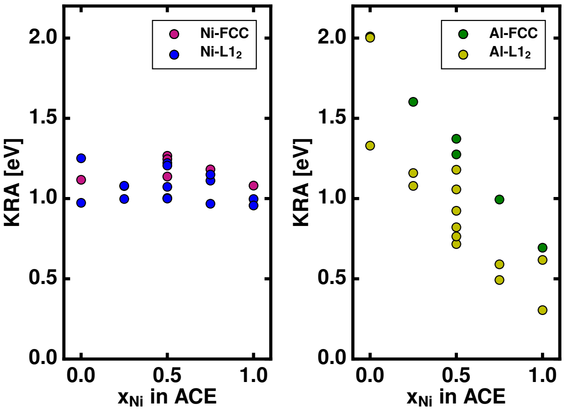

Figure 5.11: KRA values as a function of local Ni composition in the ACE for both Ni (left) and Al (right) vacancy exchanges. The values for both types of hops are colored to distinguish between hops that occur in pure Ni, and hops that occur in the L1$_2$ ordering.

the strained crystal are only slightly above those of the unstrained crystal. The difference in these energies shows that the local ordering plays a much more important role in the KRA values than strain.

5.4 Discussion

In the Ni-Al binary, diffusion occurs by two different mechanisms: a Ni atom can exchange with a nearest neighbor vacancy, or an Al atom exchanges with a nearest neighbor vacancy. The activation barrier for any event will be affected by interactions of the migrating atom with its local environment, with atoms near the migration path interacting more strongly than ones at a greater distance. Within the same local environment, a particular hop will have a different activation barrier depending on the direction the hop is occurring in. The concept of a KRA resolves the dependence on directionality, and depends only on the hop type (i.e. the types of atoms hoping and their arrangement within the hop cluster). Furthermore, it is a convenient quantity to cluster expand, since

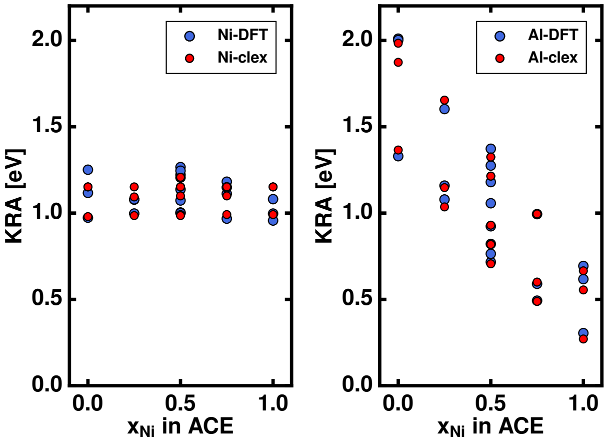

Figure 5.12: Comparison of DFT values for KRA with the cluster expansion predictions for both Ni (left) and Al (right).

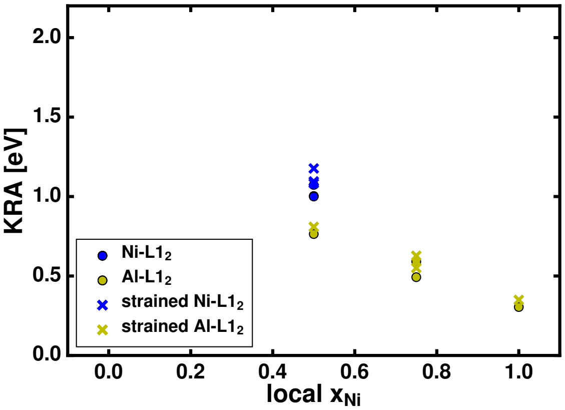

Figure 5.13: Comparison of KRA values for both Ni and Al in the L1_2 ordering under no strain, and a lattice parameter corresponding to FCC Ni.

it depends solely on ordering of a crystal.

We have systematically calculated KRA values for Ni and Al in both FCC Ni and the Ni_3Al L1_2 ordering. Atoms in the ACE are expected to interact more strongly with the migrating atom of the hop cluster. As the atom transitions into a neighboring vacant site, it must pass through the center of the ACE, resulting overcrowding where, in FCC, the migrating atom finds itself surrounded by 4 atoms, all of them at a length shorter than the equilibrium nearest neighbor distance. Our results show that a change in the composition of the ACE has the most pronounced influence on the KRA values. For Al, interactions with sites beyond the ACE are also important. The long range ordering of $L1_2$ changes the local composition beyond the ACE. While a change in the composition and ordering beyond the ACE does have an effect on the KRAs, it is less significant. In the case of $L1_2$, local orderings beyond the ACE do not change the qualitative dependence of Al hop KRAs on the ACE composition.

The values of fig. 5.11 reveal a striking difference between the behavior Ni and Al. Regardless of local environment or long range ordering, the KRA values of Ni appear to be approximately constant. This result suggests that for kinetic model in a Ni rich Ni-Al system, the KRA for Ni hops could be approximated as a constant value. Note that this does not imply a constant activation barrier ΔE. For Ni hops occurring between symmetrically equivalent end states, the KRA value would correspond exactly to the activation energy. In non-dilute alloys, the endstate will no always have the same energy, and ΔE will still have an environment dependence.

KRA values for Al behave completely differently than those of Ni. Their values are dependent on both the composition in the ACE, as well as the long range ordering of the crystal. For both the case of pure Ni FCC and the $L1_2$ ordering, KRA values appear to be proportional the number of Al atoms present in the ACE, with more Al raising the KRA value. Curiously, when the ACE is composed entirely of Ni, the KRA values of Al are lower that those of Ni. This suggests that Al is much more sensitive to interactions in the activated state, with local Al-Al interactions heavily influencing energetics of Al hops.

In the dilute limit, where the presence of Al atoms is low, we can expect Al to exchange with vacancies at a significantly higher rate than Ni atoms. The kinetics in the ordered $L1_2$ phase will be more heavily influenced by thermodynamic contributions, since the energies of the end states may vary significantly, depending on the cost of introducing antisite defects on the long range ordering. The preference for a particular sublattice by the vacancy in a long range ordered structure will also influence kinetics, since it will bias hops to particular local environments.

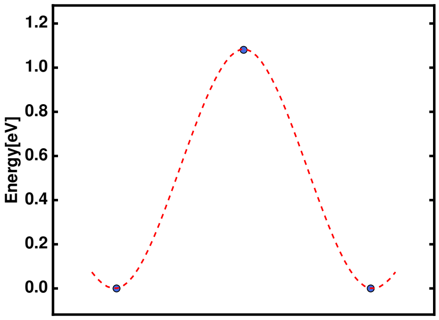

Figure 5.14: Example calculation for an Al hop between two equivalent endstates. The symmetry in the diffusion path makes it possible to determine the energy of the activated state with just one intermediate image.

We described in section 5.2.1 how to use the symmetry of the crystal and hop cluster to determine which local environments are symmetrically equivalent. The description is true in the general case, but there are some caveats when using methods such as DFT that involve supercells, where interactions with periodic images can arise. The chosen supercell should be large enough to minimize periodic image interactions of atoms participating in the hop, as well as atoms in the local environment. A subtlety of the supercell selection is that it may reduce symmetry, resulting in different KRA values for hops that are symmetrically equivalent in an infinite solid, but not in the chosen supercell.

It is therefore advantageous to select a supercell that retains the symmetry of the primitive cell. An obvious choice is to select supercells whose transformation matrix is a multiple of the identity matrix. However, this may not be the optimal choice, since a more cubic supercell with the same factor group may exist that better isolates the diffusion hop from periodic image interactions. For our system, we selected a reasonably large supercell of 108 atoms, that retained the cubic symmetry of FCC. The shape of the supercell was itself cubic, constructed as a $3 \times 3 \times 3$ arrangement of the FCC conventional cell. With this choice, the 12 nearest neighbor transitions mentioned earlier remain symmetrically equivalent in pure Ni. Figure 5.15 contrast how different supercell choices can break symmetry of equivalent hop clusters under periodic boundary conditions.

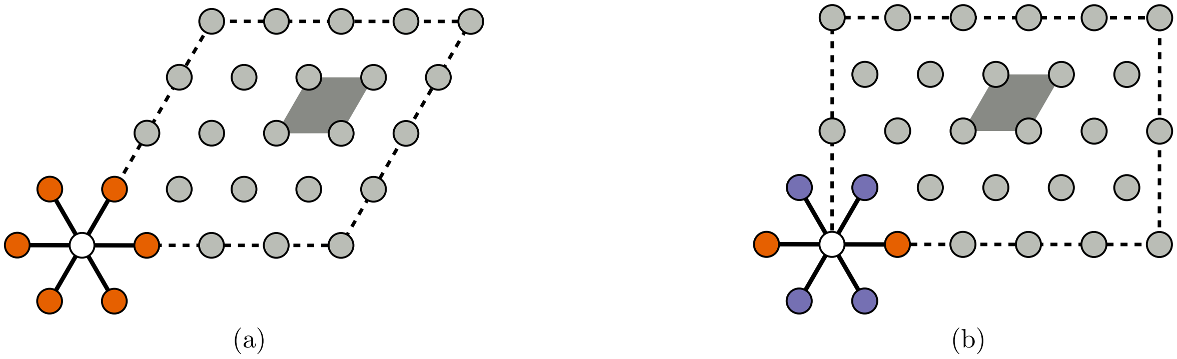
(a) (b)

Figure 5.15: Example of how a supercell may have less symmetry than the primitive cell. In fig. 5.15a, all operations in the primitive factor group exist in the supercell factor group, and all hop clusters remain equivalent. In fig. 5.15b, the supercell lacks rotational symmetry of the primitive cell, resulting in two distinct hops, highlighted in different colors.

5.5 Conclusion

We have outlined a systematic method to enumerate diffusion hop clusters within any crystal ordering. The local environment around these hop clusters can be perturbed to determine the KRA values under different conditions, which is critical to understand for non-dilute diffusion model. These methods were applied in the context of the Ni-Al system for the γ (pure Ni) and γ' phases ($L1_2$ ordering). We thoroughly investigated KRA values under different local environments for both Ni and Al vacancy exchanges. Results show that Ni-vacancy exchanges are largely independent of local environment and long range ordering, while Al-vacancy exchanges depend linearly on the immediate local environment, which high local Al concentrations resulting in the highest KRA values. Using local cluster expansions, models for both species were constructed that can accurately predict KRA values with just a handful of atomic interactions.

Chapter 6

Kinetic properties of Ni-Al

6.1 Introduction

Precipitation hardening is a major strengthening mechanism employed in the development of various engineering materials. The presence of precipitates of an ordered intermetallic phase within a matrix can greatly increase the strength of the material at high temperature. A common example of this is found in Ni-Al superalloys, designed to operate under high stress, high temperature conditions. These alloys gain their mechanical properties from the ordered $L1_2$ particles that grow within a Ni rich solid solution matrix.

The resulting precipitate size and density after the ageing process is determined by both thermodynamic and kinetic processes. Thermodynamics drives the formation of long range orderings, and determines the equilibrium volume fraction of the precipitates. The growth of these precipitates is governed by kinetics, which determines the density and size of the precipitates. Through a series of atomic hops, long range diffusion will redistribute the atoms in the crystal, with each individual hop being governed by its local ordering. Diffusion also plays a critical role in the operational lifetime of industrial materials. Throughout its operational lifetime, the desired microstructure can degrade, resulting in a loss of strength.

Diffusion in solids is mediated by vacancies in the crystal that exchange with neighboring atoms. As a result, successive jumps of each atom are correlated. In order of the jump to occur, diffusing atoms must overcome an activation barrier, which determines the frequency with which hops occur. These correlation effects and activation barriers ultimately determine the value of kinetic coefficients that describe the fluxes within a crystal. In the dilute limit of a binary alloy, the transport coefficients have been established for different crystal structures, such as the 5-frequency model for FCC. Other approaches include making a mean field approximation, where atomic diffusion depends on the local environment. In this work we combine cluster expansion methods with kinetic Monte Carlo simulations to model the atomistic behavior of Ni-Al.

6.2 Theoretical formalism

This section summarizes various phenomenological metrics of atomic mobility in substitutional alloys and describes how they can be calculated starting with an atomic description of hop frequencies. We make a distinction between perfect crystals, where the number of vacancies are conserved, and solids containing a sufficient number of vacancy sources and sinks to ensure local equilibrium in the vacancy concentration. The two extremes lead to different sets of diffusion coefficients.

6.2.1 The case of a perfect crystal of a binary substitutional alloy

We focus on the Ni rich fcc-based phases of the Ni-Al binary. These phases accommodate dilute concentrations of vacancies that can mediate substitutional diffusion. In an actual alloy, extended defects such as dislocations and grain boundaries act as sources and sinks for vacancies. In this section, we review metrics of substitutional diffusion in crystals where no such sources and sinks are present, and where the number of sites of the crystal, M, and the total number of vacancies, N_{Va}, is conserved. We will refer to these solids as “perfect crystals,” noting that, while they do not contain dislocations or grain boundaries, they still contain vacancies.

Imbalances in the chemical potentials of mobile species act as thermodynamic driving forces for atomic diffusion. These can be extracted from the Gibbs free energy, G, of the alloy, which is a function of the temperature, T, pressure, P, and the number of atoms N_{Ni} and N_{Al}. The free energy of a perfect crystal can be normalized by the number of sites in the crystal

$$g\left(T, P, x_{Ni}, x_{Al}\right) = \frac{G}{M} \tag{6.1}$$

where x_{Ni} and x_{Al} are the Ni and Al atom fractions relative to the number of sites in the crystal (such that $x_{Ni} + x_{Al} + x_{Va} = 1$).

In a perfect crystal diffusion is driven by gradients of “diffusion potentials”, defined as [127, 128, 24]

$$\tilde{\mu}_i = \frac{\partial g}{\partial x_i} = \mu_i - \mu_{Va} \tag{6.2}$$

The diffusion potential of a specie i is equal to the difference in the chemical potential of i, $\mu_i = \left(\frac{\mathrm{d}G}{\mathrm{d}N_i}\right)_{T,P,N_{j\neq i}}$, and the vacancy chemical potential, $\mu_{Va} = \left(\frac{\mathrm{d}G}{\mathrm{d}N_{Va}}\right)_{T,P,N_{j\neq Va}}$. Each $\tilde{\mu}_i$ can be viewed as the change in free energy of the alloy as an atom of type i is added to the solid at the expense of a vacancy (holding the number of crystal sites M constant).

Diffusion fluxes within a perfect crystal are related to the gradients of diffusion potentials according to

$$\begin{bmatrix} \vec{J}_{Ni} \\ \vec{J}_{Al} \end{bmatrix} = - \begin{bmatrix} L_{NiNi} & L_{NiAl} \\ L_{AlNi} & L_{AlAl} \end{bmatrix} \begin{bmatrix} \nabla \tilde{\mu}_{Ni} \\ \nabla \tilde{\mu}_{Al} \end{bmatrix} \tag{6.3}$$

where the L_{ij} refer to Onsager transport coefficients[127, 129]. Note that only the fluxes for Ni and Al need be accounted for. If the number of sites M is conserved, then $\vec{J}_{Va} + \vec{J}_{Ni} + \vec{J}_{Al} = 0$.

Kubo-Green linear response methods can be used to relate the phenomenological Onsager transport coefficients of eq. (6.3) to fluctuations that occur at the atomic scale in equilibrium. At finite temperature, atoms will be in continuous motion, migrating from one site to the next through atom-vacancy exchanges. For a crystalline solid,

$$L_{ij} = \frac{1}{\Omega k_B T} \tilde{L}_{ij} \tag{6.4}$$

with

$$\tilde{L}_{ij} = \frac{\langle \left(\sum_{\zeta} \Delta \vec{R}_i^{\zeta}(t) \right) \left(\sum_{\zeta} \Delta \vec{R}_j^{\zeta}(t) \right) \rangle}{(2d)tM} \tag{6.5}$$

Here, k_B is the Boltzmann constant, T is the temperature, Ω is the volume per substitutional site, M is the number of sites in the crystal, and d is the dimensionality of the substitutional network (e.g. for a 3-dimensional substitutional network $d = 3$, while a layered material would have $d = 2$). The vectors $\Delta \vec{R}_i^{\zeta}$ connect the end points of the trajectory of atom ζ being a species of type i after the elapse of a time t. The brackets $\langle \, \rangle$ denote ensemble averages at equilibrium. Note that eq. (6.5) satisfies the Onsager reciprocity relations[130], which require that $L_{ij} = L_{ji}$.

Other purely kinetic quantities can be defined in terms of the $\Delta\vec{R}_i^\zeta$, including correlation factors and tracer diffusion coefficients. The correlation factor f_i of a species i is defined as

$$f_i = \frac{\langle \Delta\vec{R}_i^2 \rangle}{N_\tau \langle \Delta\vec{r}_i^{\,2} \rangle} \tag{6.6}$$

where N_τ is equal to the number of hops and where $\Delta\vec{r}^2$ is the square of an elementary hop distance (e.g. nearest neighbor distance for nearest neighbor atom-vacancy exchanges). Correlation factors measure the degree with which correlations between successive hops affect atomic transport of individual atoms in a crystal. When an atom or vacancy performs a random walk, there are no correlations between successive hops and $f = 1$. When $f = 0$, every individual hop is exactly opposite the previous one. Tracer diffusion coefficients measure the diffusivity of tagged tracer atoms in the absence of chemical gradients and can be expressed as

$$D_i^* = \frac{\langle \Delta\vec{R}_i^2 \rangle}{2dt} \tag{6.7}$$

Gradients in chemical potential are not straightforward to measure experimentally. Flux expressions in terms of concentration gradients are more convenient, and can be derived from eq. (6.3) by chain rule differentiation of the chemical potentials. The flux expressions then take the form

$$\begin{bmatrix} \vec{J}_{Ni} \\ \vec{J}_{Al} \end{bmatrix} = - \begin{bmatrix} D_{Ni,Ni} & D_{Ni,Al} \\ D_{Al,Ni} & D_{Al,Al} \end{bmatrix} \begin{bmatrix} \nabla c_{Ni} \\ \nabla c_{Al} \end{bmatrix} \tag{6.8}$$

The matrix of diffusion coefficients, $\boldsymbol{D}$, are related to the Onsager transport coefficients according to

$$\begin{bmatrix} D_{Ni,Ni} & D_{Ni,Al} \\ D_{Al,Ni} & D_{Al,Al} \end{bmatrix} = \begin{bmatrix} \tilde{L}_{Ni,Ni} & \tilde{L}_{Ni,Al} \\ \tilde{L}_{Al,Ni} & \tilde{L}_{Al,Al} \end{bmatrix} \begin{bmatrix} \tilde{\Theta}_{Ni,Ni} & \tilde{\Theta}_{Ni,Al} \\ \tilde{\Theta}_{Al,Ni} & \tilde{\Theta}_{Al,Al} \end{bmatrix} \tag{6.9}$$

and is a product of a kinetic factor consisting of Onsager transport coefficients, $\tilde{\boldsymbol{L}}$, and a thermodynamic factor, $\tilde{\boldsymbol{\Theta}}$.

The thermodynamic factor $\tilde{\boldsymbol{\Theta}}$ is proportional to the Hessian of the free energy

$$\tilde{\boldsymbol{\Theta}} = \frac{1}{k_B T} \begin{bmatrix} \frac{\partial^2 g}{\partial x_{Ni} \partial x_{Ni}} & \frac{\partial^2 g}{\partial x_{Ni} \partial x_{Al}} \\ \frac{\partial^2 g}{\partial x_{Al} \partial x_{Ni}} & \frac{\partial^2 g}{\partial x_{Al} \partial x_{Al}} \end{bmatrix} \tag{6.10}$$

Similar to the Onsager transport coefficients, it is possible to relate the elements of the thermodynamic factor matrix to fluctuations, this time in composition within the semi Grand Canonical ensemble according to

$$\tilde{\Theta}_{ij}^{-1} = \frac{1}{M} \langle N_i N_j \rangle - \langle N_i \rangle \langle N_j \rangle \tag{6.11}$$

where the ensemble averages are performed in a crystal of M sites while holding the diffusion potentials $\tilde{\mu}_i$ constant.

Though $\boldsymbol{D}$ couples fluxes to gradients in concentration, the individual components of the matrix do not by themselves reveal much about the underlying physics of transport properties in a binary substitutional alloy where atomic hops are mediated by atom-vacancy exchanges. Key properties are embedded in the eigenvalues of $\boldsymbol{D}$. In the limit of a dilute vacancy concentration, the larger eigenvalue, λ^+, asymptotically converges to the vacancy diffusion coefficient, while the smaller eigenvalue, λ^-, becomes equal to an intermixing diffusion coefficient between Ni and Al. Additional metrics can be defined in terms of the elements of $\boldsymbol{D}$ that measure the extent with which the alloy deviates from a kinetically ideal substitutional alloy, which is defined as an alloy that is not only thermodynamically ideal, but also has the property that the components of the alloy have identical atom-vacancy exchange frequencies. One such metric is defined as [24]

$$\phi = \frac{D_{Al,Ni}}{D_{Ni,Al} + D_{Al,Ni}}, \tag{6.12}$$

and measures the fraction of Al that will exchange with a flux of vacancies. For a kinetically ideal substitutional alloy there is no bias in the atom-vacancy exchange frequency between the different components and ϕ becomes equal to the alloy concentration. Any deviation from this value reveals a difference in the relative mobilities between the two components of the alloy. Another metric, defined as [24]

$$\delta = D_{Al,Al} - D_{Ni,Ni} + D_{Ni,Al} - D_{Al,Ni} \tag{6.13}$$

measures the degree with which a gradient between the Ni and Al concentrations, in the absence of a gradient in the vacancy concentration, induces a vacancy flux. δ reflects the alloy's susceptibility to the Kirkendall effect.

6.2.2 Vacancies at local equilibrium

Other diffusion metrics exist when there are sufficient vacancy sources and sinks to regulate an equilibrium vacancy concentration at each point within the alloy. When there are sufficient vacancy sources and sinks to maintain local equilibrium with respect to the vacancy concentration, the vacancy chemical potential μ_{Va} will be equal to zero throughout the solid, thereby imposing thermodynamic constraints on the chemical potentials of Ni and Al. This is a common assumption in analyses of substitutional diffusion and was first invoked by Darken[131]. Under this approximation, the flux expressions can be expressed as

$$\vec{J}_{Ni} = -D_{Ni}\nabla c_{Ni} \tag{6.14}$$

$$\vec{J}_{Al} = -D_{Al}\nabla c_{Al} \tag{6.15}$$

where the self diffusion coefficients D_i are again a product of a kinetic and thermodynamic factor

$$D_{Ni} = \Lambda_{Ni}\Gamma \tag{6.16}$$

$$D_{Al} = \Lambda_{Al}\Gamma \tag{6.17}$$

The kinetic factor for each species are related to the Onsager transport coefficients according to

$$\Lambda_{Ni} = \left(\frac{\tilde{L}_{Ni,Ni}}{x_{Ni}} - \frac{\tilde{L}_{Ni,Al}}{x_{Al}}\right) \tag{6.18}$$

$$\Lambda_{Al} = \left(\frac{\tilde{L}_{Al,Al}}{x_{Al}} - \frac{\tilde{L}_{Al,Ni}}{x_{Ni}}\right) \tag{6.19}$$

The thermodynamic factors are the same for both species in the limit of a dilute vacancy concentration

$$\begin{aligned}\Gamma =& \frac{x_{Ni}}{k_B T}\left(\frac{\mathrm{d}\mu_{Ni}}{\mathrm{d}x_{Ni}}\right)_{\mu_{Va}=0} \\ =& \frac{x_{Al}}{k_B T}\left(\frac{\mathrm{d}\mu_{Al}}{\mathrm{d}x_{Al}}\right)_{\mu_{Va}=0}\end{aligned} \tag{6.20}$$

If correlations between diffusing atoms can be neglected, then the self diffusion coefficients can be expressed in terms of tracer coefficients and the thermodynamic factor according to

$$D_{Ni}^{Darken} = D_{Ni}^{*}\Gamma \tag{6.21}$$

$$D_{Al}^{Darken} = D_{Al}^{*}\Gamma \tag{6.22}$$

The fluxes of eq. (6.14) and eq. (6.15) are relative to the crystal frame of reference. However, in the presence of vacancy sources and sinks, such as dislocations and grain boundaries, the solid can become susceptible to the Kirkendall effect and single crystal regions may move relative to a fixed laboratory frame of reference. Interdiffusion between the two components of the alloy is usually measured in the laboratory frame of reference. The interdiffusion coefficient in the laboratory frame of reference can be expressed as

$$\tilde{D} = \tilde{\Lambda}\Gamma \tag{6.23}$$

where

$$\tilde{\Lambda} = x_{Al}\Lambda_{Ni} + x_{Ni}\Lambda_{Al} \tag{6.24}$$

6.2.3 Atomistic description

Even in thermodynamic equilibrium, atoms of a substitutional alloy continuously exchange with a dilute concentration of vacancies and thereby wander throughout the crystal. The Kubo-Green expression of eq. (6.5) shows that the phenomenological transport coefficients can be calculated by tracking the trajectories $\Delta\vec{R}_i^{\zeta}$ of these mobile atoms. The trajectories $\Delta\vec{R}_i^{\zeta}$ are the result of many individual atom-vacancy exchanges that occur stochastically with frequencies that in a crystal can be approximated with transition state theory according to

$$\Gamma = v^{*} \exp\left(\frac{-\Delta E}{k_B T}\right). \tag{6.25}$$

Here ΔE is the migration barrier for a hop and v^{*} is a vibrational prefactor. Within the harmonic approximation, the vibrational prefactor v^{*} is equal to the ratio of the products of the normal mode frequencies in the activated and initial states

$$v^{*} = \frac{\prod_{i=1}^{3N-3} v_i}{\prod_{k=1}^{3N-4} \tilde{v}_k} \tag{6.26}$$

where v and $\tilde{v}$ are the initial and activated state frequencies respectively and where N is the number of atoms in the crystal.

Non dilute alloys exhibit varying degrees of short and long-range ordering as a function temperature and alloy composition. As atoms of an alloy migrate, they encounter a range of migration barriers due to fluctuations in the local degree of ordering along their trajectory. Modeling diffusion in concentrated substitutional alloys therefore requires an accurate description of the dependence of the energies of the end states and of the activated states on the local degree of short- and long-range order.

In this work, we use cluster expansion Hamiltonians to describe the dependence of the energy of the crystal on the particular arrangement of Ni, Al and vacancies over the sites of the FCC crystal. The energies of the end states of a hop in a Ni-Al alloy can be described with a ternary cluster expansion as each site of the crystal is either occupied by Ni, Al or a vacancy. For the Ni-rich alloy, it is convenient to assign two occupation variables to each crystal site i: p_i^{Al}, which is equal to 1 if the site is occupied by Al and zero otherwise and p_i^{Va}, which is 1 if the site is occupied by a vacancy and zero otherwise. The configurational state of a crystal of M sites is then uniquely determined by specifying the occupation variables at each site, $\vec{p} = \left(p_1^{Al}, p_1^{Va}, ..., p_i^{Al}, p_i^{Va}, ..., p_M^{Al}, p_M^{Va}\right)$. The energy of the crystal in any end state of a hop can be expressed as an expansion of polynomials of the occupation variables

$$E(\vec{p}) = V_0 + \sum_{\alpha,\pi} V_{\alpha}^{\pi} \prod_{i\in\alpha} p_i^{\pi_i} \tag{6.27}$$

where α refers to clusters of sites such as point, pair, triplet etc. clusters and where the π denotes which occupation variable is to be assigned to each site in the cluster α. The V_{α}^{π} are constant expansion coefficients referred to as effective cluster interactions (ECI). The ECI of a cluster expansion Hamiltonian can be parameterized by training to a large number of energies for different alloy configurations $\vec{p}$ that have been calculated with a first principles electronic structure method such as density functional theory.

The migration barrier for a particular hop is equal to the difference in energy between the activated state and the initial state of the hop. In FCC Ni-Al, there are two important hop types: a nearest neighbor Al-Va exchange and a nearest neighbor Ni-Va exchange. The migration barrier for each hop type in a concentrated alloy depends on the local degree of ordering surrounding the sites involved in the hop. We denote this ordering as $\vec{p}\backslash H$, which collects all the occupation variables of the crystal minus those residing on the hop cluster H. Migration barriers also depend on the direction of the hop, since the end states of most hops in a concentrated alloy will not have the same energy. It is, therefore, convenient to work with a kinetically resolved activation barrier (KRA), ΔE^{KRA}, which for pair exchanges of type t (either an Al-Va exchange or a Na-Va exchange) is defined as the average between the forward and backward hop. ΔE^{KRA} is thereby independent of the direction of the hop. Nevertheless, in a concentrated alloy its value still depends on the degree ordering surrounding the hop, i.e. ${}_t\Delta E^{KRA}$. As with the energies of the end states of a hop, the dependence of ${}_t\Delta E^{KRA}$ on $\vec{p} \setminus H$ can also be described with a (local) cluster expansion

$$ {}_t\Delta E^{KRA}(\vec{p} \setminus H) = {}_tV_0^{KRA} + \sum_{\alpha,\pi} {}_tV^{KRA}{}^{\pi}_{\alpha} \prod_{i\in\alpha} p_i^{\pi_i} \tag{6.28} $$

where the sum extends over clusters not including the hop cluster H. The expansion coefficients ${}_tV^{KRA}{}^{\pi}_{\alpha}$ can be determined by training to a large set of ${}_t\Delta E^{KRA}(\vec{p} \setminus H)$ values as calculated with a first-principles method. Each hop type t will have a separate cluster expansion. Once cluster expansions for the end states of the hop (eq. (6.27)) and for each of the hop types t have been parameterized using a first-principles method, it is possible to calculate the migration barrier for any local environment according to

$$ \Delta E = E^* - E_i = {}_t\Delta E^{KRA}(\vec{p} \setminus H) + \frac{E(\vec{p}_f) - E(\vec{p}_i)}{2} \tag{6.29} $$

where $\vec{p}_f$ and $\vec{p}_i$ are the configurations of the crystal in the final and initial states, and where $\vec{p} \setminus H$ is the configuration of the crystal minus the hop cluster sites (which remains unchanged during the hop).

The various cluster expansions make it possible to calculate all the thermodynamic and kinetic quantities that are necessary to determine the different diffusion coefficients described in section 6.2. Grand Canonical Monte Carlo simulations applied to the crystal cluster expansion Hamiltonian eq. (6.27) generate the necessary thermodynamic information to construct an equilibrium temperature versus composition phase diagram, to calculate the equilibrium vacancy concentration and to calculate the elements of the thermodynamic factor matrix of eq. (6.10). The combination of the crystal cluster expansion eq. (6.27) with the local cluster expansions for the KRAs, eq. (6.28) as in eq. (6.29) makes it possible to determine the migration barrier in any alloy environment. This makes it possible to sample atomic trajectories that arise from stochastic atom-vacancy exchanges with kinetic Monte Carlo simulations.

6.3 Computational details

Determining the activation barrier ΔE of a diffusive hop requires an efficient evaluation of the endstate energies E_i and E_f, as well as the KRA value ΔE^{KRA}. In order to calculate the endstate energies, we constructed a ternary cluster expansion for FCC Ni-Al-Va. We used a recursive approach[2] to parameterize the expansion coefficients, starting with a well optimized binary Ni-Al cluster expansion[1], which we extended to account for interactions between Al and vacancies. In order to account for vacancy interactions, we fit to 50 configurations containing a vacancy within a 107 atom supercell, resulting in a root mean square value of approximately 6meV. The orderings of these configurations were either pure Ni or an $L1_2$ superstructure, perturbed with point, pair, or triplet defects. We assume a dilute vacancy concentration, and did not parameterize any interactions where vacancies interact with each other.

We also used two local cluster expansions to describe the dependence of the Ni-vacancy and Al-vacancy exchange KRAs. Each of the local cluster expansions were fit to 22 KRA values, with local perturbations within pure Ni and $L1_2$ 107 atom supercells. Details of the construction of these local cluster expansions are reported in chapter 5. A comparison between the DFT KRA calculations and the predicted values from the local cluster expansions can be seen in fig. 6.1. The local cluster expansions faithfully reproduce the different KRA trends for Ni vs Al: while KRA values for Ni hops are approximately constant for all local orderings, Al KRA values are sensitive to the Al composition in their immediate environment.

Vibrational prefactors defined in eq. (6.26) were calculated by calculating vibrational frequencies of Ni and Al within a 31 atom Ni supercell. Supercells with either Ni or

Al in both the equilibrium and activated state were first completely relaxed so that the atoms were in the equilibrium positions. We then used VASP to calculate the vibrational frequencies for both the equilibrium and activated states, corresponding to the values of the numerator and denominator of eq. (6.26). We found that $v^*_{Ni} = 3.11\,\mathrm{THz}$, and $v^*_{Ni} = 4.39\,\mathrm{THz}$.

Using semi Grand Canonical Monte Carlo simulations, we calculated the Ni rich binary phase diagram. We determined the equilibrium vacancy concentration in the Ni rich phases by setting $\mu_{Va} = 0$. We also tracked the fluctuations in composition during the simulation, which are directly related to the thermodynamic factor by eq. (6.11).

We employed Kinetic Monte Carlo techniques to calculate the Onsager transport coefficients. The process involves selecting a series hop events within a simulation cell, updating the atom positions and clock as each event is applied to the configuration. The dimensions of our simulation cell were $10 \times 10 \times 10$ conventional FCC cells (4000 atoms) and contained a single vacancy. When vacancies are dilute, the Onsager coefficients scale linearly with the vacancy concentration, and we adjusted their values accordingly, using the equilibrium vacancy concentrations from our Grand Canonical simulations.

6.4 Results

6.4.1 Thermodynamic quantities

Using Grand Canonical Monte Carlo simulations, we calculated the phase diagram of the Ni-Al binary, as well as the equilibrium vacancy concentration at 1300K for the γ and γ' phases. A section of the phase diagram can be seen in fig. 6.3a. The shaded ares represent single phase regions, and define the composition ranges where we did our KMC calculations. In the Grand Canonical ensemble, the diffusion potentials $\tilde{\mu}_{Ni}$ and

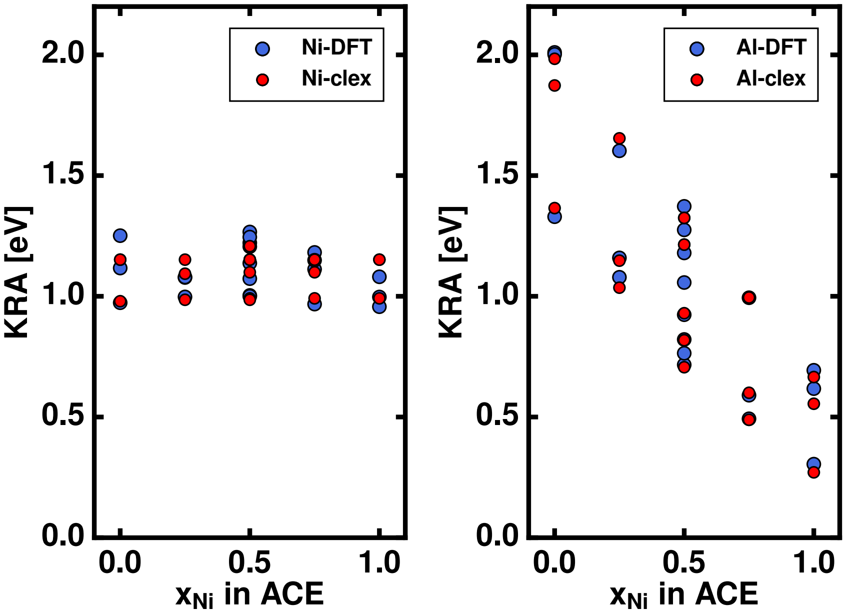

Figure 6.1: Comparison of DFT values for KRA with the cluster expansion predictions for both Ni (left) and Al (right). While KRA values for Ni are approximately constant independent of local ordering, KRA values for Al scale linearly with the immediate Al concentration of neighboring atoms.

$\tilde{\mu}_{Al}$, and the number of crystal sites M are controlled. In a real system, imperfections in the crystal (e.g. dislocations and grain boundaries) act as sources and sinks of vacancies. The equilibrium vacancy concentration in a crystal therefore cannot be controlled experimentally and is instead regulated by these imperfections. We modelled this behavior by setting the vacancy chemical potential $\mu_{Va} = 0$ throughout our calculations, which will cause the system to choose the vacancy concentration that minimizes its Gibbs free energy. The results of our calculations can be seen in fig. 6.3b. The value of the vacancy composition will have an important impact on the values of diffusion coefficients, since in the dilute limit, kinetic coefficients are proportional to the number of vacancies in the crystal.

In the γ phase, the vacancy concentration (x_{Va}) begins around $10^{-5.5}$ at $x_{Ni} = 1$. As the Al concentration is increased, favorable nearest neighbor interactions between Al and vacancies result in an increase of the vacancy concentration. In the γ' phase there is a pronounced valley in the vacancy concentration at $x_{Ni} = 0.75$, corresponding to the composition of a perfect L1_2 ordering. Introducing vacancy defects comes at a higher energetic cost within a perfectly long range ordered crystal than in one with higher disorder. When the composition moves away from $x_{Ni} = 0.75$, the crystal is forced to accommodate antisite defects, increasing the amount of disorder, resulting in more vacancies.

Both the γ and γ' phases have an FCC structure. By tracking the local composition of nearest neighbor shells around the vacancy, it is possible to infer the local environments of the vacancies. Figures 6.2a and 6.2b show the nearest neighbor environment of the Ni and Al sublattice sites of the L1_2 ordering, while fig. 6.2c shows the distance from a particular site in FCC from its first, second, and third nearest neighbors. These two figures are useful for interpreting the values of fig. 6.3c, which shows the composition of atomic shells at these three neighbor distances.

In the γ phase, Ni and Al form a solid solution, resulting in a random distribution of Al on the Ni FCC lattice. At longer length scales, pair interactions between vacancies and Al atoms are not significant. However, our DFT calculations show that positioning an Al atom in the nearest neighbor shell of a vacant site is energetically favorable, while the converse is true for the second nearest neighbor shell. We can see this behavior in fig. 6.3c, which shows that at high Ni compositions (γ phase), the Al composition of the nearest neighbor shell around vacancies (orange) is higher than that the global composition (dashed line). This indicates that the Al atoms favor occupying these vacancy nearest neighbor positions, while the opposite is true for the second nearest neighbor shell (purple). For the third nearest neighbor, the pair interaction is long enough that the energy contribution dies out. The chances of occupying this shell therefore match the rest of the crystal sites, and the average composition of the third nearest neighbor shell closely tracks the global composition.

For the γ' phase (L1$_2$), the Al ordering introduces more complex environments for the vacancy to occupy. Our cluster expansion predicts that in the perfect long range ordering, it is energetically favorable to create a vacancy defect on one of the Ni sublattices over the Al sublattice. When the vacancy is on the Al sublattice (fig. 6.2b), the nearest neighbor and third nearest neighbor shells are completely occupied by Ni atoms, while the second nearest neighbor shell is completely made up of Al atoms. On the other hand, when the vacancy is on the Ni sublattice (fig. 6.2a), the nearest neighbor and third nearest neighbor shells are $\frac{2}{3}$ Ni, while the second nearest neighbor shell is entirely Ni.

At stoichiometric compositions, fig. 6.3c shows that the vacancy prefers the Ni sublattices over the Al sublattice almost exclusively, since the local compositions in each shell matches that of fig. 6.2a. In an excess of Ni, a moderate deviation from the stoichiometric values can be seen. The Ni excess is achieved by creating Ni antisite defects on the Al sublattice. If the vacancy were to remain exclusively on the Ni sublattices, we would therefore expect the second nearest neighbor compositions to remain entirely Ni, while the first and third nearest neighbor Al compositions decrease. Instead, fig. 6.3c shows that the second nearest neighbor Al composition increases somewhat, suggesting that the vacancy begins to occupy the Al sublattice more often. In an excess of Al, the trends have similar behavior, indicating that creating Al antisite defects also biases the vacancy to occupy the Al sublattice of the L1$_2$ ordering.

6.4.2 Kinetic observations

The kinetic Onsager coefficient couple chemical potentials gradients to fluxes of different species. In the dilute limit, these coefficients scale linearly with the number of vacancies. The values are shown in fig. 6.4a. In the γ' composition region, both $L_{Ni,Ni}$ and $L_{Al,Al}$ experience a dip at $x_{Ni} = 0.75$, due to a decrease in the equilibrium va-

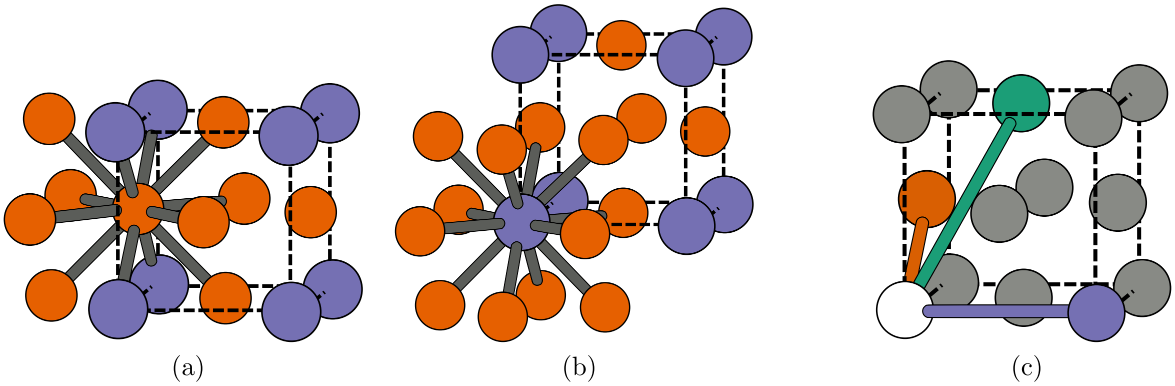
(a) (b) (c)

Figure 6.2: Figures 6.2a and 6.2b show the nearest neighbor environments of the $L1_2$ sublattices. Ni atoms (orange) are surrounded by 8 Ni, and 4 Al nearest neighbors, while Al atoms (purple) are surrounded by 12 Ni nearest neighbors. Figure 6.2c shows distances for first nearest neighbor (orange), second nearest neighbor (green) and third nearest neighbor (purple) distance within an FCC unit cell.

cancy concentration. The cross term $L_{Ni,Al}$ becomes negative around $x_{Ni} = 0.78$ (hollow circles), with negative values in the Al rich side of the γ' phase region.

Figure 6.4b shows values for the tracer diffusion coefficients of both Ni and Al, which tracks the mobilities of individual atoms in the crystal. The same dips due to a lowered vacancy concentration at $x_{Ni} = 0.75$ manifest themselves here. In the γ phase, Al is the more mobile species, while in γ' Ni tracers diffuse faster. The γ phase has no long range order, and fig. 6.1 shows that for Ni rich local environments around a hop, Al will, on average, have a lower activation barrier than Ni. A lower activation barrier corresponds to a higher hop frequency, resulting in faster diffusion for Al.

In the γ' phase, the relative values of tracer diffusion coefficients are reversed, with Ni being the faster diffuser. The long range ordering of $L1_2$ penalizes exchanges that require the introduction of Al antisite defects. In a perfect $L1_2$ ordering, an Al hop into a neighboring site is impossible without creating an antisite defect. On the other hand, sites on the Ni sublattice have other neighboring Ni sites, so the vacancy can move through the Ni channels without introducing defects into the long range ordering.

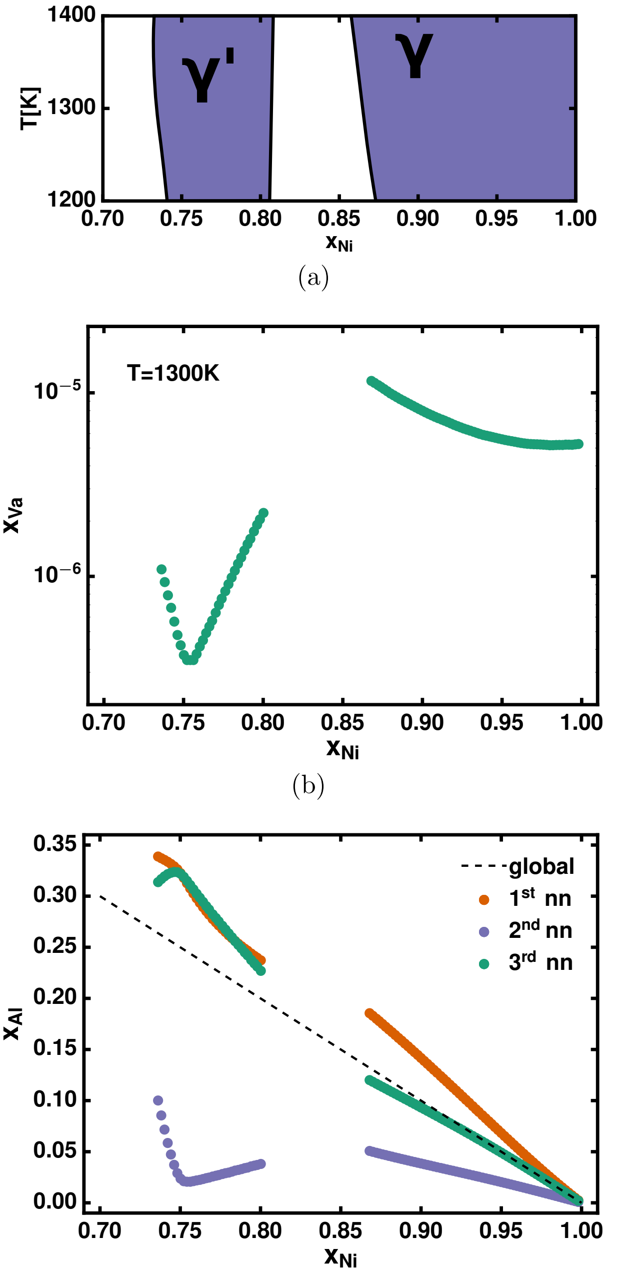

(a)

(b)

(c)

Figure 6.3: Thermodynamic properties of the γ and γ' phases calculated at 1300K. Equilibrium phase boundaries are shown in fig. 6.3a, while equilibrium vacancy concentrations are shown in fig. 6.3b. The local compositions around vacant sites are shown in fig. 6.3c for the nearest neighbor (nn), second nearest neighbor (nnn), and third nearest neighbor (nnnn) shells. The global concentration is shown with a dashed line.

The same behavior can be interpreted from the correlation factors in fig. 6.4c. In pure Ni, we see that the correlation factor for Ni is consistent with the expected value of a pure FCC crystal (≈ 0.78)), and that the vacancy correlation factor approaches 1, indicating the vacancies act as a completely random walker. As the Al composition is increased in the γ phase, the vacancy correlation factor very quickly decreases, approaching the very low values of the Al correlation factor. This suggests that when a vacancy gets at a nearest neighbor distance from an Al atom, it becomes "trapped", exchanging numerous times before an unlikely exchange with a Ni atom takes place, allowing the vacancy to continue its path through the crystal. These entrapments by Al become increasingly likely as the global Al composition increases, further correlating the paths taken by Al and vacancies.

In the γ' phase, there is a peak in the vacancy correlation factor of vacancies at stoichiometric compositions of $L1_2$. An increase in the correlation factor indicates that the hops taken by the vacancy have become more random. Vacancies must therefore be exchanging more frequently within the Ni sublattice sites, which are all symmetrically equivalent.

6.4.3 Projected diffusion metrics

Rather than examining the values of elements in the diffusion matrix $\boldsymbol{D}$, we will look at its characteristic values λ^+ and λ^-, and the values ϕ and δ defined in eqs. (6.12) and (6.13). Throughout our KMC simulations, we used cluster expansions to determine the hop frequencies of each hop, which depend on the short and long range ordering of the crystal. As such, we have not assumed an ideal solution at any moment, and all thermodynamic and kinetic contributions are contained in $\boldsymbol{D}$.

There are two Eigenvalues we can extract from $\boldsymbol{D}$. The larger Eigenvalue λ^+ is a

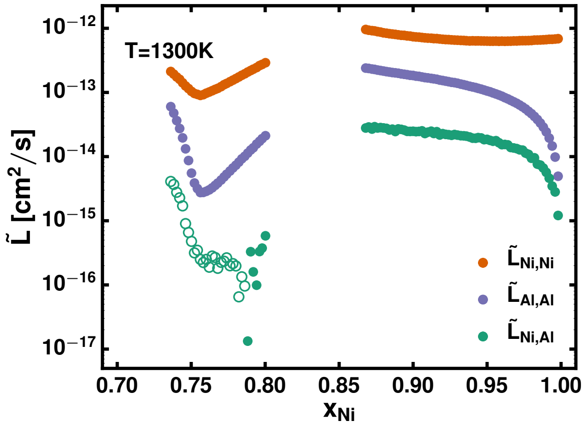

(a)

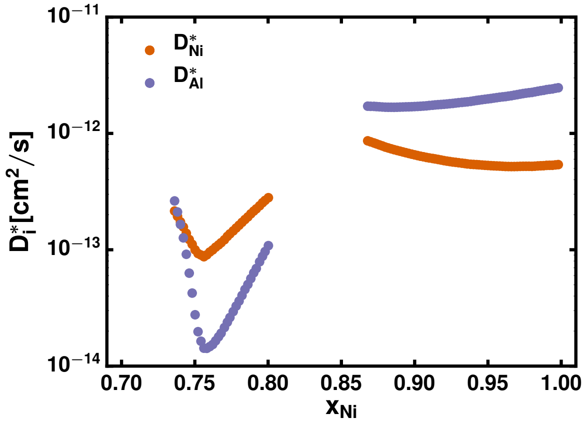

(b)

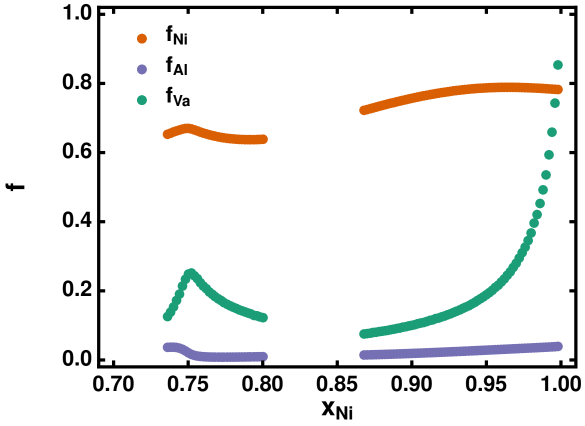

(c)

Figure 6.4: Onsager coefficients as defined in eq. (6.3) (fig. 6.4a), tracer diffusion coefficients (fig. 6.4b), and correlation factors (fig. 6.4c) from KMC simulations run at 1300K. At higher Al concentrations, the off diagonal $\tilde{L}_{Ni,Al}$ in fig. 6.4a becomes negative. Hollow points represent data where the absolute value of a negative property was taken.

metric for how vacancies dissipate due to a gradient in vacancy concentrations. In the limit of dilute vacancies, this value is the same as the tracer diffusion coefficient. The values of λ^+ and D^*_{Va} matches almost exactly in our calculations, and are shown in fig. 6.5a.

The smaller Eigenvalue λ^- corresponds to an intermixing mode between Ni and Al. For a hypothetical composition profile with a gradient in Ni and Al that resulted in no net vacancy flux, λ^- expresses the rate at which Ni and Al atoms would intermix. It is similar to the interdiffusion coefficient $\tilde{D}$, and exactly matches its value in the limit of an ideal solution. The similarities are displayed in fig. 6.5b. When $x_{Ni} = 1$, the values are identical, and in the γ phase their values are quite similar. It is only in the γ' phase that they significantly differ, due to the long range ordering of $\mathrm{L1_2}$, which lends itself poorly to an ideal solution approximation.

The value of ϕ tracks the bias of a vacancy flux to exchange with Al rather than with Ni. In the case of an ideal solution and kinetically ideal alloy, the value would simply be the atomic fraction of Al in the crystal. In the absence of ordering and identical hop frequencies, the probability of exchanging with Al is simply proportional to the amount of Al atoms present. The values from our calculations are shown in fig. 6.6a. In the γ phase, ϕ is positive, indicating a preference for vacancies to exchange with Al atoms, and increases as more Al is introduced. The opposite is true in the γ' phase, and vacancies prefer exchanging with Ni atoms, especially near stoichiometric compositions of $\mathrm{L1_2}$.

δ is akin to a "Kirkendall coefficient", and couples a vacancy flux induced by intermixing of Ni and Al, in the absence of a vacancy flux driving force. In a kinetically and thermodynamically ideal alloy $\delta = 0$, and intermixing induces no vacancy flux. The values in fig. 6.6b show that in the γ phase, intermixing of Ni and Al causes a net vacancy flux in the "positive" direction (counter to $\vec{J}_{Al}$). Since Al is the faster diffuser, more vacancies will exchange with Al and travel in the opposite direction. Within the γ'

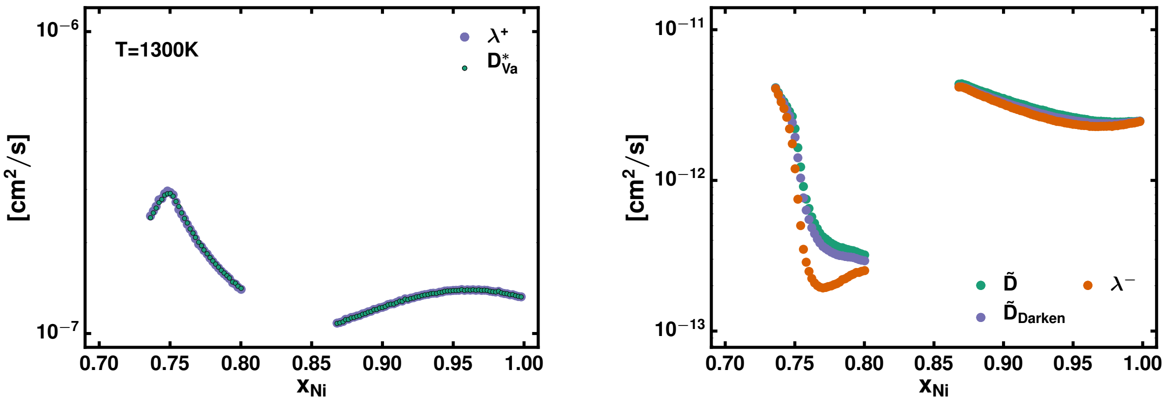

(a) (b)

Figure 6.5: Comparison of the large eigenvalue with the vacancy tracer diffusion coefficient (fig. 6.5a), and the smaller eigenvalue with the interdiffusion coefficient. Calculations were done at 1300K.

phase, we see that an excess of Ni causes the opposite behavior, and intermixing causes a vacancy flux counter to Ni. In an excess of Al, δ becomes positive again. The steep increase as Al composition grows is consistent with the values of the tracer diffusion coefficients in fig. 6.4b, which show that Al becomes increasingly mobile as Al is introduced into the $L1_2$ ordering, even surpassing the mobility of Ni.

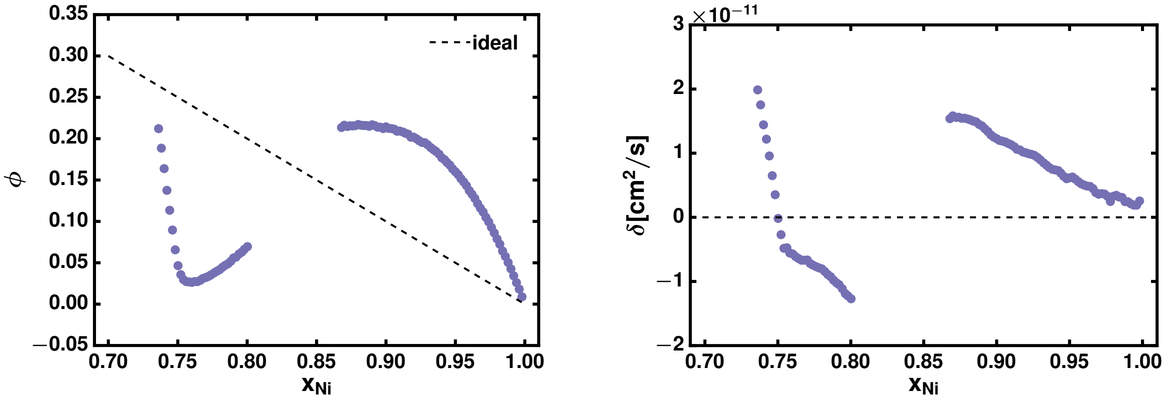

(a) (b)

Figure 6.6: Values of ϕ (fig. 6.6a) and δ (fig. 6.6b) at 1300K. Dashed lines indicate the expected values for a kinetically ideal solution.

6.4.4 Combining thermodynamic and kinetic contributions

There are two contributions to the self diffusion coefficients for Ni and Al: a thermodynamic contribution Γ, and a kinetic contribution Λ. The thermodynamic contribution is plotted in $fig.\ 6.7a$, and has a very noticeable spike around stoichiometric compositions for $L1_2$. The kinetic contribution is similar to the tracer diffusion coefficients; both are superimposed in fig. 6.7b. The difference between these two values is that the tracer diffusion coefficient accounts only for the path traveled by a particular atom, and ignores any correlation it might have with the trajectories of other atoms in the crystal.

The discrepancy in values of fig. 6.7b show that, for the most part, the trajectories of atoms are not significantly correlated. The exception to this is diffusion of Ni at low Al compositions. The deviation of Λ_{Ni} from D^*_{Ni} is likely due to the $L_{Ni,Al}$ term of eq. (6.18). Even though the value of $\tilde{L}_{Ni,Ni}$ decreases with x_{Ni}, its negative contribution to Λ_{Ni} will get amplified if it doesn't decay as quickly as x_{Al}.

Figure 6.7c shows the product of the values in fig. 6.7a and fig. 6.4b. Just as the tracer diffusion coefficients, Al is the faster diffuser in the solid solution, while Ni is more mobile in the $L1_2$ ordering. The thermodynamic contribution causes the Ni self diffusion coefficient to increase as the composition reaches $x_{Ni} = 0.75$, while the Al diffusivity remains at its lowest close to that composition. The Darken approximation, where correlations between different atoms are ignored, is quite accurate for self diffusion, save for the discrepancy at higher Ni compositions. Any error in the approximation arises purely from the difference between the kinetic contribution Λ and the corresponding tracer diffusion coefficients.

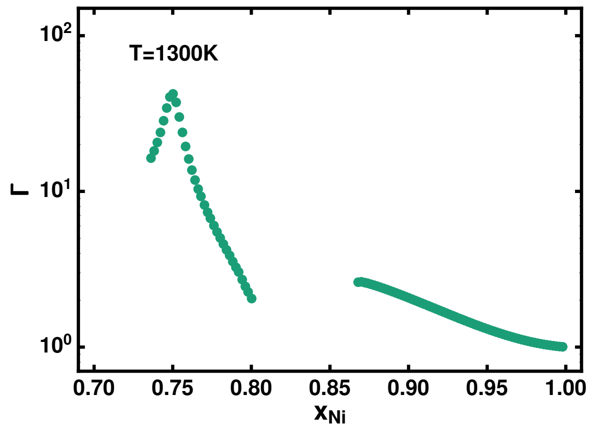

(a)

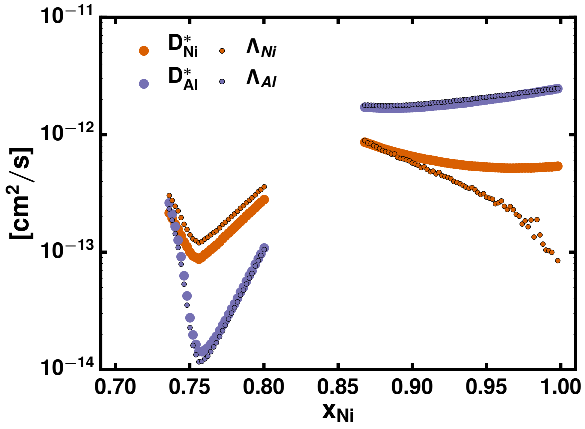

(b)

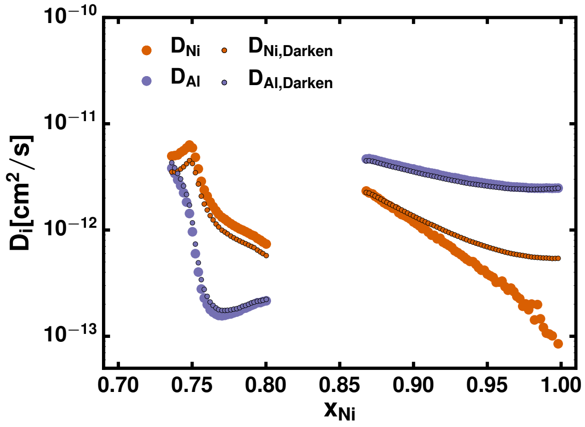

(c)

Figure 6.7: Thermodynamic contributions to the kinetic coefficients Γ (fig. 6.7a), comparison of kinetic contributions Λ with tracer diffusion (fig. 6.7b), and they're combination into self diffusion coefficients (fig. 6.7c). All values were calculated at 1300K.

6.5 Discussion

We have calculated various diffusion metrics in the Ni-Al binary for the FCC γ and γ' phases. Our results show that in the γ phase, Al is the faster diffuser, while Ni is more mobile in the long range ordered γ' phase.

The higher diffusion of Al in the γ phase can be understood almost entirely from the relative KRA values of Ni and Al. When the Ni composition is high, vacancy-Al hops will mostly encounter local environments with low local Al compositions. This results in lower KRA values for Al than for Ni, which in turn will correspond to lower activation barriers. The low activation barriers result in a higher exchange of vacancies with Al, and the Al atoms diffuse faster.

Local ordering in the solid solution heavily impacts the mobility of the vacancies. At dilute Al concentrations, vacancies favor having Al atoms as a first nearest neighbor. As a result, the diffusion of vacancies and Al is highly correlated, and both travel through the crystal together, favoring hops that keep them at a nearest neighbor distance.

In the γ' phase, vacancies are moving through a long range ordering, and diffusion in this phase is governed a lot more strongly by thermodynamics. Within the $L1_2$ ordering, vacancies primarily occupy the Ni sublattices, due to the higher energetic cost required to introduce a vacancy on the Al sublattice. The preference to occupy the Ni sublattices if further intensified by the possible hops from this position. Sites on the Ni sublattice have both Al and Ni atoms as nearest neighbor, so the vacancy can potentially exchange with either. However, while an exchange with a neighboring Ni effectively leaves the crystal in the same energetic state, an exchange with an Al both places the vacancy on the unfavored sublattice, while simultaneously creating an Al antisite defect. Al-vacancy exchanges in the $gamma'$ phase therefore occur infrequently, especially at stoichiometric $L1_2$ compositions. Under these conditions, the Al sublattice is “frozen”, and movements within the Ni channels are much more likely. A bias towards remaining on the Ni sublattices implies further exchanges with Ni atoms, and explains why the relative diffusivities of Ni and Al are opposite within the γ and γ' phases, as well as the trends of ϕ and δ.

6.6 Conclusion

We performed Kinetic Monte Carlo calculations in the Ni rich phases of Ni-Al to get diffusion coefficients for γ and γ'. In order to account for long and short range ordering of the alloy, we used a cluster expansion to dictate the energetics of the crystal orderings. Furthermore, we applied local cluster expansions to determine the value of the activation barriers of at each step of the simulation, such that its value depends on the local environment around the hop. Our results show that in the γ phase, Al is a faster diffuser, while the converse is true in the γ' phase.

Chapter 7

Summary

In this thesis we used a combination of first principles and statistical mechanics to explore the thermodynamic and kinetic behavior of Ni-Al based alloys. Using cluster expansion methods, we link the atomic interactions of first principles calculations to macroscopic quantities at higher temperatures. We focused primarily on the calculation of phase diagrams and diffusion coefficients.

In chapter 3, we explore the phase stability of the Ni-Al binary, both at 0K and finite temperature. We confirm the stability of well characterized intermetallic phases γ' and β, and also find a new family of groundstate orderings, derived from smaller units of the γ' and β orderings. A comparison between our calculated phase diagram with experiments shows good agreement, with some discrepancies for the stability of β at higher temperature. We attribute the discrepancies to anharmonic vibrational effects that stabilize the Ni rich β phase at higher temperatures.

In chapter 4, we develop a method to parameterize multicomponent cluster expansions recursively, using cluster expansions from lower subsystems as informative Bayesian priors. We use this method to extend the binary cluster expansion used for the Ni-Al binary into a Ni-Al-Cr ternary cluster expansion. Using this cluster expansion, we predict significant solubility for both the γ and γ' phases at high temperature. We also look at the sublattice preference of Cr in the $L1_2$ ordering of γ', and found that it overwhelmingly prefers the Al sublattice. By systematically enumerating orderings on FCC and BCC, we found an additional set of unreported long range orderings in the Ni-Cr and Cr-Al binaries.

Chapter 5 introduces the concept of the Kinetically Resolved Activation, a useful metric for atomic mobility from which activation barriers can be determined. We outline a systematic method to enumerate local environments around hops, and use it to to investigate nearest neighbor vacancy exchanges in Ni-Al. Our results show that while Ni hops are largely independent of their local environment, the KRA values for Al hops vary significantly depending on the amount of other Al atoms in the local environment. We then outline how to use cluster expansion methods to predict KRA values as a function of local ordering.

In chapter 6 we combine methods described in the rest of the sections to comprehensively model diffusion in Ni-Al. Cluster expansions fully dictate the energetics of hop events, and we use Kubo-Green relations to calculate diffusion coefficients. We find that Al diffuses faster than Ni in the γ phase, while Ni is the faster diffuser in γ'. The behavior can be understood by examining the possible hops within the $L1_2$ ordering that minimize the number of defects created.

Bibliography

[1] J. G. Goiri and A. Van der Ven, *Phase and structural stability in Ni-Al systems from first principles*, *Physical Review B* **94** (Sept., 2016).

[2] J. G. Goiri and A. Van der Ven, *Recursive alloy Hamiltonian construction and its application to the Ni-Al-Cr system*, *Acta Materialia* **159** (Oct., 2018) 257–265.

[3] L. Feng, D. Lv, R. K. Rhein, J. G. Goiri, M. S. Titus, A. Van der Ven, T. M. Pollock, and Y. Wang, *Shearing of γ' particles in Co-base and Co-Ni-base superalloys*, *Acta Materialia* **161** (Dec., 2018) 99–109.

[4] W. Betteridge and S. W. K. Shaw, *Development of superalloys*, *Materials Science and Technology* **3** (Sept., 1987) 682–694.

[5] "Superalloys II: High-Temperature Materials for Aerospace and Industrial Power."

[6] S. C. Deevi and V. K. Sikka, *Nickel and iron aluminides: an overview on properties, processing, and applications*, *Intermetallics* **4** (1996), no. 5 357–375.

[7] T. M. Pollock and S. Tin, *Nickel-based superalloys for advanced turbine engines: chemistry, microstructure and properties*, *Journal of propulsion and power* **22** (2006), no. 2 361–374.

[8] F. L. Curzon, *Efficiency of a Carnot engine at maximum power output*, *American Journal of Physics* **43** (1975), no. 1 22.

[9] N. P. Padture, M. Gell, and E. H. Jordan, *Thermal barrier coatings for gas-turbine engine applications*, *Science* **296** (2002), no. 5566 280–284.

[10] Z. Yu, D. Hass, and H. Wadley, *NiAl bond coats made by a directed vapor deposition approach*, *Materials Science and Engineering: A* **394** (Mar., 2005) 43–52.

[11] C. S. Giggins and F. Pettit, *Oxidation of Ni-Cr-Al Alloys Between 1000° and 1200° C*, *Journal of the Electrochemical Society* **118** (1971), no. 11 1782–1790.

[12] A. G. Evans, D. R. Mumm, J. W. Hutchinson, G. H. Meier, and F. S. Pettit, *Mechanisms controlling the durability of thermal barrier coatings*, *Progress in materials science* **46** (2001), no. 5 505–553.

[13] W. Brandl, D. Toma, and H. Grabke, *The characteristics of alumina scales formed on HVOF-sprayed MCrAlY coatings*, *Surface and Coatings Technology* **108-109** (Oct., 1998) 10–15.

[14] W. Huang and Y. A. Chang, *A thermodynamic Analysis of the Ni-Al System*, *Intermetallics* **6** 487–498.

[15] Q. Xu and A. Van der Ven, *First-principles investigation of migration barriers and point defect complexes in B2–NiAl*, *Intermetallics* **17** (May, 2009) 319–329.

[16] T. B. Gibbons and B. E. Hopkins, *Creep behaviour and microstructure of Ni-Cr base alloys*, *Metal Science* **18** (1984), no. 5 273–280.

[17] T. M. Pollock and A. S. Argon, *Creep resistance of CMSX-3 nickel base superalloy single crystals*, *Acta Metallurgica et Materialia* **40** (Jan., 1992) 1–30.

[18] R. RICKS, A. PORTER, and R. ECOB, *THE GROWTH OF GAMMA'-PRECIPITATES IN NICKEL-BASE SUPER-ALLOYS*, *ACTA METALLURGICA* **31** (1983), no. 1 43–53.

[19] R. C. Reed, M. P. Jackson, and Y. S. Na, *Characterization and Modeling of the Precipitation of the Sigma Phase in UDIMET 720 and UDIMET 720li*, *Metallurgical and Materials Transactions A* **30** (1999), no. 3 521–533.

[20] H.-E. Zschau, W. Zhao, S. Neve, B. Gleeson, and M. Schütze, *Promotion of the Al2o3-Scale Formation on Ni–Cr–Al Alloys via the Fluorine Effect*, *Oxidation of Metals* **83** (Apr., 2015) 335–349.

[21] J. Müller and D. Neuschütz, *Efficiency of α-alumina as diffusion barrier between bond coat and bulk material of gas turbine blades*, *Vacuum* **71** (May, 2003) 247–251.

[22] Z. Zhang, B. Gleeson, K. Jung, L. Li, and J. C. Yang, *A diffusion analysis of transient subsurface γ'-Ni3al formation during β-NiAl oxidation*, *Acta Materialia* **60** (Aug., 2012) 5273–5283.

[23] A. Van der Ven, M. K. Aydinol, and G. Ceder, *First-Principles Evidence for Stage Ordering in Li x CoO2*, *Journal of The Electrochemical Society* **145** (1998), no. 6 2149–2155.

[24] A. Van der Ven, H.-C. Yu, G. Ceder, and K. Thornton, *Vacancy mediated substitutional diffusion in binary crystalline solids*, *Progress in Materials Science* **55** (Feb., 2010) 61–105.

[25] B. Tryon, F. Cao, K. S. Murphy, C. G. Levi, and T. M. Pollock, *Ruthenium-containing bond coats for thermal barrier coating systems*, *JoM* **58** (2006), no. 1 53–59.

[26] P. K. Wright and A. G. Evans, *Mechanisms governing the performance of thermal barrier coatings*, *Current Opinion in Solid State and Materials Science* **4** (1999), no. 3 255–265.

[27] A. J. Bradley and A. Taylor, *X-Ray Analysis of the Ni-Al System*, *Proceedings of the Royal Society of London. Series A, Mathematical and Physical Sciences* **159** (Mar., 1937) 56–72.

[28] S. Takizawa, S. Miura, and T. Mohri, *Structural stability of NiAl with the L10 structure and local lattice distortion in the Ni3al alloy around excess Al atoms*, *Intermetallics* **13** (Nov., 2005) 1137–1140.

[29] J. L. Smialek and R. F. Hehemann, *Transformation temperatures of martensite in \backslash-phase nickel aluminide*, *Metallurgical Transactions* **4** (1973), no. 6 1571–1575.

[30] Schryvers, D., Toth, L., Ma, Y., and Tanner, L., *Nucleation and Growth of the Ni5al3 Phase in Ni-Al Austenite and Martensite*, *J. Phys. IV France* **05** (1995), no. C2 C2–299–C2–304.

[31] P. S. Khadkikar, I. E. Locci, K. Vedula, and G. M. Michal, *Transformation to ni5al3 in a 63.0 at. pct ni-al alloy*, *Metallurgical transactions A* **24** (1993), no. 1 83–94.

[32] P. Boullay, D. Schryvers, and J. Ball, *Nano-structures at martensite macrotwin interfaces in Ni65al35*, *Acta Materialia* **51** (Mar., 2003) 1421–1436.

[33] G. P. Purja Pun and Y. Mishin, *Molecular dynamics simulation of the martensitic phase transformation in NiAl alloys*, *Journal of Physics: Condensed Matter* **22** (Oct., 2010) 395403.

[34] J. P. Perdew, K. Burke, and M. Ernzerhof, *Generalized gradient approximation made simple*, *Physical review letters* **77** (1996), no. 18 3865.

[35] G. Kresse and J. Furthmüller, *Efficiency of ab-initio total energy calculations for metals and semiconductors using a plane-wave basis set*, *Computational Materials Science* **6** (1996) 15–50.

[36] G. Kresse and J. Furthmüller, *Efficient iterative schemes for ab initio total-energy calculations using a plane-wave basis set*, *Physical Review B* **54** (1996), no. 16 11169.

[37] G. Kresse and D. Joubert, *From ultrasoft pseudopotentials to the projector augmented-wave method*, *Physical Review B* **59** (1999), no. 3 1758.

[38] C. Developers, *Casmcode: v0.1.0*, 2015.

[39] J. C. Thomas and A. Van der Ven, *Finite-temperature properties of strongly anharmonic and mechanically unstable crystal phases from first principles*, *Physical Review B* **88** (Dec., 2013).

[40] A. Van der Ven, J. Thomas, Q. Xu, and J. Bhattacharya, *Linking the electronic structure of solids to their thermodynamic and kinetic properties*, *Mathematics and Computers in Simulation* **80** (Mar., 2010) 1393–1410.

[41] B. Puchala and A. Van der Ven, *Thermodynamics of the Zr-O system from first-principles calculations*, *Physical Review B* **88** (Sept., 2013).

[42] C. Wolverton and A. Zunger, *Magnetic destabilization of Ni 7 Al*, *Physical Review B* **59** (1999), no. 19 12165.

[43] H. Hencky, *Welche Umstände bedingen die Verfestigung bei der bildsamen Verformung von festen isotropen Körpern?*, *Zeitschrift für Physik* **55** (1929), no. 3-4 145–155.

[44] G. R. Barsch and J. A. Krumhansl, *Twin boundaries in ferroelastic media without interface dislocations*, *Physical Review Letters* **53** (1984), no. 11 1069.

[45] W. Burgers, *On the process of transition of the cubic-body-centered modification into the hexagonal-close-packed modification of zirconium*, *Physica* **1** (May, 1934) 561–586.

[46] J. Thomas, A. R. Natarajan, J. Bechtel, and A. Van der Ven, *In preparation*, .

[47] J. M. Sanchez, F. Ducastelle, and D. Gratias, *Generalized cluster description of multicomponent systems*, *Physica A: Statistical Mechanics and its Applications* **128** (Nov., 1984) 334–350.

[48] J. M. Sanchez, *Cluster expansion and the configurational theory of alloys*, *Physical Review B* **81** (June, 2010).

[49] D. De Fontaine, *Cluster approach to order-disorder transformations in alloys*, in *Solid state physics*, vol. 47, pp. 33–176. Elsevier, 1994.

[50] J. W. D. Connolly and A. R. Williams, *Density-functional theory applied to phase transformations in transition-metal alloys*, *Physical Review B* **27** (1983), no. 8 5169.

[51] G. L. W. Hart, V. Blum, M. J. Walorski, and A. Zunger, *Evolutionary approach for determining first-principles hamiltonians*, *Nature Materials* **4** (May, 2005) 391–394.

[52] P. A. Korzhavyi, A. V. Ruban, A. Y. Lozovoi, Y. K. Vekilov, I. A. Abrikosov, and B. Johansson, *Constitutional and thermal point defects in B 2 NiAl*, *Physical Review B* **61** (2000), no. 9 6003.

[53] Y. Mishin, M. J. Mehl, and D. A. Papaconstantopoulos, *Embedded-atom potential for B 2 - NiAl*, *Physical Review B* **65** (June, 2002).

[54] B. Meyer and M. Fähnle, *Atomic defects in the ordered compound B 2-NiAl: A combination of ab initio electron theory and statistical mechanics*, *Physical Review B* **59** (1999), no. 9 6072.

[55] M. Ellner, S. Kek, and B. Predel, *Ni3al4 - A Phase with Ordered Vacacies Isotypic to Ni3ga4*, *Journal of Less-Common Metals* **154** (1989) 207–215.

[56] D. de Fontaine, G. Ceder, and M. Asta, *Low-temperature long-range oxygen order in YBa2cu3oz*, *Nature* **343** (Feb., 1990) 544–546.

[57] A. R. Natarajan, E. L. Solomon, B. Puchala, E. A. Marquis, and A. Van der Ven, *On the early stages of precipitation in dilute Mg–Nd alloys*, *Acta Materialia* **108** (Apr., 2016) 367–379.

[58] Y. Wang, S. Curtarolo, C. Jiang, R. Arroyave, T. Wang, G. Ceder, L.-Q. Chen, and Z.-K. Liu, *Ab initio lattice stability in comparison with CALPHAD lattice stability*, *Calphad* **28** (Mar., 2004) 79–90.

[59] P. D. Tepesch, G. D. Garbulsky, and G. Ceder, *Model for configurational thermodynamics in ionic systems*, *Physical review letters* **74** (1995), no. 12 2272.

[60] B. C. Han, A. Van der Ven, G. Ceder, and B.-J. Hwang, *Surface segregation and ordering of alloy surfaces in the presence of adsorbates*, *Physical Review B* **72** (Nov., 2005).

[61] Y. Mishin and D. Farkas, *Atomistic simulation of point defects and diffusion in B2 NiAl: Part I. Point defect energetics*, *Philosophical Magazine A* **75** (Jan., 1997) 169–185.

[62] A. Van de Walle and M. Asta, *Self-driven lattice-model Monte Carlo simulations of alloy thermodynamic properties and phase diagrams*, *Modelling and Simulation in Materials Science and Engineering* **10** (2002), no. 5 521.

[63] A. Van der Ven and G. Ceder, *First Principles Calculation of the Interdiffusion Coefficient in Binary Alloys*, *Physical Review Letters* **94** (Feb., 2005).

[64] A. A. Belak and A. Van der Ven, *Effect of disorder on the dilute equilibrium vacancy concentrations of multicomponent crystalline solids*, *Physical Review B* **91** (June, 2015).

[65] Y. Mishin, *Atomistic modeling of the γ and γ'-phases of the Ni–Al system*, *Acta Materialia* **52** (Apr., 2004) 1451–1467.

[66] C. Woodward, A. van de Walle, M. Asta, and D. Trinkle, *First-principles study of interfacial boundaries in Ni–Ni3al*, *Acta Materialia* **75** (Aug., 2014) 60–70.

[67] I. Ansara, B. Sundman, and P. Willemini, *Ni-Al assessment (CALPHAD)*, *Acta Metallurgica* **36** (Oct., 1986) 997–982.

[68] J. C. Thomas and A. Van der Ven, *Elastic properties and stress-temperature phase diagrams of high-temperature phases with low-temperature lattice instabilities*, *Physical Review B* **90** (Dec., 2014).

[69] R. Quijano, R. de Coss, and D. J. Singh, *Electronic structure and energetics of the tetragonal distortion for TiH 2 , ZrH 2 , and HfH 2 : A first-principles study*, *Physical Review B* **80** (Nov., 2009).

[70] J. Bhattacharya and A. Van der Ven, *Mechanical instabilities and structural phase transitions: The cubic to tetragonal transformation*, *Acta Materialia* **56** (Sept., 2008) 4226–4232.

[71] J. C. Wojdeł, P. Hermet, M. P. Ljungberg, P. Ghosez, and J. Íñiguez, *First-principles model potentials for lattice-dynamical studies: general methodology and example of application to ferroic perovskite oxides*, *Journal of Physics: Condensed Matter* **25** (July, 2013) 305401.

[72] W. Zhong, D. Vanderbilt, and K. M. Rabe, *Phase Transitions in BaTi O 3 from First Principles*, *Physical Review Letters* **73** (1994), no. 13 1861.

[73] U. V. Waghmare and K. M. Rabe, *Ab initio statistical mechanics of the ferroelectric phase transition in PbTiO 3*, *Physical Review B* **55** (1997), no. 10 6161.

[74] K. M. Rabe and U. V. Waghmare, *Localized basis for effective lattice hamiltonians: Lattice Wannier functions*, *Physical Review B* **52** (1995), no. 18 13236.

[75] R. Arroyave, D. Shin, and Z.-K. Liu, *Ab initio thermodynamic properties of stoichiometric phases in the Ni–Al system*, *Acta Materialia* **53** (Apr., 2005) 1809–1819.

[76] A. Van de Walle, G. Ceder, and U. V. Waghmare, *First-principles computation of the vibrational entropy of ordered and disordered Ni 3 Al*, *Physical review letters* **80** (1998), no. 22 4911.

[77] MAAS, J. H., TOTH, L., HAMERS, A. A.H., and BEYER, J., *TRANSFORMATION BEHAVIOUR OF THE Al - 65% Ni ALLOY*, *J. Phys. IV France* **01** (1991), no. C4 C4–373–C4–378.

[78] Schryvers, D., *Martensitic and Related Transformations in Ni-Al Alloys*, *J. Phys. IV France* **05** (1995), no. C2 C2–225–C2–234.

[79] K. Enami and S. Nenno, *Memory effect in Ni-36.8 at. pct Al martensite*, *Metallurgical and materials Transactions B* **2** (1971), no. 5 1487–1490.

[80] S. Chakravorty and C. M. Wayman, *The thermoelastic martensitic transformation inβ' Ni-Al alloys: I. Crystallography and morphology*, *Metallurgical transactions A* **7** (1976), no. 4 555–568.

[81] K. Enami, S. Nenno, and K. Shimizu, *Crystal structure and internal twins of the Ni-36.8 at% Al martensite*, *Transactions of the Japan Institute of Metals* **14** (1973), no. 2 161–165.

[82] K. Momma and F. Izumi, *VESTA 3 for three-dimensional visualization of crystal, volumetric and morphology data*, *Journal of Applied Crystallography* **44** (Dec., 2011) 1272–1276.

[83] J. D. Hunter, *Matplotlib: A 2d graphics environment*, *Computing In Science & Engineering* **9** (2007), no. 3 90–95.

[84] M.-H. Tsai and J.-W. Yeh, *High-Entropy Alloys: A Critical Review*, *Materials Research Letters* **2** (July, 2014) 107–123.

[85] O. Senkov, G. Wilks, J. Scott, and D. Miracle, *Mechanical properties of Nb25mo25ta25w25 and V20nb20mo20ta20w20 refractory high entropy alloys*, *Intermetallics* **19** (May, 2011) 698–706.

[86] D. Miracle and O. Senkov, *A critical review of high entropy alloys and related concepts*, *Acta Materialia* **122** (Jan., 2017) 448–511.

[87] D. B. Miracle, *High-Entropy Alloys: A Current Evaluation of Founding Ideas and Core Effects and Exploring “Nonlinear Alloys”*, *JOM* **69** (Nov., 2017) 2130–2136.

[88] Z. Li and D. Raabe, *Strong and Ductile Non-equiatomic High-Entropy Alloys: Design, Processing, Microstructure, and Mechanical Properties*, *JOM* **69** (Nov., 2017) 2099–2106.

[89] B. Cantor, *Multicomponent and High Entropy Alloys*, *Entropy* **16** (Aug., 2014) 4749–4768.

[90] L. J. Nelson, V. Ozoliņš, C. S. Reese, F. Zhou, and G. L. W. Hart, *Cluster expansion made easy with Bayesian compressive sensing*, *Physical Review B* **88** (Oct., 2013).

[91] L. J. Nelson, G. L. W. Hart, F. Zhou, and V. Ozoliņš, *Compressive sensing as a paradigm for building physics models*, *Physical Review B* **87** (Jan., 2013).

[92] T. Mueller and G. Ceder, *Bayesian approach to cluster expansions*, *Physical Review B* **80** (July, 2009).

[93] W. Huang, A. Urban, Z. Rong, Z. Ding, C. Luo, and G. Ceder, *Construction of ground-state preserving sparse lattice models for predictive materials simulations*, *npj Computational Materials* **3** (Dec., 2017).

[94] X. Ma and N. Zabaras, *An efficient Bayesian inference approach to inverse problems based on an adaptive sparse grid collocation method*, *Inverse Problems* **25** (Mar., 2009) 035013.

[95] A. van de Walle and G. Ceder, *Automating first-principles phase diagram calculations*, *Journal of Phase Equilibria* **23** (2002), no. 4 348–359.

[96] F. H. Stott, *The protective action of oxide scales in gaseous environments at high temperature*, *Rep. Prog. Phys.* **50** (1987), no. 7 861.

[97] P. Saltykov, O. Fabrichnaya, J. Golczewski, and F. Aldinger, *Thermodynamic modeling of oxidation of Al–Cr–Ni alloys*, *Journal of Alloys and Compounds* **381** (Nov., 2004) 99–113.

[98] Y. Wang, Z.-K. Liu, and L.-Q. Chen, *Thermodynamic properties of Al, Ni, NiAl, and Ni3al from first-principles calculations*, *Acta Materialia* **52** (May, 2004) 2665–2671.

[99] L. Barnard, G. Young, B. Swoboda, S. Choudhury, A. Van der Ven, D. Morgan, and J. Tucker, *Atomistic modeling of the order–disorder phase transformation in the Ni2cr model alloy*, *Acta Materialia* **81** (Dec., 2014) 258–271.

[100] J. M. Sanchez, *Cluster expansions and the configurational energy of alloys*, *Physical review B* **48** (1993), no. 18 14013.

[101] G. Inden, *Atomic Ordering*, in *Phase Transformations in Materials*, pp. 519–581. Wiley-VCH Verlag GmbH & Co. KGaA, 2005.

[102] X. Zhang and M. H. F. Sluiter, *Cluster Expansions for Thermodynamics and Kinetics of Multicomponent Alloys*, *Journal of Phase Equilibria and Diffusion* **37** (Feb., 2016) 44–52.

[103] K. P. Murphy, *Machine learning: a probabilistic perspective.* Adaptive computation and machine learning series. MIT Press, Cambridge, MA, 2012.

[104] F. Pedregosa, G. Varoquaux, A. Gramfort, V. Michel, B. Thirion, O. Grisel, M. Blondel, P. Prettenhofer, R. Weiss, V. Dubourg, J. Vanderplas, A. Passos, D. Cournapeau, M. Brucher, M. Perrot, and E. Duchesnay, *Scikit-learn: Machine Learning in Python*, *Journal of Machine Learning Research* **12** (2011) 2825–2830.

[105] D. G. T. Denison, *Bayesian Methods for Nonlinear Classification and Regression.* John Wiley & Sons, May, 2002. Google-Books-ID: SIlDWySNuXgC.

[106] C. Developers, *CASMcode: v0.1.0*, tech. rep., Zenodo, Sept., 2015.

[107] A. Belsky, M. Hellenbrandt, V. L. Karen, and P. Luksch, *New developments in the Inorganic Crystal Structure Database (ICSD): accessibility in support of materials research and design*, *Acta Crystallographica Section B: Structural Science* **58** (2002), no. 3 364–369.

[108] A. Marucco and B. Nath, *Effects of ordering on the properties of Ni-Cr alloys*, *Journal of materials science* **23** (1988), no. 6 2107–2114.

[109] M. Audier, M. Durand-Charre, E. Laclau, and H. Klein, *Phase equilibria in the Al? Cr system*, *Journal of alloys and compounds* **220** (1995), no. 1-2 225–230.

[110] Y. Wang and G. Cacciamani, *Thermodynamic modeling of the Al-Cr-Ni system over the entire composition and temperature range*, *Journal of Alloys and Compounds* **688** (Dec., 2016) 422–435.

[111] B. Cao and K. Kuo, *Crystal structure of the monoclinic η-Al11cr2*, *Journal of Alloys and Compounds* **458** (June, 2008) 238–247.

[112] A. R. Natarajan and A. Van der Ven, *First-principles investigation of phase stability in the Mg-Sc binary alloy*, *Physical Review B* **95** (June, 2017).

[113] A. R. Natarajan, J. C. Thomas, B. Puchala, and A. Van der Ven, *Symmetry-adapted order parameters and free energies for solids undergoing order-disorder phase transitions*, *Phys. Rev. B* **96** (Oct., 2017) 134204.

[114] W. Huang and Y. A. Chang, *Thermodynamic properties of the Ni–Al–Cr system*, *Intermetallics* **7** (1999), no. 8 863–874.

[115] V. Blum, G. L. W. Hart, M. J. Walorski, and A. Zunger, *Using genetic algorithms to map first-principles results to model Hamiltonians: Application to the generalized Ising model for alloys*, *Physical Review B* **72** (Oct., 2005).

[116] T. Mueller, *Ab initio determination of structure-property relationships in alloy nanoparticles*, *Phys. Rev. B* **86** (Oct., 2012) 144201.

[117] J. Kristensen and N. J. Zabaras, *Bayesian uncertainty quantification in the evaluation of alloy properties with the cluster expansion method*, *Computer Physics Communications* **185** (Nov., 2014) 2885–2892.

[118] M. Asta, C. Wolverton, D. de Fontaine, and H. Dreyssé, *Effective cluster interactions from cluster-variation formalism. I*, *Physical Review B* **44** (Sept., 1991) 4907–4913.

[119] E. Fawcett, *Spin-density-wave antiferromagnetism in chromium*, *Rev. Mod. Phys.* **60** (Jan., 1988) 209–283.

[120] J. S. Wróbel, D. Nguyen-Manh, M. Y. Lavrentiev, M. Muzyk, and S. L. Dudarev, *Phase stability of ternary fcc and bcc Fe-Cr-Ni alloys*, *Physical Review B* **91** (Jan., 2015).

[121] M. Y. Lavrentiev, J. S. Wróbel, D. Nguyen-Manh, S. L. Dudarev, and M. G. Ganchenkova, *Magnetic Cluster Expansion model for random and ordered magnetic face-centered cubic Fe-Ni-Cr alloys*, *Journal of Applied Physics* **120** (July, 2016) 043902. arXiv: 1503.02481.

[122] F. Teng, L.-J. Yu, O. Ciuca, E. Marquis, G. Burke, and J. D. Tucker, *The Role of Stoichiometry on Ordering Phase Transformations in Ni–Cr Alloys for Nuclear Applications*, in *Proceedings of the 18th International Conference on Environmental Degradation of Materials in Nuclear Power Systems – Water Reactors* (J. H. Jackson, D. Paraventi, and M. Wright, eds.), pp. 251–259. Springer International Publishing, Cham, 2018.

[123] B. Gwalani, T. Alam, C. Miller, T. Rojhirunsakool, Y. Kim, S. Kim, M. Kaufman, Y. Ren, and R. Banerjee, *Experimental investigation of the ordering pathway in a Ni-33 at.%Cr alloy*, *Acta Materialia* **115** (Aug., 2016) 372–384.

[124] F. Teng and J. D. Tucker, *Role of Stoichiometry on Ordering in Ni-Cr Alloys*, *MRS Online Proceedings Library Archive* **1809** (2015) 7–12.

[125] A. Marucco, *Atomic ordering and α'-Cr phase precipitation in long-term aged Ni3cr and Ni2cr alloys*, *Journal of materials science* **30** (1995), no. 16 4188–4194.

[126] A. R. Natarajan and A. Van der Ven, *A unified description of ordering in HCP Mg-RE alloys*, *Acta Materialia* **124** (Feb., 2017) 620–632.

[127] K. W. Kehr, K. Binder, and S. M. Reulein, *Mobility, interdiffusion, and tracer diffusion in lattice-gas models of two-component alloys*, *Phys. Rev. B* **39** (Mar., 1989) 4891–4910.

[128] J. W. Cahn and F. C. Larché, *An invariant formulation of multicomponent diffusion in crystals*, *Scripta Metallurgica* **17** (July, 1983) 927–932.

[129] R. E. Howard and A. B. Lidiard, *Matter transport in solids*, *Reports on Progress in Physics* **27** (Jan., 1964) 161–240.

[130] L. Onsager, *Reciprocal Relations in Irreversible Processes. I.*, *Phys. Rev.* **37** (Feb., 1931) 405–426.

[131] L. Darken, *Diffusion, Mobility and Their Interrelation Through Free Energy in Binary Metallic Systems*, *Transactions of the American Institute of Mining and Metallurgical Engineers* **175** (1948) 184–201. WOS:A1948XR33900011.